Master of Science Thesis

Design Methodology and Optimization of Kick Stage Main Structures

Akshay Kulkarni

Faculty of Aerospace Engineering · Delft University of Technology

TU Delft Delft University of Technology

Design Methodology and Optimization of Kick Stage Main Structures

Master of Science Thesis

For obtaining the degree of Master of Science in Aerospace Engineering
at Delft University of Technology

Akshay Kulkarni

March 27 2023

Faculty of Aerospace Engineering · Delft University of Technology

The work in this thesis was supported by ArianeGroup GmbH, Bremen and University of Bremen. Their cooperation is gratefully acknowledged.

Delft University of Technology
Faculty of Aerospace Engineering
Department of Aerospace Structures and Materials

GRADUATION COMMITTEE

Dated: March 27 2023

Chair holder:

Dr.-Ing. S.G.P. (Saullo) Castro

Committee members:

Dr.ir. Erwin Mooij

I. (Ines) Uriol Balbin

Co-supervisors:

Dipl.-Phys. Robert Meitzner

Prof. Dr.-Ing. Richard Degenhardt

Abstract

The kick stage is an ongoing project at ArianeGroup GmbH that will boost the versatility of the Ariane 6 launcher. The design methodology development of the kick stage main structure using structural optimization techniques is the scope of this master thesis research project. The master thesis forms a consequential component of the academic requirements for graduation requirements for the Master of Science in the aerospace engineering program at the Delft University of Technology. This research project has been completed in collaboration with ArianeGroup GmbH at the Bremen site and the University of Bremen.

The kick stage is an additional stage on the top of the upper stage of the Ariane 6 launch vehicle. The propellant tanks are a dominant load of the kick stage and they are located along an off-axis with respect to the launcher's central axis. Considering this, it is imperative that the main structure withstands the static, dynamic, and buckling loads acting on the propellant tanks and limits them to acceptable levels. The scope of the research project is the development of a lightweight design methodology for the main structure that constrains the heavy propellant tanks against mechanical loads.

Initially, the project requirements and the research goals have been planned out. This has been followed by a literature study of similar missions and the current advances in the analytical and numerical methods for designing this structure. The problem has been solved using the concepts of structural optimization using OptiStruct solver. Initially, topology optimization principles have been used to generate the design critical regions from the total design space. Afterward, size optimization methods have been implemented to modify the design to meet the design constraints. In addition, an innovative design using composite grid structure methodology has been proposed and analyzed for the primary loading conditions.

The resultant methodology proposed indicates that a combination of topology and size optimization has helped to create stiffer structures while meeting the dynamic requirements. The design performance can be scaled with low efforts to match the input dynamic load. Additionally, the anisogrid composite design for cylinders under compressive loading is a promising lightweight solution for improving the buckling and dynamic performance of the stage core.

Preface

While completing my internship at ArianeGroup GmbH in Bremen, I came across enriching topics in the space industry. After working on dynamic modeling and vibration testing of a thruster assembly, I wanted to work on structural optimization methods for my Master's thesis. After going through a pool of topics at the university with the professors and also discussing a list of topics with my senior colleagues at ArianeGroup, I finally decided to choose this structural development and optimization topic. This topic fits in perfectly with the research area of optimization that I wanted to increase my expertise in, combing structural optimization with dynamics. The research goals of the thesis were closely aligned with the M.Sc. coursework, my learning curve, and my career goals. Even though the start was a bit shaky due to certain administrative uncertainties, I am delighted to research this topic for my master's thesis and finish my master's degree in aerospace engineering on a high note.

I am sincerely grateful to my supervisor Dr.-Ing. S.G.P. (Saullo) Castro for his continuous support and expertise to guide me throughout this thesis project. I would also like to thank my co-supervisor Prof. Dr.-Ing. Richard Degenhardt for providing me with valuable research insights and facilitating my guest student stay at the University of Bremen. I would also like to thank my co-supervisor Dipl.-Phys. Robert Meitzner at ArianeGroup GmbH for his guidance on this subject and his expertise on the dynamics of launchers. In addition, I am also thankful to all my colleagues on the Dynamics and Testing team, especially, Detlev Buelten, Francois Gori, and Vasu Ramonalla for facilitating this thesis position and mentoring me while working in the team. I am humbled to have this amazing technical interaction with everyone, and I look forward to more such future collaborations regarding space structure development.

Last but not the least, I am very grateful to my parents and my sister for being the source of my inspiration, financing this master's program, and motivating me to chase these big dreams. I am also very grateful to my fiancee for always supporting and encouraging me throughout this journey. Without you all, none of this would have been possible.

Delft, University of Technology — Akshay Kulkarni
March 27 2023

Table of Contents

List of Figures

List of Tables

Chapter 1

Introduction

A launch vehicle requires staging to put a payload into orbit. This is due to the science of laws of physics and Earth's gravity that direct the rocket equation and moreover the engineering limit on the fuel chemical compositions and the structural design possibilities. For contemporary rockets, there is usually a 2-stage to orbit or 3-stage to low earth or geostationary transfer orbit available and this staging could be series or parallel [28]. Some missions such as trans lunar injections or moon missions can greatly benefit from an additional stage provided by the launch vehicle. This leads to missions where an additional series stage on top of the upper stage is very useful. Such missions are where the kick stage is applicable.

1.1 Introduction to the kick stage

The Astris kick stage is the project for an additional stage which will be placed before spacecraft deployment and after the upper stage of the launch vehicle Ariane 6. There are multiple missions for which such an additional kick stage could be useful. This includes deep-space missions, constellation missions, or transfer orbit missions. The two configurations that the kick stage can be particularly useful as is shown in Figure 1.1 for a satellite configuration and in Figure 1.2 for a constellation configuration. The spacecraft to be deployed is bolted to the top interface of the kick stage. The entire rocket with its upper stage and core stage will propel the kick stage and payload together to earth orbit. After the burning of the upper stage, the kick stage propulsion switches on and provides this additional thrust for the subsequent orbit transfers or deep space exploration goals of the spacecraft.

Thus, the propulsion system fuel requirements for the standalone payload will be lowered due to this additional kick stage, as it will provide the necessary thrust for the trajectory to the design orbit. In addition, for moon-based or inter-planetary missions, a series of kick stages could be stacked, one on top of the other in sets of four or six. Thus, the versatility of the new launcher Ariane 6 would be further improved due to the addition of the kick stage [4] [15] [21].

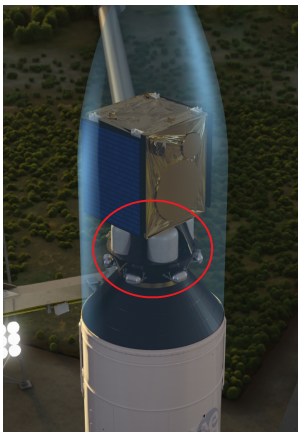

Figure 1.1: The kick stage (encircled in red) in a satellite launch configuration.[4]

Figure 1.2: The kick stage (encircled in red) in a constellation launch configuration.[4]

1.2 Motivation for lightweight design for the kick stage

The push for lightweight designed structures for the aerospace industry has always been in high demand, and the push is even larger for the space launch industry. The launch cost per kg and the payload ratio are two aspects that are briefly discussed here to motivate this demand for lightweight structures.

Figure 1.3 shows a graph that provides the data for the cost to launch one kg of payload to space. Adjusting for inflation, it can be noted that the graph has a downward trend. We can see that the approximate launch cost has reduced to one-tenth of its value from forty years ago. However, despite the downward trend, the present-day costs are approximately 2000 \$/kg. The launch cost will be lowered proportionally to the payload mass. The propellant mass is a major constituent of the total wet mass of the payload. Additionally, within the dry mass of the payload, the mass contribution of mechanical structures to the mass budget is the major fraction compared to other equipment such as avionics or thermal control. Thus, structure optimization of the spacecraft mechanical structures is sought out for the payload under development [21].

The payload fraction (a comparable term to the mass ratio) is useful to understand the concept of the kick stage and lightweight design. It is used to characterize the efficiency of an aerospace design and is defined as a simple ratio of the mass of the payload and the total takeoff mass. This is important because the fuel forms a major fraction of the total takeoff mass. For example, for commercial aircraft, the number is of the order of $45 - 55\%$ for a modern jet airliner. It is in one-digit percentages for a space launcher, as the payload fraction is about 2.5% for the Ariane 5 launcher. Furthermore, the payload fraction is even lower for spacecraft payloads, approximately 1%. This is because a large propulsion system with large fuel tanks is usually required for a given spacecraft to reach the designated orbit. The more useful scientific or communication payloads on the spacecraft then tend to have a smaller fraction of the total takeoff mass of the spacecraft. The aim of an additional stage system such as a kick stage is to reduce the mass propulsion system requirement of spacecraft accordingly allowing for a higher payload fraction, and resulting in more payload capacity on

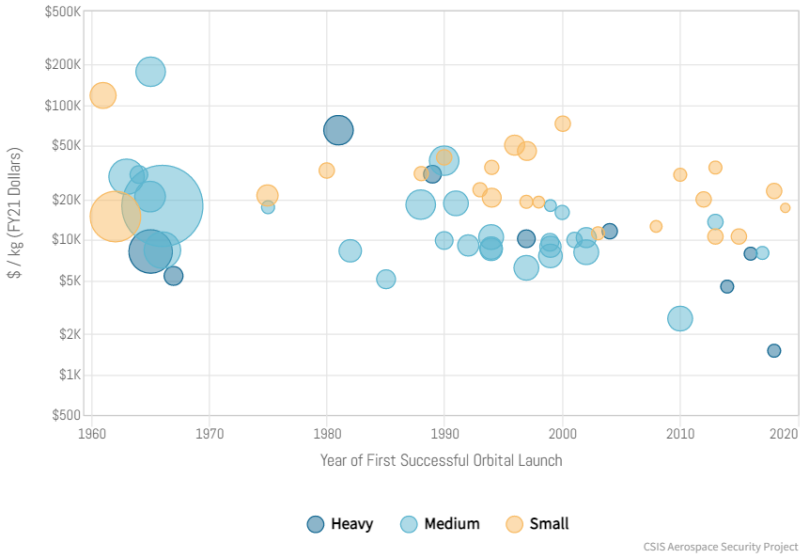

Figure 1.3: Graph denoting the launch cost per kg to LEO for multiple launchers across the world.[31]

board the spacecraft [21].

Considering these factors and the operation of the kick stage, additional mass savings on the kick stage structural dry mass are highly desirable and they will increase the payload carrying capacity of the launcher with the kick stage. The mission payload delivery capabilities would be increased due to the kick stage main structures optimization exercise. This aligns with the ArianeGroup goals of customer satisfaction by making the Ariane 6 with kick stage a more competitive launcher in the increasingly competitive global launch market [21].

1.3 Scope and format of the document

This thesis document starts off with the project description of the kick stage and is discussed in chapter 2. This is followed by the summary of the literature study discussed in chapter 3, while the detailed Literature study can be found in [21]. This is followed by the solution methodology described in chapter 4. The work carried out is divided into three main segments. The topology optimization studies are discussed in chapter 5. The size optimization studies are discussed in chapter 6 and chapter 7. The composite design proposal and preliminary analysis is discussed in chapter 8. Finally, the work is concluded in chapter 9.

Chapter 2

Project Description

The structure description and the architecture of the kick stage are discussed in this chapter. This also leads to the development of the design problem and the subsequent loading conditions for the off-axis propellant tanks.

2.1 Kick stage description

Figure 2.1 shows the detailed view of the kick stage. The propellant tanks are encircled in orange. The helium tanks are encircled in green, holding struts of helium tanks are encircled in red [4]. There are four propellant tanks positioned in a circular pattern around the central axis. The bi-propellant engine fuel is a combination of mono-methyl hydrazine (MMH) serving as the propellant and mixed oxides of nitrogen (MON) serving as the oxidizer. Each propellant fuel is filled into two diagonally opposite pairs of the total of four tanks present in this configuration. The smaller liquid helium tanks are used for pressurizing the propellants during combustion in space. The structural holding struts are present for securing the helium tanks to the main central tube [5] [21].

The kick stage structure consists of a centrally cylindrical tube that interfaces to the top of the upper stage and to the bottom of the satellite. The interfaces are secured by pyrotechnic bolts with clamp separation bands. The lower interface clamp band activates after the upper stage is exhausted. Afterward, the kick stage propels the payload to its mission orbit. Then, the second clamp band activates and detaches the kick stage from the payload. The central structure houses the avionic systems, side thrusters, thermal control equipment, liquid helium tanks, and propellant fuel tanks. The current design proposal consists of using honeycomb panels (CFRP face sheet with aluminium core) or machined aluminum panels for the primary structures of the kick stage. The current kick stage design with an aluminium main structure is approximated to have a dry mass budget of 800kg. The total propellant mass with four propellant tanks results in an approximated wet mass of approximately 4.5t (1t=1tonne=1000kg) [5] [21].

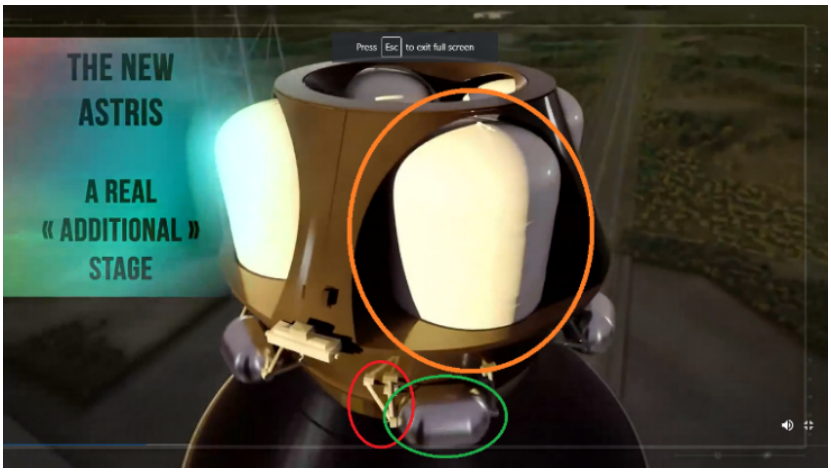

Figure 2.1: The detailed view of the kick stage[4].

2.2 Structure architecture

A CAD model sketch to scale of the structure is shown in Figure 2.2. The design scope is within the sizing bounds of three main components of the architecture. These are the launch vehicle fairing, the central tube, and the propellant tanks. The outer size constraint on the kick stage is decided by the launch vehicle Ariane 6 usable fairing diameter of 4600mm [6]. The central tube interface to the upper stage has a diameter of 1666mm as this diameter will be used for the clamp band selection. The propellant tank dimensions are a diameter of 1154mm and a total height of 1192mm for each tank. The propellant tanks have a nominal offset of 1510mm from the launcher's central axis. This offset of four propellant tanks leads to design requirements for static and dynamic loading on the structure. This is different in comparison to the conventional satellite bus systems, where the propellant tanks are in-line concentric with the central launch axis [21].

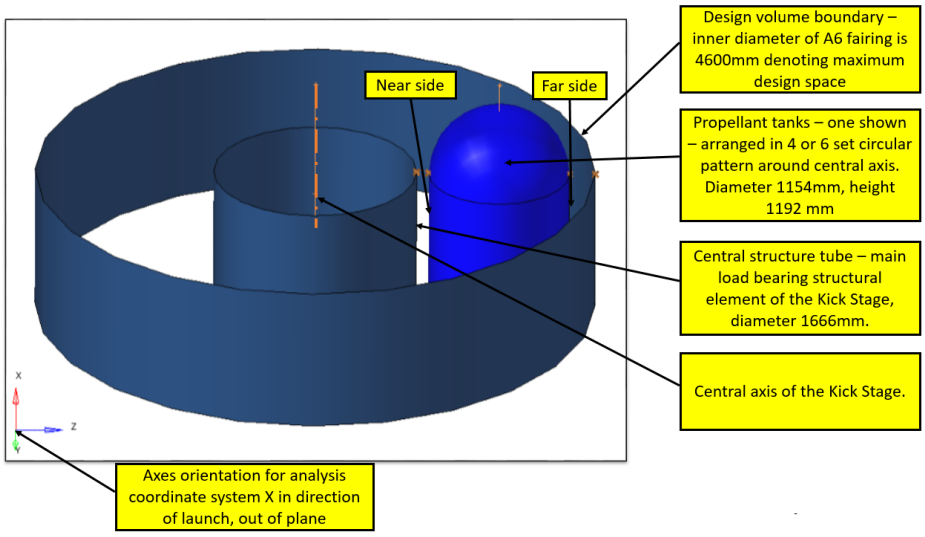

Figure 2.2: Approximate CAD sketch of Kick Stage indicating the size of structures.

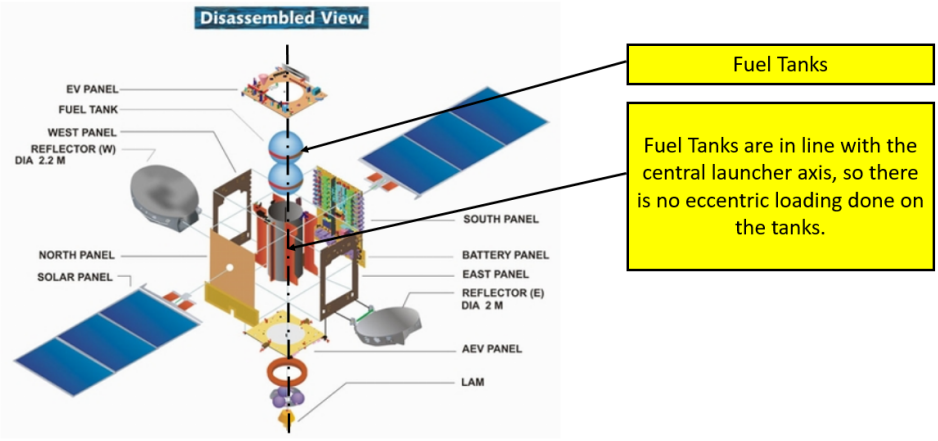

Figure 2.3: CAD model sketch for a conventional satellite – I3K satellite bus.[18]

A conventional satellite bus I3K satellite configuration is shown in Figure 2.3. The propellant tanks are along the central launch axis and are positioned on top of one another. The two propellant tanks are encased within the satellite shear panels structure. The bolting flanges of the propellant tanks have a uniform distribution of static and dynamic stresses. The symmetric boundary conditions on the structure make it comparatively easier to predict dynamic behavior. This is because larger mass contributing out of axis modes will be symmetrically amplified along the edges. This also results in the center of gravity (cog) of the satellite being elevated to a greater height. The amplification on in-plane modes would be significantly increased at corresponding resonant frequencies [21].

A disadvantage of such a configuration for the kick stage is that it would reduce the available height for the payload, as there is a maximum height until which the fairing height on the launcher can be increased. The propellant tanks are certification occurs in this type of in-line loaded configuration, and the input dynamic excitation loads are provided along the propellant tank's central axis. Creating a new qualification test setup for an off-axis loaded condition would be expensive as the whole process qualification would need to be repeated. Considering this, the design development must take into consideration the amplification resulting from off-axis loading [21].

Chapter 3

Literature Study Summary

The detailed literature review of the project is covered in the separate **Literature Study** document [21]. The summary of the literature study is discussed in this chapter in the following sections.

3.1 Design studies for similar missions

A review of some of the previous and upcoming spacecraft designs is discussed in this section. The understanding from this will be used to develop an innovative methodology for the proposed kick stage design and provide additional insights to solve the off-axis propellant tank design problem.

3.1.1 ISRO study for design of an advanced spacecraft

A study for a 6t satellite configuration by Khaleelullah et al. [20] suggests the modifications required for the main structure design to meet the stiffness requirements for the spacecraft [20]. Figure 3.1 shows the configuration of the spacecraft. The propellant masses are a total of 3.5t and are distributed over four propellant tanks, leading to 800kg propellant per tank, and the tanks are in a circular pattern around a central core.

Structure proposal and results

The initial design proposal is a honeycomb sandwich panel and they are load-bearing members that support the four propellant tanks. From this model, the final design is expected to meet the static, modal frequency, and failure index requirements. The options of increasing the face sheet thickness or doubling of core thickness at tank mounting points or embedding a hollow rectangular pipe inside the core do not meet the stiffness requirements. The final option presented to meet the stiffness requirements was an addition of high inclination struts

(at 60°) as shown in Figure 3.2. The propellant tanks are connected to the panel and the strut at the tank attachment zones as seen in the image [20][21].

The optimization technique used in this study was an iterative step-wise increment of the design parameters. This manual sizing modification included the face sheet thickness, core thickness, strut thickness, and angles followed by a best-fit curve. In addition, the design heritage of structures such as honeycomb panels influenced the design selection. This indicates that while the honeycomb structure is a good baseline design, it is not sufficient when considering the dynamics of a high mass offset of propellant tanks [22] [21]. Additional stiffness and load-carrying capability are provided by the struts. Another takeaway was to increase the load-bearing abilities in the longitudinal direction while considering the corresponding mass penalty.

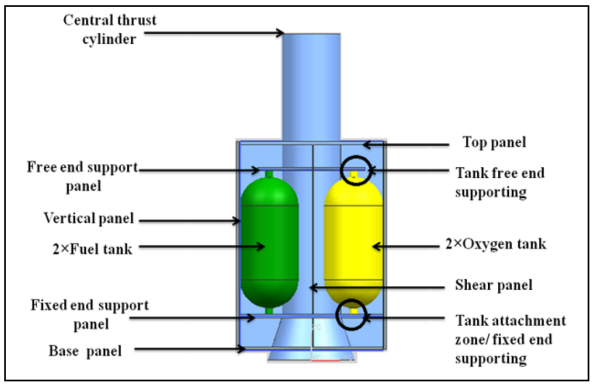

Figure 3.1: Propellant tank design for a 3.5t satellite considered in the ISRO study [20]

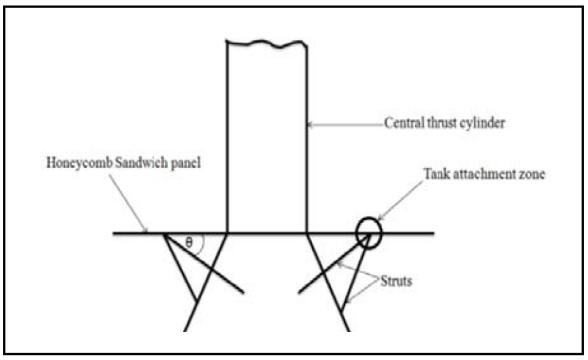

Figure 3.2: Propellant tank design solution that meets the design requirements for ISRO study [20]

3.1.2 ESM design within the Orion spacecraft

Airbus Defence and Space designed and built the Orion European Service Module (ESM) for the Artemis Moon Missions [9]. The ESM design is developed from the Automated Transfer Vehicle (ATV) project heritage.

Current design for ESM main structure

Figure 3.3 is the primary mechanical structure and serves as an interface between the spacecraft adaptor and the crew module. A high-capacity mission to the moon leads to a design with a total of four propellant tanks for 8.6t of propellant [9]. The structure is designed as two distinct machined aluminum platforms and was separated by a longeron assembly, as can be seen in Figure 3.3 and Figure 3.4.

Future flight model design for Orion main structures

The future flight model optimized proposals are proposed by Di Vita et al. [13] for the lightweighting design alternatives for mechanical structure. One of the options discussed included

substituting the lower platform machined aluminium frame with a honeycomb panel design called the "Basement" design. Another option proposed was to add struts to join the secondary structural elements to the composite lower platform. The mass savings are approximated at 161kg according to [13]. These design proposals are shown in Figure 3.5 and Figure 3.6.

Figure 3.3: ESM main structure hardware [9]

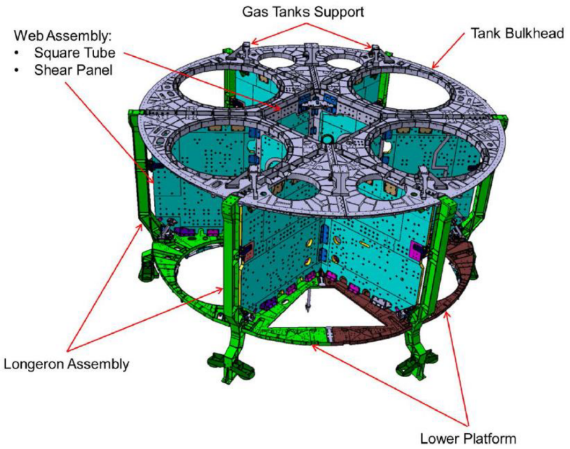

Figure 3.4: ESM main structure labelled [13]

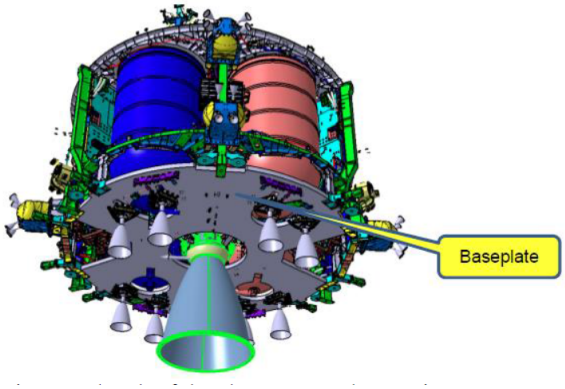

Figure 3.5: ESM basement design sketch [13]

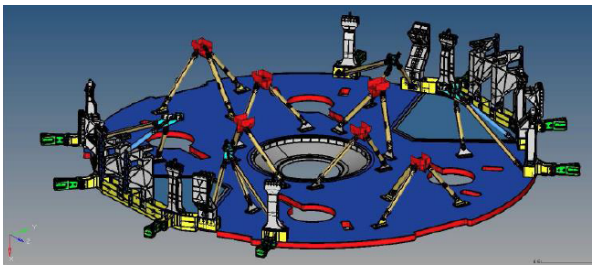

Figure 3.6: ESM basement design assembly with supporting struts [13]

3.1.3 Composite grid-stiffened and lattice structures design

There have been recent advances in the design and manufacturing of composites. One of the most recent useful structural designs is the development of grid structures in composite design. Particularly, within the grid structures, the anisogrid structures are found most suitable for composite design, given that the tailoring properties of composites can be designed to meet the requirements of the loading conditions.

One of the studies by Pavlov et al. [30], discusses a structural design case study developed using lattice and grid structures made from composite materials. The authors provide the de-

sign method that adopting composite designs instead of honeycomb and machined aluminum structures can result in significant mass savings and lead time savings. The case studies for a launcher interstage and a satellite bus central cylinder is shown in Figure 3.8

Another review by Huybrechts et al. [17] provides the developments in the design and manufacturing of grid-stiffened structures. In this study, the authors compare the performance of grid-stiffened structures against a monocoque, skin-stringer, or honeycomb sandwich structure design. Another design study by Spivey [32] proposes to use load such grid stiffened structures for primary load structures including the possibility of tank structures.

Finally, another detailed study by Vasiliev et al. [34] provides detailed equations for the design of composite grid structures design. The author has also elaborated on the manufacturing aspects and provided examples of the use of anisogrid composite designs on spacecraft and launch vehicle primary structures.

Describing Lattice type and grid-stiffened type structures

The lattice-type and grid-stiffened structures for different grids – orthogrid, isogrid, anisogrid – are shown in Figure 3.7. A basic grid-stiffened structure is a skin with stiffeners, where the stiffeners are arranged in a specific pattern. A lattice-type design is only a specific arrangement of stiffeners. The isogrid consists of hollowed-out pockets in the form of equilateral triangles. As the name suggests, the isogrid stiffness is isotropic within the plate, hence the prefix 'iso' for this type of grid structure. The continuous ribs provide stiffness, whereas the hollowed-out space allows for a lightweight design. The shape stability is provided because of the triangular trusses in the shape of equilateral triangles. The load redistribution occurs at the nodes where the sides of the triangles intersect. The NASA handbook on isogrid design [24] summarizes the properties of isogrid as with high isotropic behavior, efficient for compressive and bending loads, and availability of redundancy in the load paths. A locally thick region is created at the intersecting sides of the trusses and a tapped hole is made for attachment to secondary components.

The orthogrid cutouts have orientation of stiffeners in a rectangular pattern and the plate behavior is not isotropic. An orthogrid structure has to be thicker and/or have deeper rib structures to match the performance of an isogrid, which leads to a higher mass penalty. However, one advantage is orthogrid rectangular ribs are comparatively easier for manufacturing than isogrid structures [32]. The anisogrid structure is a pattern of stiffeners having different mechanical properties along its directions. This is more useful for composite designs as the adaptability feature of anisogrid can be matched with the directional properties of composite materials. This can lead to a design where the principal load-bearing direction has a unidirectional composite layup [34]. All three types of grid structures are extensively used in aerospace structures design and based on application, an appropriate design is chosen.

Performance of the anisogrid composite design in comparison to other structures

The comparatively conventional aerospace structure designs are a stringer stiffened panel or a sandwich structure with the primary load-carrying component as the skin. The ribs in the stiffened panel and the core in the sandwich panel primarily provide the bending stiffness, thereby increasing the buckling limit when undergoing compressive and shear loads [34].

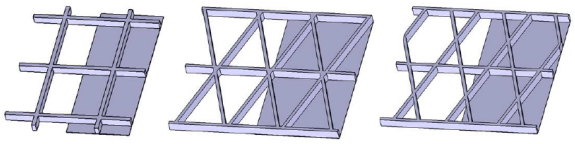

Figure 3.7: Lattice type and grid stiffened type structures for: left –orthogrid, middle –triangular isogrid, right –anisogrid [30]

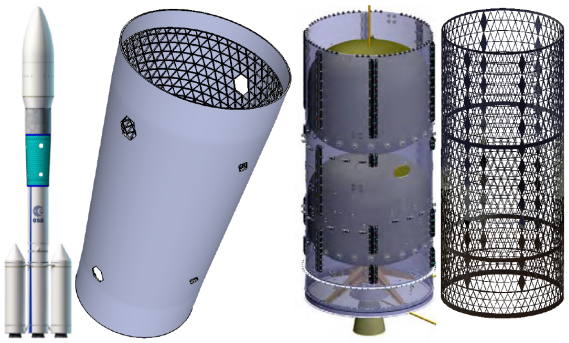

Figure 3.8: Case studies taken up by ATG for grid stiffened composite structure proposals [30]

Composites design while very useful suffer from some problems which make it less effective compared to high aerospace-grade metal alloys. These include the need for plies in laminate to avoid failure in transverse directions, matrix cracking, delamination, or higher bearing stresses at a joint. These features typically lead to a low volume fraction of fibers, under-loading of the fibers in the longitudinal direction, and large strains leading to crack formations in the laminated skin. Thus if a higher fiber fraction could be achieved in the composite, then the fiber under-loading factor could be greatly reduced. This would lead to a design with higher stiffness and strength performance. This results in a situation where if the design load case can fit the advantages of such a composite grid structure and downplay the disadvantages, then the design of such grid structures could be very useful. In particular, the anisogrid composite structure consisting of the helical and circumferential ribs coupled with a higher fiber volume fraction will lead to a higher load-carrying capacity. The presence of skin on such a structure is optional, however, if functionally required, then can be added by manufacturing using filament winding techniques [34] [33] [17] [19].

One of the significant advantages of anisogrid systems is the shape stabilization of a cylindrical central core. The presence of helical and circumferential ribs on a cylindrical anisogrid composite structure will lead to two direct consequences. The axial compressive load due to the spacecraft payload satellite acting on the top interface of the kick stage will be transferred through the helical ribs as tensile loads on the circumferential ribs. Thus, even if there are minor imperfections present on the circumferential ribs, they tend to be circular after loading. The experimental values are then closer to the theoretically predicted values, and as current research shows, there are usually no knockdown factors considered. This is not the case with a metal or skin-based cylindrical structure as the presence of shell imperfections leads to large knockdown factors [34] [33] [29] [24].

Examples of the anisogrid composite design proposals

The design case study [30] that focused on the interstage of a rocket and the central cylinder construction of a satellite bus, is shown in Figure 3.8. The first case study involves the rocket interstage, where a grid-stiffened structure is proposed. The second case study of the satellite bus proposes a lattice grid-stiffened structure for the satellite's central core. The authors

report about 25% savings on mass and 30% savings on manufacturing costs can be achieved by switching to proposed composite designs [30].

The aluminium isogrid structure that had been used on the Titan, Delta launch vehicle structures, was replaced by a composite grid-stiffened structure developed by the Air Force Research Laboratory. The composite structure was nearly 61% lighter, 300% stronger, and 1000% stiffer than the aluminum structure that was replaced [17]. Another study compared the fairing designs using a composite grid-stiffened structure and a honeycomb sandwich structure, and the new composite design was 28% stiffer leading to a larger payload envelope. The grid structure also had a 39% higher first modal frequency so the fairing acoustic damping was increased [17].

Along with fairings and launch vehicles, such designs have been flown for spacecraft as well. The spacecraft architecture with anisogrid structure can be seen in Figure 3.9. The structure is the load-bearing member for the satellite architecture, and the equipment and payloads are mounted on the outer surface of the platform. Propulsion tanks and engines are present on the inside of the structure. Another variation of the design can be seen in Figure 3.10 which shows the Express 2000 central core lattice structure. It can be seen that there are additional locally reinforced axial ribs for load carrying from the side edges to the upper and bottom interfaces [34].

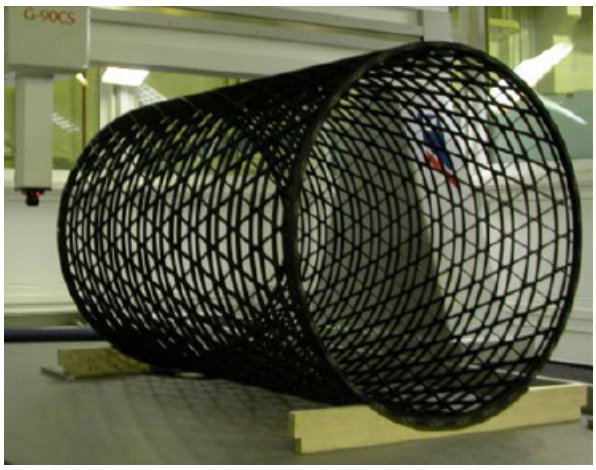

Figure 3.9: Central lattice composite structure for satellite architecture [34]

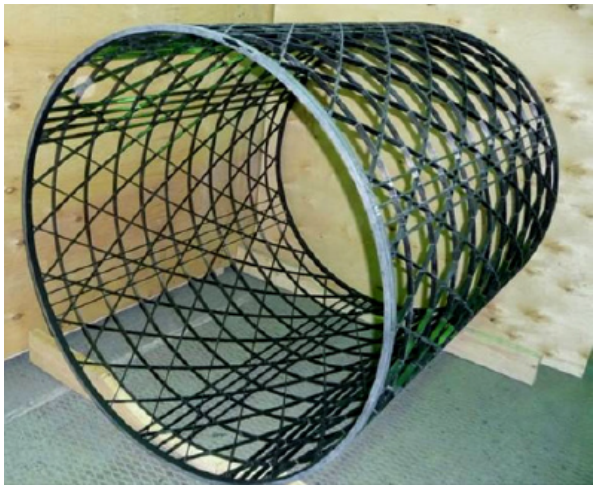

Figure 3.10: Express 2000 central core composite structure [34]

3.1.4 ArianeGroup proposal for the black upper stage

Finally, at ArianeGroup, composite-based designs for the upper stage of the launchers are being evaluated. ArianeGroup GmbH and MT Aerospace are jointly working under an ESA contract on the PHOEBUS project (Prototype of a Highly Optimized Black Upper Stage) [14][2].

Composite Upper Stage and benefits

The final goal of the project is the development of a fully composite-based upper stage called Icarus for the Ariane 6 launch vehicle. The development process is outlined in Figure 3.11. The intermediate design step is the PHOEBUS project and the project mounted on the Ariane 6 launch vehicle is seen in Figure 3.12. The current version of the upper stage is a metallic design. The black upper stage proposal leads to a significantly different methodology for design, manufacturing, and production. The benefit of the project is that it will increase payload capacity by 2t while also reducing production costs [14]. The project will lead to an increased capability of the Ariane 6 launcher [3]. The competencies being acquired for this technology would also be useful to develop a kick stage design methodology that can further push the boundaries for composite-based space structures.

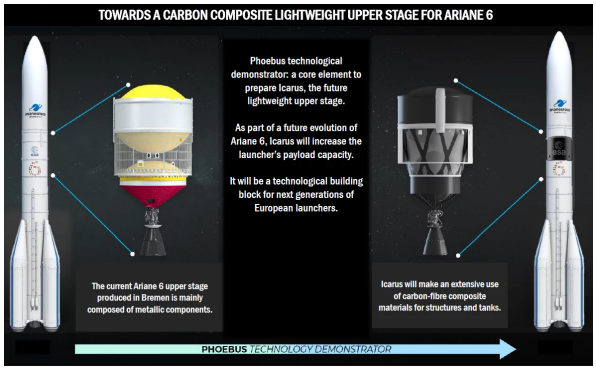

Figure 3.11: Black upper stage Demonstrator – PHOEBUS [2]

Figure 3.12: Phoebus upper stage project on Ariane 6 launch vehicle by ArianeGroup [14]

3.1.5 Literature study conclusion

From the literature study, two conclusions can be formed. There is a scope for a design methodology development that can account for the off-axis presence of propellant tanks in the design space. Instead of iterations of conventional designs of honeycomb panels or machined aluminium structures, a more organic optimization methodology can be developed. This would involve the development of design from the total design space using computational tools that account for the static and dynamic behavior of the system. The second insight is that there is a good case for developing a lightweight main structure design based on the recent developments in grid-stiffened composites. This will benefit the payload launch capabilities of the kick stage missions and provide innovative design solutions.

3.2 Development of research objectives and research questions

The thesis research objective and the research questions are derived and discussed below. The research questions for this thesis are developed in connection with the research methodologies report [22] and the literature study report [21].

3.2.1 Research objective

The primary research objective of the thesis is:

> "To achieve an innovative methodology for the design of the kick stage main structure – the central tube and the structure interfacing to the off-axis propellant tanks – by means of applying concepts of structural optimization, design of lightweight structures, and dynamics of structures." Kulkarni [22]2022(p. 7).

3.2.2 Main research question and sub-research questions

The research questions to be solved can be split into two sections: the main and the sub-research questions.

The main research question is:

"Which design methodology can be developed for the kick stage main structure, that is mass optimized and meets the design requirements, considering the off-axis mounted propellant tanks? " Kulkarni [22]2022(p. 6).

The sub-research questions based on the main research question are:

1. How would the design and qualification of the propellant tank affect the static and dynamic design of kick stage main structure?
   (a) How will dynamic levels to which the propellant tank is qualified to be used for the design of the kick stage?
   (b) What is the impact of the presence of the two fuels – oxidizer and propellant – on the design development?
2. What would be the kick stage structure design methodology?
   (a) What would be the innovative structure design methodology that will meet the design requirements?
   (b) Which optimization method and steps or combination of optimization methods would produce the most reliable and lightweight results?
   (c) What are the system-level dynamic responses and satellite interface amplifications for the structure when loaded with suitable boundary conditions?
   (d) How could the trinity principles of design, materials, manufacturing, and assembly be addressed within the design development framework?

Kulkarni [22]2022(p. 7).

The solution to the research questions is the research goal of the project. The development of the design methodology to meet this research goal is discussed in the next chapter. This includes the development of the design input parameters, followed by the structural analysis methods and its numerical formulation with finite element modeling and the results are elaborated in upcoming chapters.

Chapter 4

Methodology Description

The solution methodology for solving the research questions is discussed in this chapter. Initially, the overall methodology and the workflow are described. This is followed by details of the design input parameters, where the constraints, input loads, objectives, and variables are elaborated. The further discussion provides insight into the structural analyses including failure modes and the optimization tools used for the research problem. Thus, this provides a complete and detailed overview of the solution methodology developed and used for this project. Additionally, some individual analysis parameters are discussed in subsequent chapters where they are more relevant to the specific analysis under consideration.

4.1 Overall design methodology

The broad scope of the thesis to solve the research questions includes the implementation of topics within multiple aerospace and mechanical systems engineering disciplines. These are mentioned in a block chart Figure 4.1. The engineering disciplines including vibrations and dynamics of structures, lightweight structures design, structural optimization, finite element methods, design of composite structures, and the design of spacecraft and launch vehicle systems have been implemented in the design methodology development. A set of relevant principles of design are selected from these disciplines. This is used to develop an overall design methodology. The flowchart describing this overall design methodology is seen in Figure 4.2.

1. The project started off with understanding of the kick stage parameters and developing the research topic. This was followed by a literature study [21] and development of a project plan [22]. Combining these aspects, the design input parameters of design constraints, input loads, design objectives, and design variables were formulated. These are described in the next section on design input parameters section 4.2.

2. Two design approaches were derived from the results of the literature study. The first is the optimization methodology for the entire design space, and the second is the composite anisogrid design proposal.

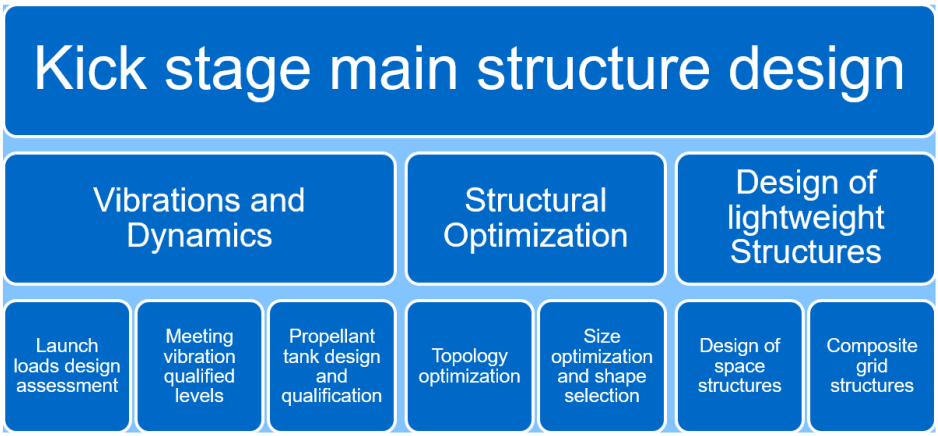

Figure 4.1: Broad academic disciplines discussed within the scope of this thesis

3. The numerical method with finite element method was selected for solving the complex input loads and developing the design optimization methodology. The details of the finite element method and formulation of the governing equations have been discussed in detail in section 4.3.

4. The first approach formulated was a combination of topology optimization, shape selection, and sizing optimization to develop a methodology for structural concept from the total design space. Each aspect of the optimization process pointed to a phase of the design cycle, starting with the conceptual design stage to the detailed design stage. The optimization implementation for structural analysis is discussed in section 4.5. The corresponding structural analysis considered for each optimization loop also increased as seen in Figure 4.2.

5. The optimization loops proposed solved the structural analysis modules within each loop, to result in an optimized converged design. For the topology optimization loop, the linear static analysis for the quasi-static loads, and the normal modes analysis for the modal frequency requirements were carried out. For the size optimization loop, along with these two, modal frequency response analysis and buckling analysis were also carried out. These optimization studies were then repeated for different input configurations that are important to the design study. The modeling details for the study and the results are given in subsequent chapters, topology optimization in chapter 5, and sizing optimization in chapter 6 and chapter 7.

6. A slightly different approach has been developed for the composite design proposal. An analytical model based on the design equations is proposed for the baseline failure modes for a lightweight design using anisogrid CFRP structures. This model is then modeled numerically using finite element methods and optimized using size optimization to account for additional loading conditions. The results of the analytical and the numerical model are described in chapter 8

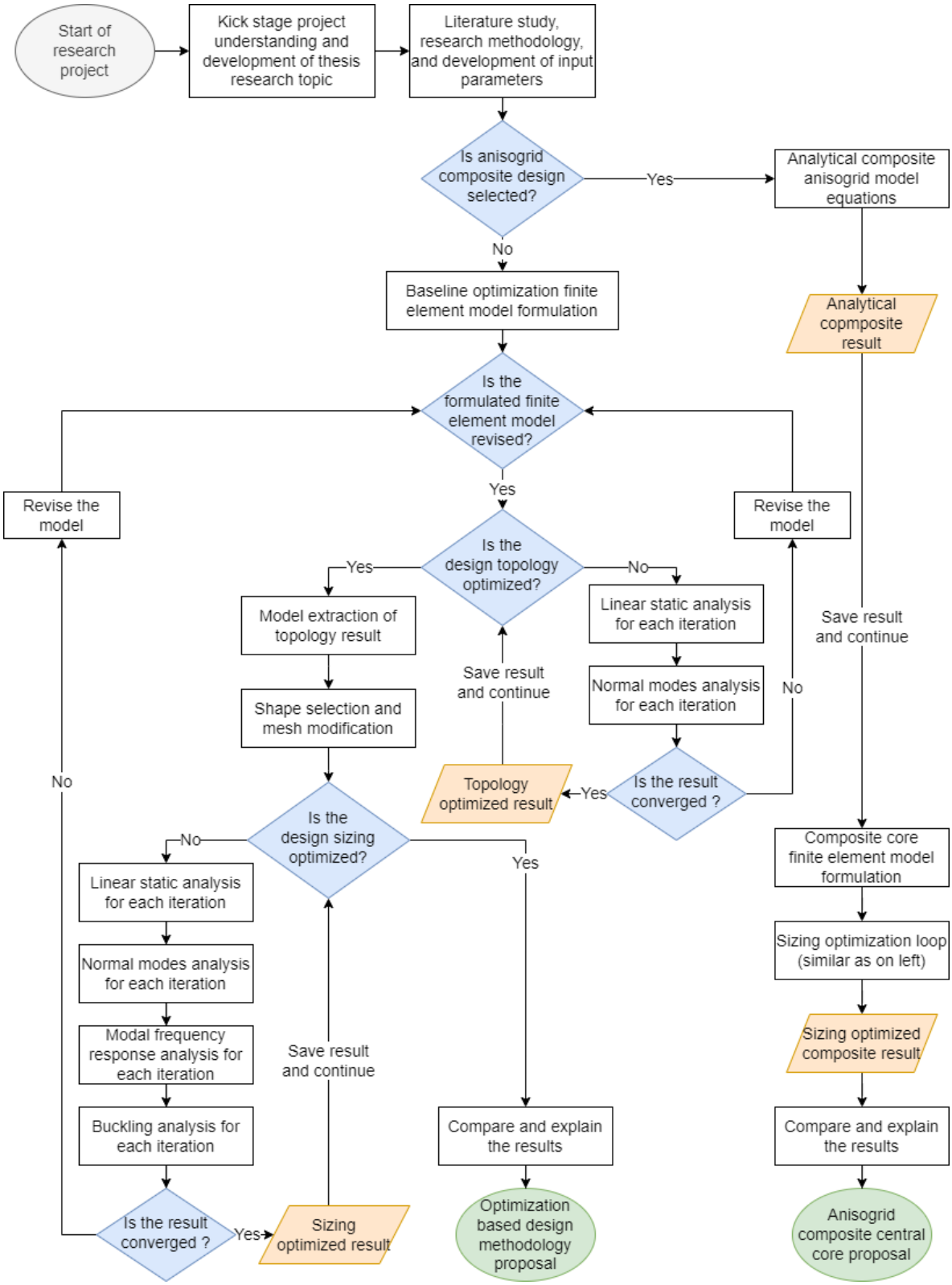

Figure 4.2: Workflow diagram for the design methodology

4.2 Design Input Parameters Development

The design input parameters for the structure design are discussed in this section. The design problem for the thesis problem statement is a structural optimization problem, with an aim to achieve a lightweight design and a methodology for the kick stage main structure. The design input parameters of constraints, input loads, design objectives, and design variables that are needed for defining an optimization problem are presented [21].

4.2.1 Constraints

The constraints include the boundary conditions and the available design space.

Boundary conditions for FE modeling

- **Bottom interface** – The bottom interface of the kick stage is bolted to the top of the upper stage using pyrotechnic separation clamp bands. This is approximated in the FEM analysis as a fixed boundary condition. For dynamic FEM studies, a corresponding enforced acceleration is given input at this interface.

- **Top interface** – The top interface is loaded with the spacecraft payload. This is modeled as a point load at a height corresponding to the center of mass of the spacecraft and is connected to the design structure using rigid elements.

Design space and volume

- **Design space availability** – The total available design space is the space between the central core and the fairing of the Ariane 6 launch vehicle. The nominal clearance of the propellant tank on the near and the far side with respect to the central cylinder is about 100mm and 213mm respectively. The design space is highlighted in grey color as shown in Figure 4.3.

4.2.2 Input loads

Masses considered for the structure design

- **Propellant tank loads** – The filled bi-propellant tanks are the primary loads on the kick stage. The volume of each propellant tank is 862litres. The mass for the tanks is calculated by considering this volume, the filling ratio of 97%, and the density of the propellants. The heavier density of oxidizer results in a mass of 1252kg per tank, while the propellant results in a mass of 777kg per tank. This difference in the filled tank masses for the propellant and the oxidizer impacts the design of the resulting structure. The total mass considering two pairs of each of the propellant tanks is 4058kg.

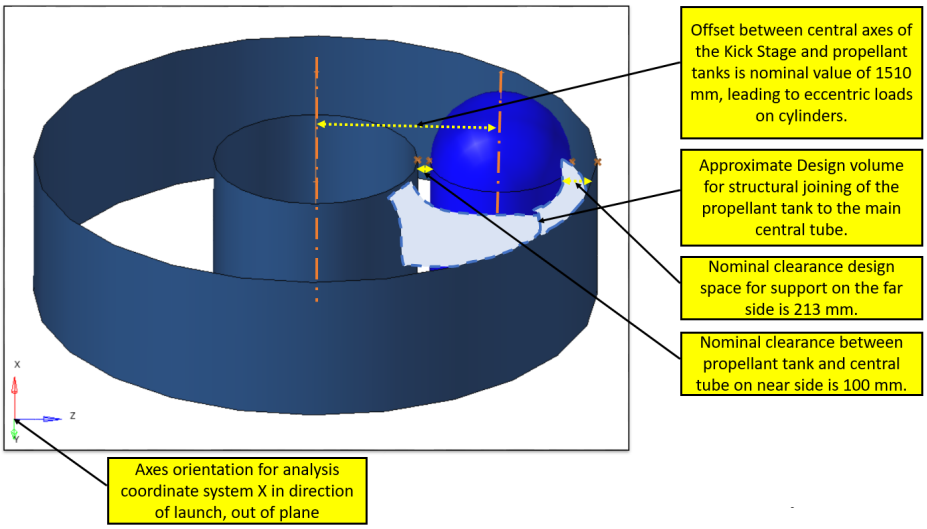

Figure 4.3: Approximate CAD sketch of Kick Stage indicating the design space.

- **Design payload mass** – The maximum payload that a mission can possess for the Ariane 6 with Ariane 64 configuration varies as per the altitude of the orbit. The Ariane 6 launcher has the ability to transfer payloads of mass 20t to Low Earth Orbit (LEO), or 11.5t to Geosynchronous Transfer Orbit (GTO), or 8.6t to lunar transfer orbit, or 6.9t for Earth escape missions [6]. The preliminary studies done at ArianeGroup GmbH indicate that science missions or payload delivery missions to lunar transfer orbit or geostationary transfer orbit missions stand to be most benefited from such an additional kick stage [5]. Thus, considering this study, we get a spacecraft payload load of 4.2t on the kick stage.

Quasi-static loads (QSL) accelerations

- **QSL accelerations** – The entire payload has a specification of quasi-static loads (QSL) on the structure which is a resultant acceleration calculated for the Ariane 6 launcher. The QSL considered in the analysis is the launcher accelerations with an additional design factor. The acceleration for the longitudinal direction is 9g (1g=9.81 m/s^2) and for the lateral direction is 5g. These accelerations were used for checking the stresses and calculating the structure compliance while evaluating the optimization loop results.

Dynamic loads

- **Dynamic loads** – During the launch, the effects of aerodynamics and propulsion systems cause dynamic loads on the payload. The sine dynamic input at the spacecraft interface for the Ariane 6 launch vehicle is given as 1g amplitude for longitudinal direction and 0.8g amplitude for lateral direction within the frequency from 2Hz to 100Hz. The profile for this excitation is mentioned in the Appendix B. As per the user manual [6] the random vibration for frequencies below 100Hz is covered within this same sine load specification.

4.2.3 Design objectives

The design objectives are the targets of the design methodology that the resulting design must satisfy.

Strength requirements

- **Yield strength requirements for main structure** – The kick stage structure joining the central tube and the propellant tank should not exceed the ultimate tensile strength of the material, and so should have a positive margin of safety for qualification QSL levels applied to the structure.
- **Margin of safety requirements** – A factor of safety of 1.2 is observed for the main structure design, while a smaller value of 1.1 is observed for the standardized qualified components. This factor of safety requirement and an additional positive margin of safety is expected to be fulfilled by the design.

Buckling requirements

- **Buckling** – The compressive loads on the main structure including the payload and the propellant tanks should not lead to the buckling of the structure. Hence, the buckling modes of the design are calculated and the first buckling mode is of particular interest.

Stiffness requirements

- **First modal frequency requirements in longitudinal and lateral directions** – The first modal frequency of the structure has to be above a given mandatory requirement for avoiding resonance due to the low-frequency excitations of the launch vehicle. The kick stage to the launcher structure interface is assumed as fixed boundary condition. For the longitudinal direction, 15Hz is the minimum requirement for the first mode of the structure. For the lateral direction, 13Hz is the minimum requirement for the first mode of the structure.

Dynamic amplification limiting values

- **Peak acceleration and Qualified levels** – The propellant tanks are qualified to 9g axial acceleration qualification levels. This qualification is carried out when the propellant tank is loaded along its axis. The off-axis impact of the kick stage configuration would tend to increase the amplification on the propellant tank. This is considered in the design process. It is demonstrated that the peak acceleration on the propellant tank cog do not reach these values for given flight-level load input. (In cases where the acceleration exceeds this value for a given frequency range and the corresponding mass penalty to modify the design is high, then relaxation by notching or reduction of qualification margins at that frequency range can be done.)

- **Effect of multiple propellant tanks** – The configuration of four propellant tanks causes a high resonance of the main structure as the modal frequencies are close to the vibration peaks of the launch vehicle. The resulting higher amplification is taken into account for the studies.

4.2.4 Design variables

Design structure type

- **Structure design and visualization** – The result of the design cycle should correspond to a design type and a design methodology that meets the constraints and objectives. This includes the methodology or approach for the design development and the design solution proposed.

Mass of the feasible design

- **Mass objective** – The objective of the optimization exercise is to minimize the mass of the entire structure.

4.3 Structural analysis by FEM numerical method

The design methodology developed is a combination of structural analysis steps carried out to validate the design against failures. The analyses would take into account these design variables, formulated so as to meet the design objectives while accounting for the input loads and constraints. For complex load cases, analytical methods are often insufficient. Hence, a numerical method is proposed. The numerical methods are solved using finite element method (FEM) packages.

The FEM methodology involves representing a continuous structure as a combination of grid point nodes connected by discrete elements. All the nodes are associated with motion along the six degrees of freedom (three translational and three rotational) and are commonly called by variable $\{u\}$. The elements provide the necessary stiffness to the structure and transmit the motion from one node to another. The stiffness matrix of each element usually represented using variable $[K]$, depends on the defined material properties, type, and geometry of each element. The input load vectors are also provided as input to one or multiple nodes and is represented by $\{p\}$. The nodal connections between the elements are used to determine the global stiffness matrix, such that it forms a series of equations that connects the deformation of all nodes. The boundary conditions are applied so as to remove fixed degrees of freedom and this leads to a solvable system of equations. The results of the nodal degrees of freedom are obtained by the relation between the input loads and the loading parameters. This governing physics equation in its matrix form is then used to solve the numerical problem, where the loads and the element stiffnesses are known, and the nodal displacements are unknown [25]. For a simple linear static analysis, the process along with the governing equation is described in Figure 4.4.

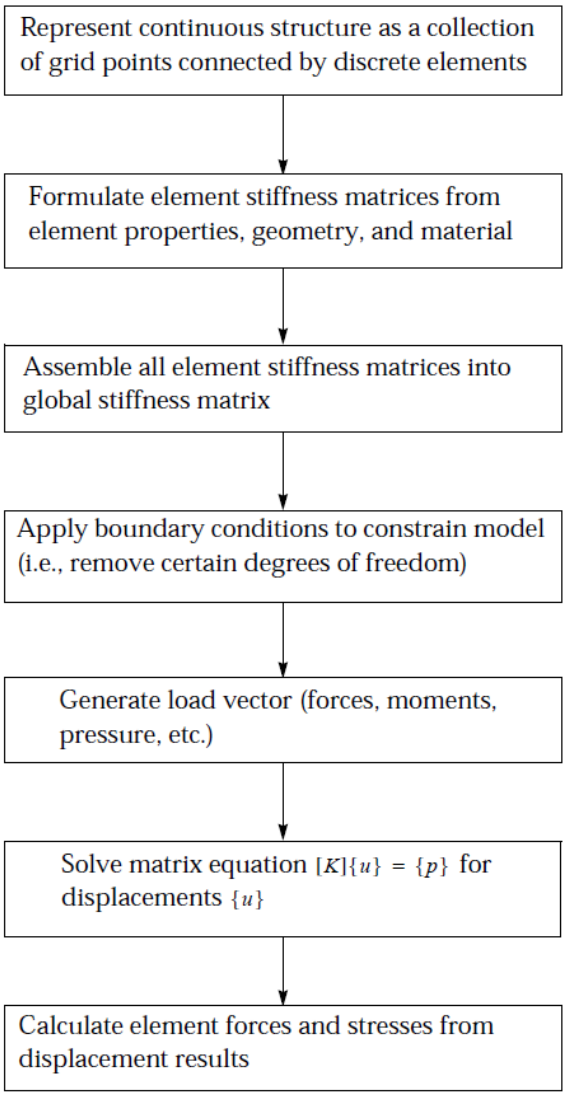

Figure 4.4: FEM process overview - for linear static analysis [25]

There are many commercial FEM solvers such as Nastran, Abaqus, Ansys, OptiStruct, etc. The FEM packages of MSC Nastran and OptiStruct are available within the scope of the project, and they have been proven to provide a high degree of confidence in the aerospace structure design and optimization [12] [21]. The solved analyses and their formulation in FEM are discussed in the next section.

4.3.1 Static load analysis and failure modes

The quasi-static acceleration loads acting on the kick stage are time-independent and so there is no dynamic excitation present. The linear static analysis is the structural analysis required for this load assessment, as the deformations are small and additionally, the material and geometric non-linearities are not considered.

In the FEM method, the mathematical matrices of the input vectors $\{p\}$, element stiffness $[K]$, and the nodal displacements $\{u\}$ are related. The input load matrix $\{p\}$ contains the applied loads' data including the accelerations or forces applied on the model. The linear static analysis governing equation in FEM is given by Equation 4.1. The unknown displacements $\{u\}$ for the linear static equation are solved by the solver using the Gauss elimination method. The strain and stress are calculated by arithmetic operations on the displacement results based on the material properties and the type of elements formulated in the mesh. The solver-solution packages MSC Nastran SOL 101 Linear statics and OptiStruct Linear static can be used for linear static analysis [25]. The workflow chart for linear static analysis is seen in Figure 4.4.

$$[K]\{u\} = \{p\} \tag{4.1}$$

Yield stress failure criterion

The stresses developed due to these loads are tested against failure criterion for design validation. For isotropic materials, yield stress is a common limiting failure indicator, as this is the limiting value of elastic behavior, and stress exceeding it will result in plastic deformation of the structure. The Von Mises failure criteria for three-dimensional stresses is a commonly used failure criterion given by Equation 4.2. The stresses in non-principal directions are denoted by σ_{xyz} are the normal stresses and τ_{xyz} are the shear stresses. A factor of safety (FOS) is applied as it accounts for uncertainties in material properties and manufacturing tolerances [19]. The limiting stress constraint value within the optimization loop includes this FOS.

$$\frac{1}{\sqrt{2}}\sqrt{(\sigma_x - \sigma_y)^2 + (\sigma_y - \sigma_z)^2 + (\sigma_z - \sigma_x)^2 + 6\left(\tau_{xy}^2 + \tau_{yz}^2 + \tau_{zx}^2\right)} \leqslant \frac{\sigma_Y}{FOS} \tag{4.2}$$

Composite design failure criteria

There are several composite failure criteria available due to recent advances. However, for coarse modeling and first-order calculations, the Tsai-Hill approximation for stress on 2D ply is a good failure criterion [19]. For a single ply under plane stress with ply axes xy the equation is as shown in Equation 4.3. The failure along fibers is represented by strength X, the failure along matrix is represented by strength Y, and the shear failure is represented by S [19].

$$\frac{\sigma_x^2}{X^2} - \frac{\sigma_x \sigma_y}{X^2} + \frac{\sigma_y^2}{Y^2} + \frac{\tau_{xy}^2}{S^2} \leqslant 1 \tag{4.3}$$

4.3.2 Buckling load analysis and failure modes

The buckling phenomenon is defined as the deformation and drop in the load-carrying capacity of the structure, occurring due to compressive or shear loads acting on the structure. The buckling of the kick stage main structure occurs due to compressive loads acting on it, primarily the payload on top of the structure and the propellant tanks on the sides. The Euler buckling formula is valid for slender beams. However, for the cylindrical structures

such as the main cylinder of the spacecraft, the more conservative equation of Equation 4.4 is used, as given in [10] and derived by Von Karman and Tsein [35] in their work.

$$\sigma_{\text{shell}} = \frac{E}{\sqrt{3\,(1-v^2)}}\frac{t}{R} \tag{4.4}$$

This equation only gives the theoretical buckling load. However, in practice, the experimental failure loads are lower than this, primarily due to manufacturing imperfections of the cylinder. The empirical formulae of NASA SP 8007 for the cylindrical buckling loads are generally used as knock down factor given by Equation 4.5 given in [29].

$$\frac{P}{P_{cf}} = 1 - 0.902\left(1 - e^{-\frac{1}{16}\sqrt{\frac{R}{t}}}\right) \tag{4.5}$$

However, these reduction factors are provided only for smooth cylinders without any additionally loaded side panels or similar structures. Using the FEM method, the buckling failure of these attached components to the central cylinder can also be detected.

The buckling governing equation in FEM is solved as a typical eigenvalue problem, defined by accounting for the geometric non-linearity solution. The linear buckling equation is given by Equation 4.6 [11].

$$\left([K]^{\text{Mat}} + \lambda_{\text{cr}}[\hat{K}]^{\text{Geo}}\right)\mathbf{v} = \mathbf{0} \tag{4.6}$$

Here, the $[K]^{\text{Mat}}$ is the material stiffness, the $[\hat{K}]^{\text{Geo}}$ is the geometric stiffness matrix, and $\mathbf{v}$ is the buckling mode shape vector. This is an eigenvalue problem with the stiffness matrix $[K]$. The buckling load is the eigenvalue for which the geometric stiffness and the material stiffness matrices cancel out. Re-substituting the values, the buckling mode shape vector is found, which shows the relative displacements of the nodes in the structure.

Both solver-solution packages of MSC Nastran SOL 105 Linear buckling and OptiStruct Linear buckling can be used for buckling analysis. Additional stiffening members for the structure would also be assessed based on this result. A more accurate and computationally expensive buckling solution is given by a non-linear FEM buckling solution as it accounts for material non-linearity and post-buckling behavior. However, this analysis is beyond the scope of this project.

4.4 Dynamic analysis

The dynamic analysis method follows a similar FE development methodology as seen in Figure 4.4, however, the loading conditions and the governing equations are significantly different. The major difference is that the applied dynamic loads are a function of time or frequency. Consequently, this load induces time or frequency-varying responses.

A representation of a dynamic system with a single degree-of-freedom is a spring mass damper system as seen in Figure 4.5. The components of this system are the mass, damper, spring,

and applied load. As the mass m is displaced by $u(t)$ due to the externally applied load $p(t)$, there are internal forces generated in the system. Equating the internal and external forces the equilibrium equation is a second-order linear differential equation at each instant given by Equation 4.7[27].

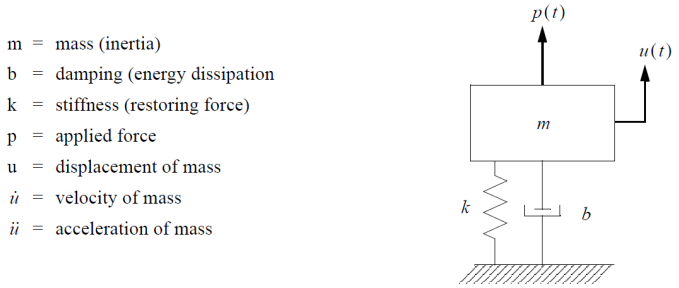

Figure 4.5: A spring mass damper system with single degree-of-freedom[27]

$$m\ddot{u}(t) + b\dot{u}(t) + ku(t) = p(t) \tag{4.7}$$

where,
$m\ddot{u}(t)$ is the inertia force proportional to the mass and the acceleration
$b\dot{u}(t)$ is the damping force proportional to the damping parameter and the velocity
$ku(t)$ is the induced elastic or spring force proportional to the stiffness and the displacement
$p(t)$ is the applied loads on the system

The objective of dynamic analysis is the solution to this equation of motion Equation 4.7, leading to the results for displacements, velocities, accelerations, or stresses as a function of time. Depending on the presence or absence of external loads $p(t)$ on the system the dynamic analysis could be forced or free vibrations respectively. If the damping parameter is set to zero, the vibration analysis is undamped. Depending on the damping values, the system could be critically damped or overdamped, or underdamped. The natural frequencies of the structure are calculated by free undamped vibration analysis. The forced vibration analysis typically of concern for mechanical structures design is underdamped systems.

The natural frequency of every structure is an inherent dynamic property defined by structural stiffness and mass properties. Calculation of this is important to understand the stiffness of the structure and the frequencies at which the natural vibration of the structure occurs. During the launch, external dynamic loads act on the entire launcher due to launch acceleration, the launcher staging, engine noise, thrust, and aerodynamic turbulence. The total dynamic loads are then characterized as a vibration signal applied at the kick stage to the upper stage interface. The dynamic loads acting on the structure are present at nearly the same frequencies as the natural frequency of the structure, this can lead to resonance where the observed amplification on the structure is higher than the qualified or safe operational value. Thus, the calculation of the amplification observed on the propellant tanks is a two-step process. In the first step, it is necessary to do a free vibration modal analysis to extract the important modes and frequencies of the structure. In the second step, a forced response analysis is done over a particular frequency range. This combined modal and dynamic analysis procedure to meet the dynamic requirements is shown in flowchart Figure 4.6.

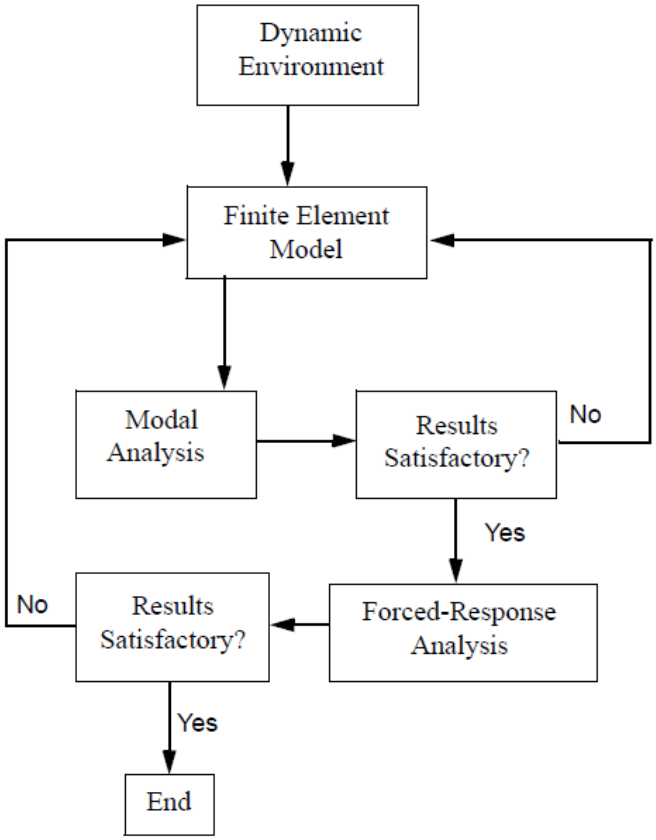

Figure 4.6: Dynamic analysis process overview for methodology used[27]

4.4.1 Modal frequency analysis

The modal analysis is formulated as a free undamped vibration problem in which the natural frequencies of the structure are determined. Thus, the external forces and the damping is not considered. The deformed shape developed at a particular natural frequency of vibration is the mode shape of the structure at that frequency. Rewriting the equation of motion into a matrix form for the free undamped vibration case, we get Equation 4.8

$$[M]\{\ddot{u}\} + [K][u] = 0 \tag{4.8}$$

where the term $[M]$ is the mass matrix that contains the information for the structural mass and the inertia and is defined for each element. The formulation depends on the geometry and the property details of the element. The term $[K]$ is the stiffness matrix.

This equation can be solved by converting it into an eigenvalue problem with a harmonic solution of the form Equation 4.9

$$\{u\} = \{\phi\} \sin \omega t \tag{4.9}$$

where the term $\{\phi\}$ is the eigenvector equivalent to the mode shape and the term ω is the circular natural frequency. The resulting equation after simplification results to Equation 4.10

$$\left([K] - \omega^2[M]\right)\{\phi\} = 0 \tag{4.10}$$

This solver has to determine the eigenvalue problem solution which depends on the mass matrix and stiffness matrix of the structure. The non-trivial solution for the eigenvalue problem is given by Equation 4.11

$$\det([K] - \omega^2[M]) = 0 \tag{4.11}$$

This equation is zero only for a certain set of eigenvalues ${\omega_i}^2$. For each eigenvalue, there is a corresponding eigenvector ϕ_i that satisfies Equation 4.12. Each eigenvalue and corresponding eigenvector define the free vibration mode of the structure for each i-th value.

$$\left([K] - {\omega_i}^2[M]\right)\{\phi_i\} = 0 \qquad i = 1, 2, 3, ... \tag{4.12}$$

Finally, the modal frequency in Hz is given by the relation between the natural frequency and circular frequency given by Equation 4.13.

$$f_i = \frac{\omega_i}{2\pi} \tag{4.13}$$

There are different methods available for the extraction of eigenvalues, and the algorithm details are beyond the scope of this project. The solver-solution packages of MSC Nastran SOL 103 Real eigenvalues and OptiStruct Normal modes can be used for modal analysis evaluation and interpretation of results [25].

4.4.2 Dynamic frequency response analysis

The dynamic analysis for the input excitation at the kick stage interface is carried out using frequency response analysis. The profile and the magnitude of the sine load at the kick stage launcher interface are given in Appendix B. There are two methods available, direct frequency response analysis and modal frequency response analysis. The direct method directly solves the coupled equations of motion, whereas the modal method utilizes the mode shapes calculated in normal modes analysis. The modal method is more useful for large FE structures as the number of equations is reduced because the modes of the structure are already known. The dynamic response for kick stage is calculated using the modal frequency response analysis method.

The damped forced vibration equation in matrix form is given by Equation 4.14. The harmonic load is written as a complex vector form instead of the usual trigonometric form. The use of a complex number representation results in output defined by a real-imaginary or magnitude-phase result. The magnitude at each frequency is the output of interest. The phase difference represents the peak response difference between the output measurement and the input excitation. It has to be noted that here ω_f denotes the forcing frequency of excitation at which the governing equation is solved.

$$[M]\{\ddot{x}(t)\} + [B]\{\dot{x}(t)\} + [K]\{x(t)\} = \{P(\omega_f)\}e^{i\omega_f t} \tag{4.14}$$

A harmonic equation of the form Equation 4.15 is assumed to satisfy the damped forced vibration equation for the direct frequency response method.

$$\{x\} = \{u(\omega_f)\}e^{i\omega_f t} \tag{4.15}$$

This results in a system of equations Equation 4.16 for the forcing frequency ω_f and is then solved using arithmetic complex value methods[27].

$$\left[-\omega_f^2 M + i\omega_f B + K\right]\{u(\omega_f)\} = \{P(\omega_f)\} \tag{4.16}$$

The modal frequency response method adds an intermediate step where the variables are transformed from physical coordinates $\{u(\omega_f)\}$ to modal coordinates $\{\xi(\omega_f)\}$ by the transformation Equation 4.4.2, where $[\phi]$ is the mode shape matrix.

$$\{x\} = [\phi]\{\xi(\omega_f)\}e^{i\omega_f t} \tag{4.17}$$

Substituting into the governing equation and pre-multiplying with the transpose of the mode shape matrix $[\phi]^T$ the final equation for the modal frequency response function is given by Equation 4.18

$$\left[-\omega_f^2[\phi]^T[M][\phi] + i\omega_f[\phi]^T[B][\phi] + [\phi]^T[K][\phi]\right]\{\xi(\omega_f)\} = [\phi]^T\{P(\omega_f)\} \tag{4.18}$$

The modal space vectors for each ith mode are given by the corresponding mode shape matrix $[\phi_i]$. This defines the modal mass matrix as $m_i = [\phi_i]^T[M][\phi_i]$, the modal stiffness matrix as $k_i = [\phi_i]^T[K][\phi_i]$, the damping matrix as $b_i = [\phi_i]^T[B][\phi_i]$, and the modal force matrix as $p_i = [\phi_i]^T\{P(\omega_f)$ for each mode. Depending on the type of damping – modal, viscous, or structural – the formulation of the damping matrix in FEM changes.

This results in the governing equation in modal space as Equation 4.19

$$-\omega_f^2 m_i\xi_i(\omega_f) + i\omega_f b_i\xi_i(\omega_f) + k_i\xi_i(\omega_f) = p_i(\omega_f) \tag{4.19}$$

The results for the modal responses are then calculated in modal space given by Equation 4.20.

$$\xi_i(\omega_f) = \frac{p_i(\omega_f)}{-m_i\omega_f^2 + ib_i\omega_f + k_i} \tag{4.20}$$

The responses are converted back from modal space to physical space by

The total response of the structure is a linear combination of solutions generated at all modes given by Equation 4.21. This total response for acceleration at each frequency is the result of interest for the modal frequency response analysis.

$$x(\omega_f) = \sum_{\mathrm{i}=1}^{\mathrm{N}} \phi_{\mathrm{i}} \xi_i(\omega_f) \tag{4.21}$$

A frequency response function (FRF) $H(\omega)$ is the ratio of the response of a structure $x(\omega)$ (displacement, velocity, acceleration) to its input excitation force $P(\omega)$. For example, the FRF for the displacement is given by Equation 4.22. A different FRF is calculated for each frequency and in numerical methods of FEM it is calculated as the response to a unit magnitude input load.

$$H(\omega) = \frac{x(\omega)}{P(\omega)} \tag{4.22}$$

The final equation for modal frequency response analysis Equation 4.19 is similar to the direct frequency response analysis Equation 4.16. However, the additional computational saving is that it is calculated only at specific frequencies where the modal analysis has calculated that the modes are present. A structural damping of 3% is formulated for the kick stage design procedure and this card is considered in the analysis. This explains the detailed equations of the flow chart for the dynamic methodology developed as seen in Figure 4.6. Thus, the result of the modal frequency response analysis is that it gives the peak responses observed for an input excitation and is calculated at specific modes. The peak acceleration responses are calculated at multiple 'sensor' nodes such as the propellant tanks are considered for further analysis. The solver-solution packages of MSC Nastran SOL 111 modal frequency response and OptiStruct modal frequency response can be used for the dynamic response analysis for sine input.

4.5 Optimization development methodology

The structural optimization methodology is discussed in this section. This involves the description of the optimization problem, the density method used in topology optimization, and the process methodology within FEM. Finally, a study comparing the performance of different solvers is mentioned.

4.5.1 Structural optimization

Structural optimization plays a crucial role in the development of a lightweight design and is an important part of the proposed design methodology. An optimization problem is expressed below.

Minimize $f(x)$

Subject to

$g_i(x) <= 0$ for $i = 1, ..., m$

and

$h_j(x) = 0$ for $j = 1, ..., l$

where,

$x = (x, x_1, ..., x_n)$

$f(x) =$ objective function

g_i are the inequality constraints and the h_j are the equality constraints[23].

In the case of structural optimization, the objective is a goal to be usually minimized. Typical examples are minimization of mass or compliance of the structure. The structural analysis described in earlier sections is usually solved within an optimization loop iteration. The results of the structural analysis such as frequency, stress, compliance, and mass, are exported from the solver to the optimizer. These results are design parameters that have to satisfy the equality or non-equality constraints. The detailed FE formulation of structural optimization is discussed in greater detail in the literature study [21]. A brief discussion on these details is provided in Appendix A and a flowchart in section A.2.

There are three primary three types of optimization techniques. These include sizing (or size), shape, and topology and they are useful in distinct stages of design development as seen in Figure 4.7. In the concept design phase, the topology optimization study results describe the regions in the entire design space that is relatively important to meet the design objective. This was followed by the basic design stage where particular shapes have been identified from the topology result. Finally, in the detailed design stage, the sizing optimization results provide the optimized dimensions of the structure. The scope of mass optimization for lightweight design is maximum for the concept design phase and continues to decrease as the design progresses towards the detailed design phase [21].

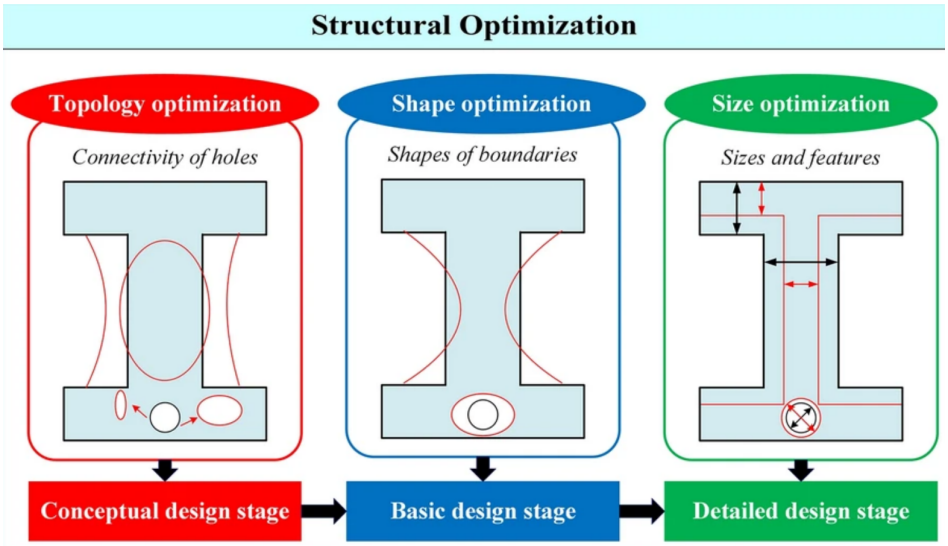

Figure 4.7: Structural optimization processes overview [16]

4.5.2 Topology optimization by density method

Topology optimization has been used to determine the critical areas in the total design space of the kick stage. The FEM solver input is the entire design space available for the main structure design. The density method is based on the artificial material approach devised by Bendsøe [8] and is also called the Solid Isotropic Material with Penalization method (SIMP). This includes an assumption that the entire design space mesh has an artificial homogeneous material and the material density can vary between 0 and 1. The material properties are proportional to this relative density. A power law relation is provided to the solver that relates the artificial density and material property, such as Young's modulus [21].

In the design space with a nominal full density ρ_0 and full Young's modulus E_0 that for the kick stage corresponds to aerospace grade aluminium alloy. The design space artificial material parameters for topology optimization are given by density ρ and Young's modulus E. The equations Equation 4.23 and Equation 4.24 relate the two components as shown below.

$$\rho = \rho_0 x \tag{4.23}$$

$$E = E_0 x^p \tag{4.24}$$

where x is the design variable and p is the penalty factor.

For this project, the design variable is the total mass fraction and the value of 0.3 is assigned. The penalty factor of 3 is selected as it is considered the default for topology optimization, while the value can vary between 2 to 5. This results in a set of optimization iterations to meet the design objective while being within the design constraints. For the design variable mass fraction of 0.3, the first iteration is where the entire design space has the artificial density 0.3 times the original design input mass. This first iteration is not the optimized structure as every individual element in the optimization space has a uniform 0.3 density. Across iterations, the individual elemental densities are redistributed from regions where the material is not required (individual element density close to 0, i.e. no material present in that element) to where elements are required (individual element density close to 1, i.e. material fully present in that element).

After reaching a convergent solution of the optimization, the non-critical areas get assigned a lower element density < 0.1 while the critical regions leading to the desired objective until convergence have a higher element density 1.0 [26]. The output has then been exported into a new mesh for further analysis for the next design phase. The detailed objective and constraints that lead to the solution are discussed in further chapters. The FE formulation of structural optimization is discussed in greater detail in the Literature Study [21] and a summary of the same is attached as Appendix A.

This density method for topology optimization is used by both MSC Nastran and OptiStruct. The topology optimization data entry cards are TOPVAR card in MSC Nastran and DPTL card in OptiStruct. Additional constraints such as manufacturing conditions, symmetry, changes in the penalty factor, maximum or minimum size, etc. can be done for these entry cards [26] [1].

4.5.3 Performance of solvers for structural optimization

A comparative study of the performance of the FEM solvers of MSC Nastran, OptiStruct, and Genesis for optimization problems was carried out by Choi et al. [12]. The performance was graded based on the computational time and the optimum solution quality. The linear static analysis load case was carried out for shape, size, and topology optimization methods. The paper recommends that OptiStruct solver provides the best quality solutions for a topology optimization problem. The paper also recommends that MSC Nastran provides the best quality solutions for a shape optimization problem. Finally, the paper also evaluated the solvers for a large-scale example and concluded that similar objective function results were provided by the three solvers. However, OptiStruct had a better computational time compared to MSC Nastran (46 minutes for OptiStruct compared to 5 days and 9 hours 30 minutes for MSC Nastran) [12] [21].

Due to this data, the OptiStruct solver has been used for the research project. The data entry cards for optimization and structural analysis are nearly identical in both MSC Nastran and OptiStruct. The similar structure of the input files – .dat in MSC Nastran and .fem in OptiStruct – also makes the input coding easier and interchangeable with minimum effort. The different types of data input cards used for these packages within the scope of this thesis are detailed in section A.3.

4.6 Finite Element Method checks

A FE model has to be checked for any errors before the numerical analyses are solved. The below FEM checks have been carried out within the scope of this project to ensure that the FE model is acceptable for the solver and that the physical behavior of the structure is correctly represented numerically.

1. Mass of FEM and CAD model – The mass of the FEM should have the approximately same mass as the prediction by a geometric model. This ensures that all elements correctly represent the geometric structure they were meshed against. In this thesis project, the FEM mass calculations match the mass budget by geometry.

2. Error elements – The mesh quality has to be checked before exporting the model to the solver. The parameters such as aspect ratio, warp angle, skew, duplicate nodes, duplicate elements, Jacobian, distortion, minimum element length, etc. are checked against acceptable values. The mesh quality for this project has been checked for these criteria and in case of violations, mesh re-modification in local areas has been performed. The duplicate nodes and elements are merged so that additional degrees of freedom or additional stiffness are not added to the structure. The nodes and elements renumbering are performed carefully before each analysis.

3. Rigid body modes – A rigid body analysis involves a modal analysis without any constraints. An unconstrained structure has six free degrees of freedom (three linear translations along X, Y, Z, and three rotations about X, Y, Z). Hence, in an unconstrained condition, this analysis will result in the first six modes being at 0Hz typically a value < 0.0001Hz. If there are more than six free modal frequencies, that indicates that the

mesh is not correctly connected. The kick stage mesh structure is verified for the rigid body modes checks.

Chapter 5

Topology Optimization

The topology optimization studies form the first step of design space development. The development of topology optimization models and the results of the topology optimization is discussed in this chapter. The optimization was carried out for about six iterations, each with a step-wise increment of the design complexity. For the sake of brevity, the key results for the selected key three iterations are discussed in this report. Initially, the setup of the problem is discussed. This is followed by these aforementioned three models and their results and discussions.

5.1 Setting up the topology optimization problem

The topology optimization problem works on the density method, described in the previous section. This requires the entire design space to be given as input to the solver for finding the optimum distribution of the material so as to meet the objective within the constraints. The process then works by reassigning the material from the non-contributing regions to the critical regions of the mesh.

5.1.1 Solution Methodology – optimization input mesh, constraints, objective, and loads

The optimization process parameters including the constraints, loads, and objectives that are common to the input mesh are discussed.

- **Mass fraction constraint (upper bound)** – The design mass fraction denotes the total mass that the structure cannot exceed as a fraction of the initial design input mass. As per the discussion in an earlier chapter, the power law for the density method, a fraction of 0.3 is provided as the upper bound on the mass fraction.

- **Frequency constraint (lower bound)** – As mentioned earlier, the design requires a minimum of 15Hz as the first frequency requirement. Hence there is a lower bound constraint on the frequency response.
- **Design objective** – The design objective is the minimization of compliance with the structure. This is in context to maximize the stiffness of the structure, which in effect is to ensure that the stiffness of the designed structure for the propellant tank is maximized. Since the stiffness has to be accounted for in all three directions of excitation, the compliance is calculated as a sum of the compliance calculations for the QSL loads in X, Y, and Z directions.
- **Design space** – The entire design space within the geometric constraints is provided as input for optimization. The scope of this design volume changes in each of the analyses mentioned further. The mesh type is 3D CHEXA elements with an element size of 4cm. The PSOLID element properties help approximate the topology space correctly. Further, the optimizer will assign and modify the density of each 3D element and provide the solved result on convergence. Aerospace-grade aluminum 7075 is the material assigned for the mesh. The mesh checks are performed to ensure that there are no error elements.
- **Design Variables** – The design variable here is the DTPL design card for the entire 3D PSOLID design space mesh. The MINDIM parameter feature allowing for a minimum on the resolution of the topology optimization is enabled and set to three times the element size so as to get high-quality smooth result [1].
- **Load cases** – The QSL load cases are considered for the linear static load cases and compliance evaluation, with 9g for the longitudinal and 5g for the lateral accelerations. The modal load case for the first frequency calculation is provided as well. The first frequency is calculated as an eigenvalue problem as described in the earlier sections. The fixed boundary conditions representing the interface of the kick stage to the upper stage is kept constant in the analysis.
- **Responses** – The design evaluation and responses are recorded by the DRESP cards for variables such as mass, mass fraction, displacement, frequency, and weighted compliance. Some of these response cards are written back to the constraint card for the optimization loop to complete and meet the constraint requirements, while others are for monitoring the solution.

5.2 Topology optimization of a single tank

The topology optimization for a single tank provides the regions that are necessary for enhancing the load-carrying capacity of the kick stage structure.

5.2.1 Model Description

The first model includes the design space optimization for a single tank. The model input mesh to the sectional analysis for one propellant tank within the design space with a fixed

central core. The design impact of the assessment of the single tank is studied. The section view – shows the quarter of the cylindrical volume that can be occupied for the entire cylinder.

The propellant tank is modeled as a point mass with CONM2 properties. This connection of the propellant tank to the design space is done using twelve RBE3 elements representing the 12 attachment bolting points on the propellant tank.

The fixed boundary condition is assigned to all the nodes on the inner surface of the central hollow tube. This represents the central core that connects the upper stage to the payload and houses all the kick stage components. The key takeaway is to understand how the off-axis eccentric presence of a point mass affects the dynamic behavior of the kick stage when being designed and when the inner interface is fully provided with fixed boundary conditions. The input mesh view can be seen in Figure 5.1.

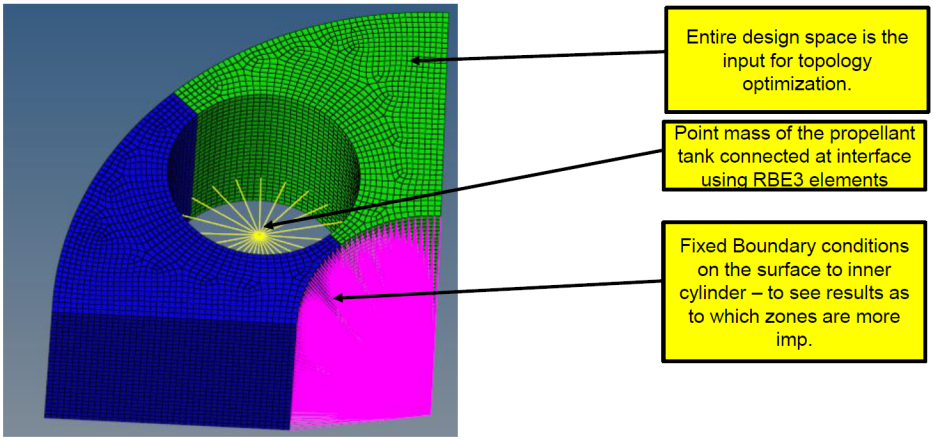

Figure 5.1: Topology study 1 – sectional model – input mesh

5.2.2 Analysis evaluation

The optimization result leads to a structure with reassigned mesh density. The difference in the result for the first iteration and the final iteration for this configuration can be seen in Figure 5.2. The change of the objective being minimized, the compliance, can be seen in Figure 5.3. For the same mass fraction of 0.3, the mass redistribution during the topology optimization occurs and results in the compliance objective being minimized from 50.34Nm to 1.50Nm. This results in a frequency improvement from 34.47Hz to 129.45Hz.

5.2.3 Result interpretation

The converged iteration that meets the boundary conditions is seen in Figure 5.4. The solution shows that there are regions in the mesh where the element density is zero, indicating that those regions have no contribution to meeting the objective or keeping the solution within constraints. There are gaps along the fixed interface as well, indicating that despite the entire surface being with a fixed boundary condition, the regions which do not contribute to the stiffness of the propellant tanks can be safely ignored. The connection points of the propellant tanks to the surrounding structure are uniformly present with high material density, indicating

Figure 5.2: Topology study 1 – sectional model – comparison of first and converged iteration

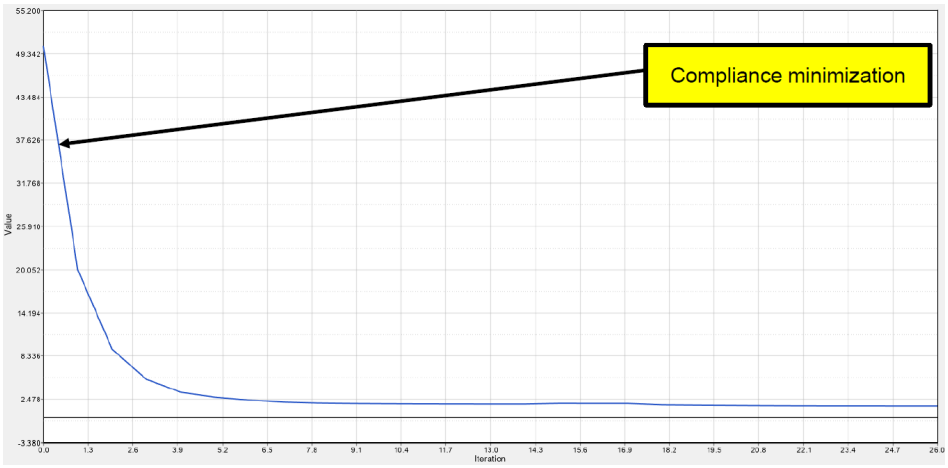

Figure 5.3: Topology study 1 – sectional model – minimization of compliance objective

the criticality of this region for the solution. The light-shaded transparent view indicates the total design space which was discussed in the earlier section of the model description. A significant portion of the outer material region is shown to be insignificant for the optimum solution. The support structure to the far side of the cylinder is seen to rise from the top interface and follow a double-curved path to maximize the stiffness.

However, to fully account for the total static and dynamic behavior of the structure with all four cylinders, the next model is developed.

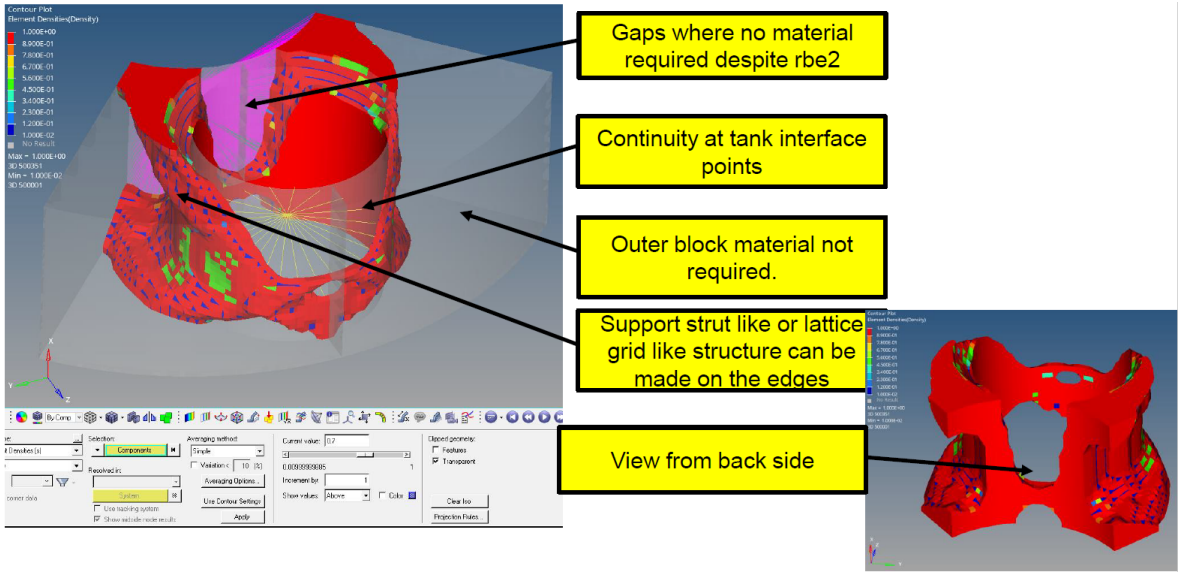

Figure 5.4: Topology study 1 – sectional model – converged solution view

5.3 Topology optimization for the model with four tanks

The second model includes the design space optimization for the entire design space with all four propellant tanks. The model input mesh consists of four propellant tanks within the total design space with a fixed boundary condition on the central core.

5.3.1 Model Description

The propellant tank and the connection points to the surrounding design space are modeled as mentioned in the previous model. The fixed boundary condition is assigned to all the nodes on the inner surface of the central hollow tube. The key takeaway is to understand how the presence of four tanks affects the dynamic behavior of the kick stage when being designed and when the inner interface is fully provided with fixed boundary conditions. The input mesh view can be seen in Figure 5.5.

In this model, all 4 sets of propellant tanks are modeled. This contains two sets of propellants and two sets of oxidizers. The masses for the oxidizer tank and the propellant tanks are taken from the corresponding user manual for 97% filled capacity with the corresponding density. The masses then correspondingly are arranged diagonally following the fuel-burning requirements. The oxidizer tank has a mass of 1252kg and the propellant tank has a mass of 777kg.The propellant tank CONM2 nodes to design space connections using RBE3 are similar to the previous condition. The central core is the fixed boundary in the design setup. This is to see the impact of neighboring cylinders on the dynamic performance of each cylinder.

5.3.2 Analysis evaluation

The optimization result leads to a structure with reassigned mesh density. The difference in the result for the first iteration and the final iteration for this configuration can be seen in

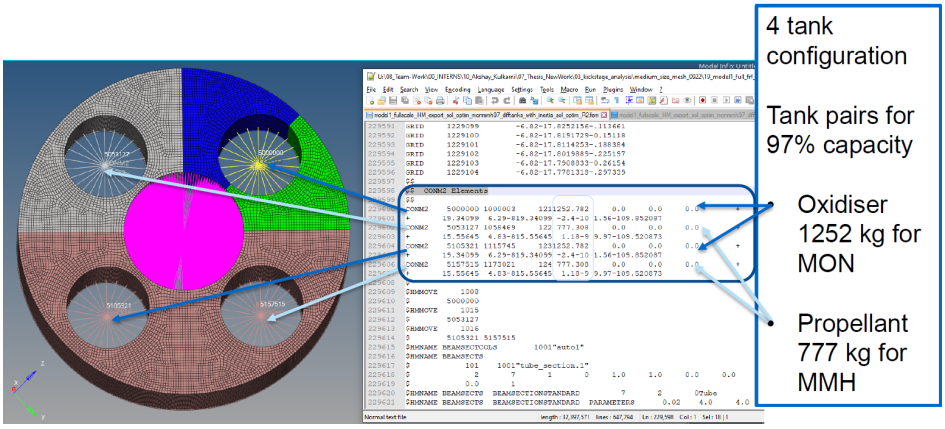

Figure 5.5: Topology study 2 – all tanks model – input mesh

Figure 5.6 and the change of the objective being minimized, the compliance, can be seen in Figure 5.7. For the same mass fraction of 0.3, the mass redistribution during the topology optimization occurs and results in the compliance objective being minimized from 305.30Nm to 14.24Nm. This results in a frequency improvement from 50.35Hz to 178.63Hz.

```
Objective Function (Minimize WCOMP) =  3.05308E+02
Maximum Constraint Violation %      =  0.69759E-11
Design Volume Fraction              =  2.11975E-01   Mass     =  1.09044E+04
Discreteness Index                  =          0.00

Density      %
-------------
0.0-0.1    0.0
0.1-0.2    0.0
0.2-0.3  100.0
0.3-0.4    0.0
0.4-0.5    0.0
0.5-0.6    0.0
0.6-0.7    0.0
0.7-0.8    0.0
0.8-0.9    0.0
0.9-1.0    0.0

 Subcase  Weight      Compliance     Epsilon                 Weight*Comp.
      11  1.000E+00  2.224182E+02 -5.530023E-12              2.224182E+02
      12  1.000E+00  4.241323E+01 -3.395804E-12              4.241323E+01
      13  1.000E+00  4.047689E+01 -3.311089E-12              4.047689E+01
                                                            -----------
Sum of Weight*Compliance                                    3.053083E+02

Note : Epsilon = Residual Strain Energy Ratio.

                                                 Generalized   Generalized
 Subcase  Mode   Frequency    Eigenvalue          Stiffness        Mass
      14     1  5.035110E+01  1.000870E+05  1.000870E+05  1.000000E+00
      14     2  5.857378E+01  1.354460E+05  1.354460E+05  1.000000E+00
      14     3  5.863775E+01  1.357420E+05  1.357420E+05  1.000000E+00
```

```
ITERATION  26
  the 2nd satisfied convergence ratio =  3.9616E-03

Objective Function (Minimize WCOMP) =  1.42410E+01   % change =       -0.39
Maximum Constraint Violation %      =  0.00000E+00
Design Volume Fraction              =  2.11975E-01   Mass     =  1.09044E+04
Discreteness Index                  =          0.94

Density      %
-------------
0.0-0.1   79.9
0.1-0.2    0.1
0.2-0.3    0.1
0.3-0.4    0.1
0.4-0.5    0.1
0.5-0.6    0.4
0.6-0.7    0.0
0.7-0.8    0.0
0.8-0.9    0.0
0.9-1.0   19.2

 Subcase  Weight      Compliance     Epsilon                 Weight*Comp.
      11  1.000E+00  7.703345E+00 -1.211549E-12              7.703345E+00
      12  1.000E+00  3.646412E+00 -2.931924E-12              3.646412E+00
      13  1.000E+00  2.891213E+00 -2.575866E-12              2.891213E+00
                                                            -----------
Sum of Weight*Compliance                                    1.424097E+01

Note : Epsilon = Residual Strain Energy Ratio.

                                                 Generalized   Generalized
 Subcase  Mode   Frequency    Eigenvalue          Stiffness        Mass
      14     1  1.786374E+02  1.259808E+06  1.259808E+06  1.000000E+00
      14     2  1.864806E+02  1.372862E+06  1.372862E+06  1.000000E+00
      14     3  1.870473E+02  1.381220E+06  1.381220E+06  1.000000E+00
      14     4  1.966434E+02  1.526575E+06  1.526575E+06  1.000000E+00
```

Figure 5.6: Topology study 2 – all tanks model – comparison of first and converged iteration

5.3.3 Result interpretation

The converged iteration that meets the boundary conditions is seen in Figure 5.8. Similar to the first model, the solution shows that there are regions in the mesh where the element density is zero, indicating that those regions have no contribution to meeting the objective or keeping the solution within constraints. There are gaps along the fixed interface as well, indicating that despite the entire surface being with a fixed boundary condition, the regions which do not contribute to the stiffness of the propellant tanks can be safely ignored. The connection points of the propellant tanks to the surrounding structure are uniformly present with high material density, indicating the criticality of this region for the solution. A more

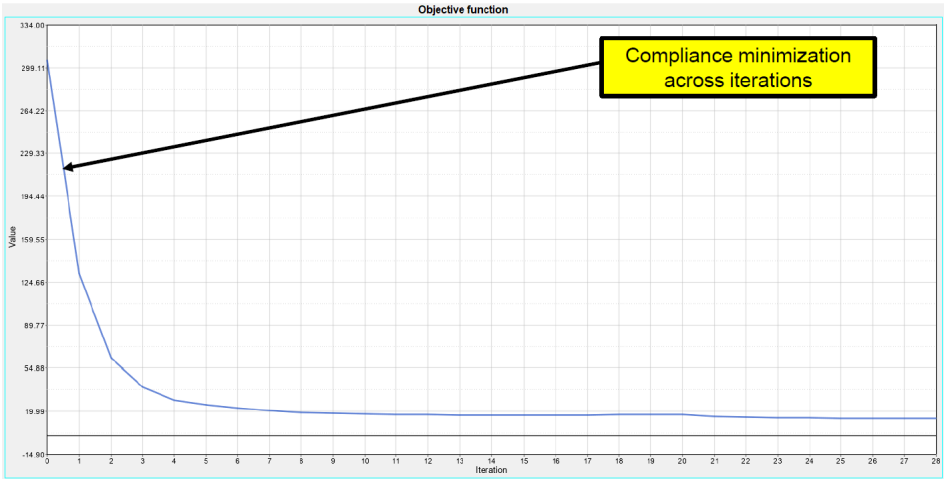

Figure 5.7: Topology study 2 – all tanks model – minimization of compliance objective

continuous support structure from the top interface to the far side of the cylinder is seen. This indicates the impact of neighboring propellant tanks and the corresponding support structure, leading to a more organic structure as a result.

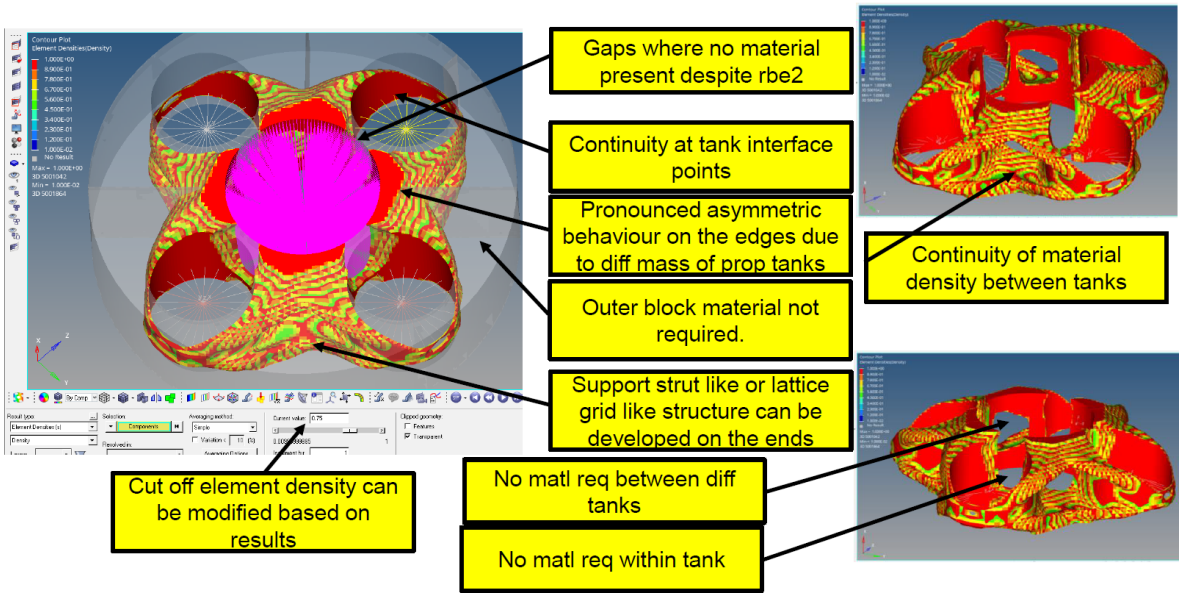

Figure 5.8: Topology study 2 – all tanks model – converged solution view

In the final step, to fully account for the total static and dynamic behavior of the structure with all four cylinders and the payload on the kick stage, the next model is developed.

5.4 Topology optimization for full four tanks with modeled central core and satellite point mass

The third model includes the design space optimization for the entire design space with all four propellant tanks and the payload spacecraft on top of the kick stage.

5.4.1 Model Description

All four sets of propellant tanks along with the spacecraft are modeled. The central core between the spacecraft interface and the Upper Stage interface is included in the design space. The bottom interface of the clamp band to the Upper Stage is a fixed boundary condition. The point mass of 4.2t for the spacecraft is assumed at the height of 2.5m from the top interface of the kick stage, indicating this load acting at the COG of the payload spacecraft. The connection between the spacecraft node and the kick stage interface nodes is given by RBE3 elements. This represents the complete design space and is set to provide a more realistic result of how the dynamics and static are impacted by the combination of the payload spacecraft and the propellant tanks. The input mesh view can be seen in Figure 5.9.

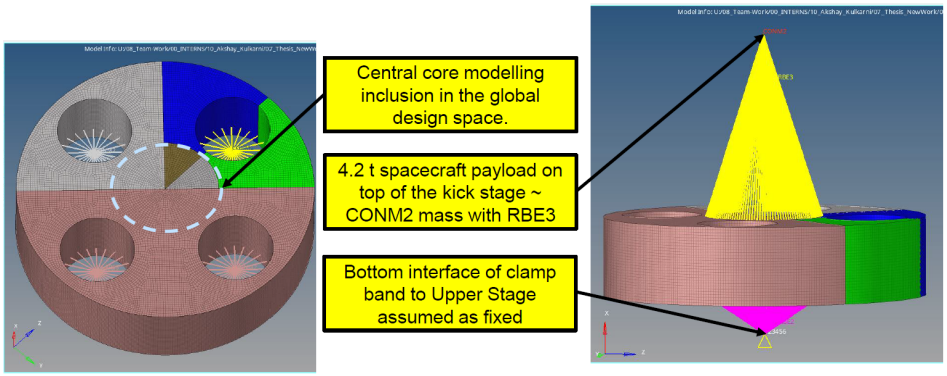

Figure 5.9: Topology study 3 – all tanks model with payload – input mesh

5.4.2 Analysis evaluation

The optimization result leads to a structure with reassigned mesh density. The difference in the result for the first iteration and the final iteration for this configuration can be seen in Figure 5.10 and the change of the objective being minimized, the compliance, can be seen in Figure 5.11. For the same mass fraction of 0.3, the mass redistribution during the topology optimization occurs and results in the compliance objective being minimized from 3400.25Nm to 92.14Nm. This results in a frequency improvement from 12.22Hz to 84.36Hz.

5.4.3 Result interpretation

The converged iteration is seen in Figure 5.12. The solution is different from the previous two model solutions. The features of organic design results between the tanks are more

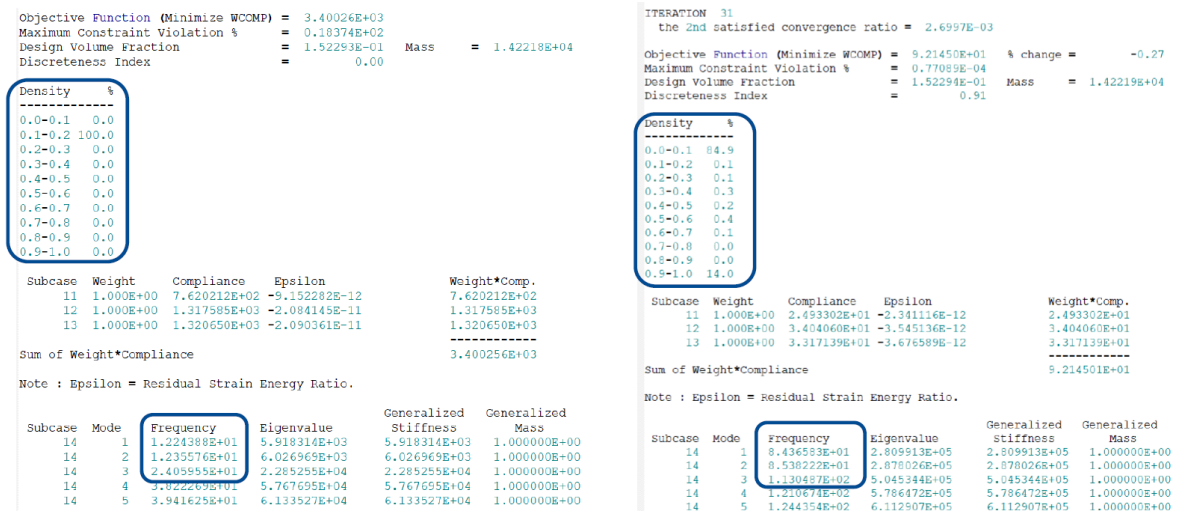

```
Objective Function (Minimize WCOMP) =  3.40026E+03
Maximum Constraint Violation %      =  0.18374E+02
Design Volume Fraction              =  1.52293E-01   Mass     =  1.42218E+04
Discreteness Index                  =         0.00

Density     %
------------
0.0-0.1    0.0
0.1-0.2  100.0
0.2-0.3    0.0
0.3-0.4    0.0
0.4-0.5    0.0
0.5-0.6    0.0
0.6-0.7    0.0
0.7-0.8    0.0
0.8-0.9    0.0
0.9-1.0    0.0

 Subcase  Weight     Compliance    Epsilon                Weight*Comp.
      11  1.000E+00  7.620212E+02 -9.152282E-12          7.620212E+02
      12  1.000E+00  1.317585E+03 -2.084145E-11          1.317585E+03
      13  1.000E+00  1.320650E+03 -2.090361E-11          1.320650E+03
                                                        ------------
Sum of Weight*Compliance                                3.400256E+03

Note : Epsilon = Residual Strain Energy Ratio.

                                                 Generalized   Generalized
 Subcase  Mode   Frequency      Eigenvalue        Stiffness       Mass
      14     1  1.224388E+01  5.918314E+03  5.918314E+03  1.000000E+00
      14     2  1.235576E+01  6.026969E+03  6.026969E+03  1.000000E+00
      14     3  2.405955E+01  2.285255E+04  2.285255E+04  1.000000E+00
      14     4  3.822269E+01  5.767695E+04  5.767695E+04  1.000000E+00
      14     5  3.941625E+01  6.133527E+04  6.133527E+04  1.000000E+00
```

```
ITERATION  31
  the 2nd satisfied convergence ratio =  2.6997E-03

Objective Function (Minimize WCOMP) =  9.21450E+01   % change =       -0.27
Maximum Constraint Violation %      =  0.77089E-04
Design Volume Fraction              =  1.52294E-01   Mass     =  1.42219E+04
Discreteness Index                  =         0.91

Density     %
------------
0.0-0.1   84.9
0.1-0.2    0.1
0.2-0.3    0.1
0.3-0.4    0.3
0.4-0.5    0.2
0.5-0.6    0.4
0.6-0.7    0.1
0.7-0.8    0.0
0.8-0.9    0.0
0.9-1.0   14.0

 Subcase  Weight     Compliance    Epsilon                Weight*Comp.
      11  1.000E+00  2.493302E+01 -2.341116E-12          2.493302E+01
      12  1.000E+00  3.404060E+01 -3.545136E-12          3.404060E+01
      13  1.000E+00  3.317139E+01 -3.676589E-12          3.317139E+01
                                                        ------------
Sum of Weight*Compliance                                9.214501E+01

Note : Epsilon = Residual Strain Energy Ratio.

                                                 Generalized   Generalized
 Subcase  Mode   Frequency      Eigenvalue        Stiffness       Mass
      14     1  8.436583E+01  2.809913E+05  2.809913E+05  1.000000E+00
      14     2  8.538222E+01  2.878026E+05  2.878026E+05  1.000000E+00
      14     3  1.130487E+02  5.045344E+05  5.045344E+05  1.000000E+00
      14     4  1.210674E+02  5.786472E+05  5.786472E+05  1.000000E+00
      14     5  1.244354E+02  6.112907E+05  6.112907E+05  1.000000E+00
```

Figure 5.10: Topology study 3 – all tanks model with payload – comparison of first and converged iteration

pronounced. The central core material is completely eliminated with a low density indicating a cylindrical core is more suitable for the design. The presence of four propellant tanks creates additional support structures on the sides. The thickness of the support structures is proportional to the tank masses, so the heavier oxidizer tanks lead to a thicker structure, while the comparatively lighter propellant fuel tanks lead to a slightly thinner structure. The joining points of these support structures are also different, creating asymmetry for the tanks. In addition, there is the presence of a lattice strut structure between the tanks on the far side, although the thickness is comparatively thinner than the rest of the structure.

5.4.4 Result export

This result represents the final topologically optimized structure. The resultant mesh is then exported with a full mesh density of 1 to result in a new solution mesh as shown in Figure 5.13. This an exported solution mesh, and as a standalone analysis provides the nearly same result of QSL stresses and first modal frequency as the final iteration of the optimization. The mass split up of the final result is discussed here. Out of the total 14.83t solution result mass, subtracting the mass of propellant tanks and the satellite point mass leads to a structural solution of 6.57t smeared out as isotropic material with the density of aluminum. As the result shows, the structure topology is clear, however, the mass is way larger than the mass budget.

In the next steps, it is desired to reduce the mass while maintaining the frequency constraints and considering the dynamic performance of the model. This is detailed in upcoming chapters.

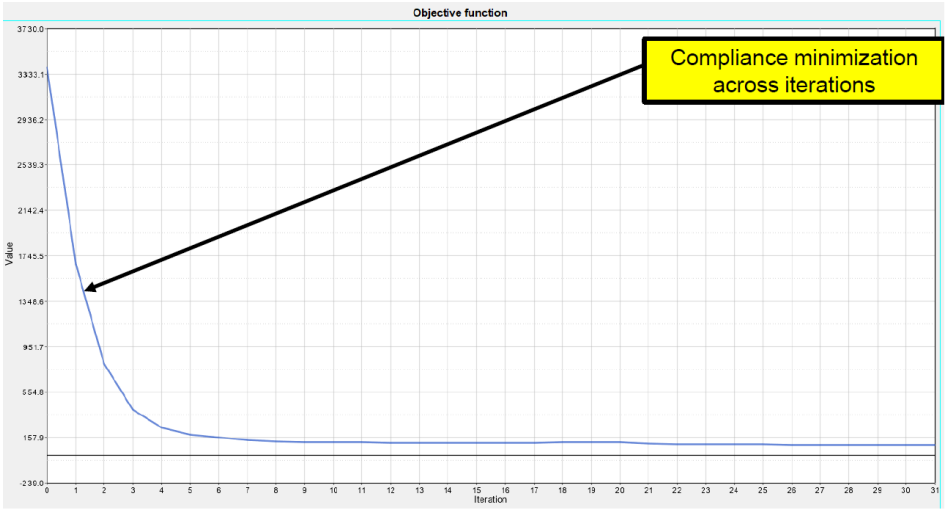

Figure 5.11: Topology study 3 – all tanks model with payload – minimization of compliance objective

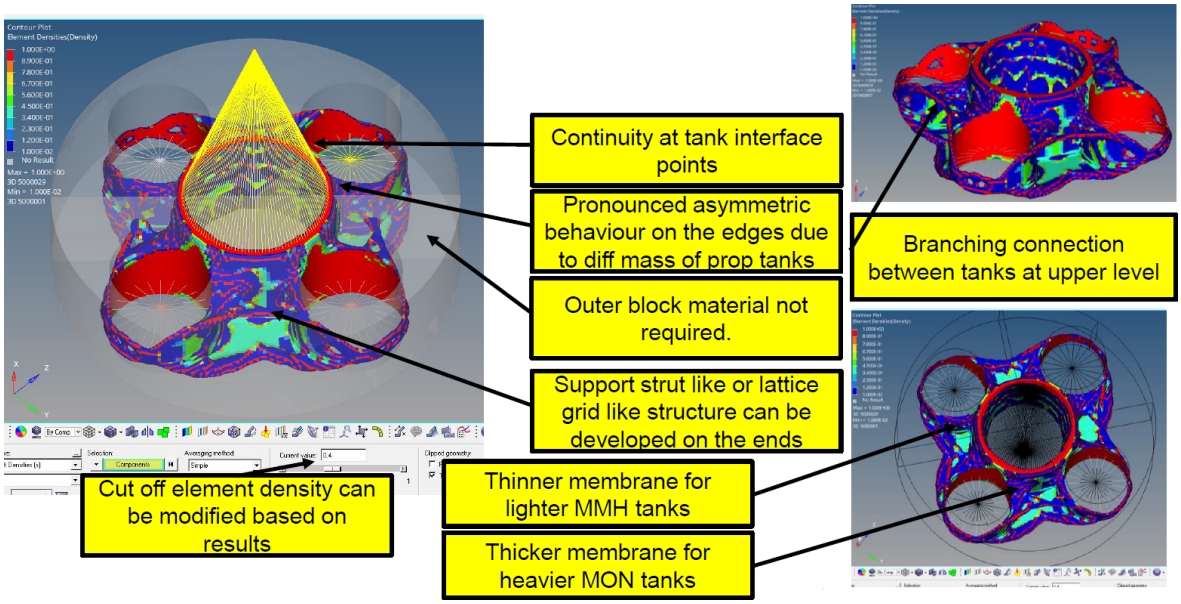

Figure 5.12: Topology study 3 – all tanks model with payload – converged solution view

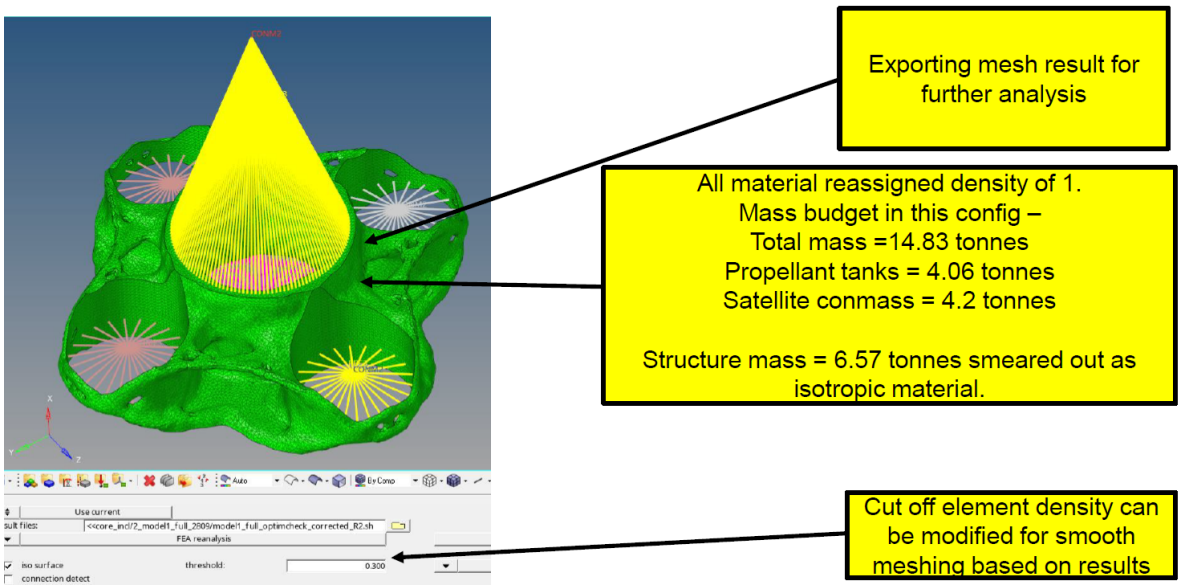

Figure 5.13: Export of result file for Model 3 to a new mesh

5.5 Discussion

The final mesh optimized result for all three cases is seen in Figure 5.14. The distinction in the resulting changes at each step can be clearly seen. The results show that the topology optimization method provides a good understanding of the critical areas in the design space. In addition, the optimization takes into account the loading conditions and the total design space. The effect of two sets of cylinders i.e. propellant and oxidizer leads to two different load paths that can meet this objective. The final design iteration of the full model though, shows that the heavier spacecraft point mass is the higher driving factor for the design, so a larger mass is present along the central cylinder. It can also be seen that there is no diagonal load path crossing the cylinder in between, even though it was a part of the design space to be optimized. However, there is the presence of membranes and continuous structures on the outer platform connecting adjacent propellant tanks. This indicates that the neighboring tanks have a greater effect in adding global stiffness to the structure. These features are non-intuitive. For simple loading conditions with simple geometry, a free-body diagram can help to find the critical loading areas and accordingly assign material in those regions. However, when complex load paths and dynamic load cases are involved for a large structure, a topology optimization study as shown can provide newer insight into the structure design. It also noted after considering the design trinity principles, that such a design cannot be directly manufactured. This is attributed primarily due to the mass and size of the structure. A splitting of such an organic structure would be required, and in addition, the mass should be brought down to acceptable levels. In the next chapter, this final design is further refined to two sizing optimization studies and the results are reported.

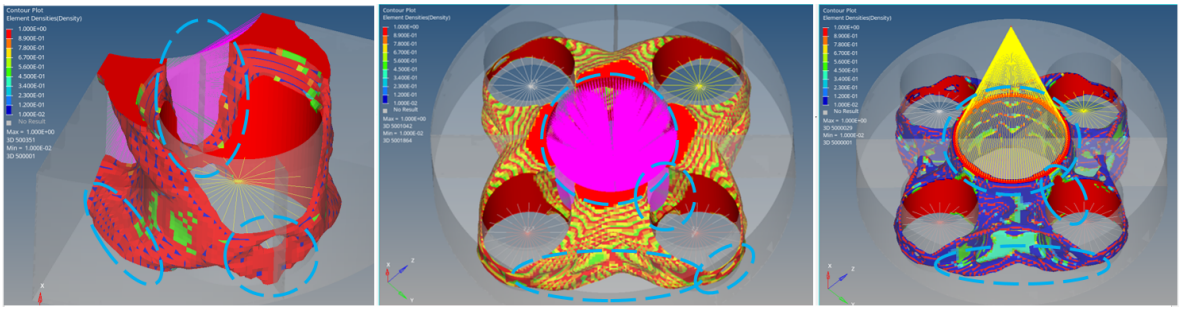

Figure 5.14: Comparison of the final result files for the topology optimization studies

Chapter 6

Sizing Optimization 1 – strut design

The results of the topology optimization studies were then modified to complete the shape and sizing optimization studies. This analysis has bridged the gap between the high mass high stiffness results of topology optimization to a manageable result with geometry considerations.

6.1 Converting topology optimization result mesh to a sizing optimization mesh

The methodology for shape and sizing optimization involved extracting the shape of the design of the topology optimization result and then subjecting it to sizing optimization steps. The analysis involves reducing the mass of this topology results while meeting the minimum 15Hz requirement and checking the dynamic response at the propellant tanks for the acceleration input. The more organic results of the topology optimization are converted into a combination of shell and bar elements for the sizing optimization studies.

The result of the topology optimization is an organic continuous structure. This makes it difficult for shape identification and sizing optimization studies using FEM. In addition, the design trinity principles of manufacturing and assembly also step into the design aspect. It is not possible to manufacture such a large continuous structure. So a set of manageable structural elements are needed that will approximate a similar if not the same structure that can be used for proper manufacturing and assembly. Hence, the next step is to replicate the shape of the topology result into a discrete but equivalent combination of bar and shell elements. The geometry parameters such as thickness and shape can then be modified iteratively in the sizing optimization process by being assigned as the design variables.

The meshing process done on the topology optimized mesh to a discrete sizing optimized mesh is as shown in Figure 6.1. There are three distinct regions mapped out. The central core is modified to a cylindrical shell mesh. The smooth surface around the propellant tanks is also meshed to be a double-curved cylindrical shell mesh. A smooth top edge curve ensures the continuity between the geometry of the topology mesh and the shell mesh. Finally, the

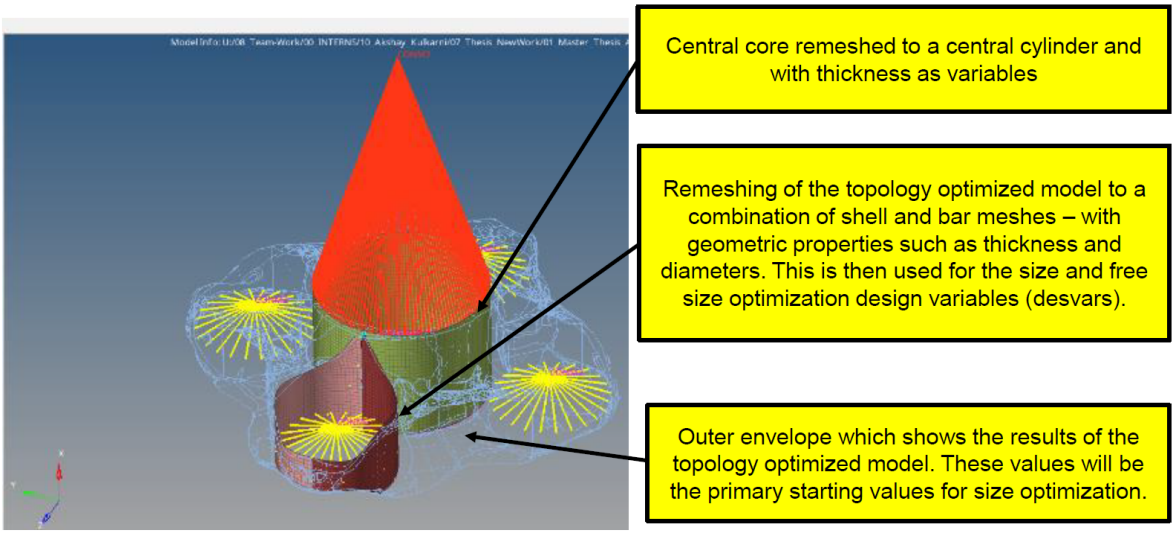

Figure 6.1: Model design methodology from topology optimization result to sizing optimization

outer platform connecting the surfaces of the propellant tanks meshes as a flat shell mesh. The mesh sizes and node placement is done such that the continuity of the propellant tank connecting nodes and the satellite nodes is maintained. Finally, additional support structures are modeled using a combination of bar and shell elements and connected with suitable rigid elements to end nodes.

The proposed mesh types and the final output to be used for the next type of optimization studies are shown in Figure 6.3. There are two types of sizing optimization methods offered by Optistruct. These are size and free-sizing optimization methods. The sizing optimization is useful for the bar elements and shell elements where the total size of a given mesh can be modified iteratively to meet the objective. The free-sizing optimization offers additional advantages in which each element of the shell mesh can be varied in thickness. This is particularly useful for sizing each element on the shell mesh and also indicates the more critical regions for the optimization process [1]. This indicates that this optimization loop is relevant for thin skin continuous shell-based structures where different thicknesses could be manufactured more easily in comparison to honeycomb structures, where the entire structure is manufactured using fixed thicknesses for core and face skin.

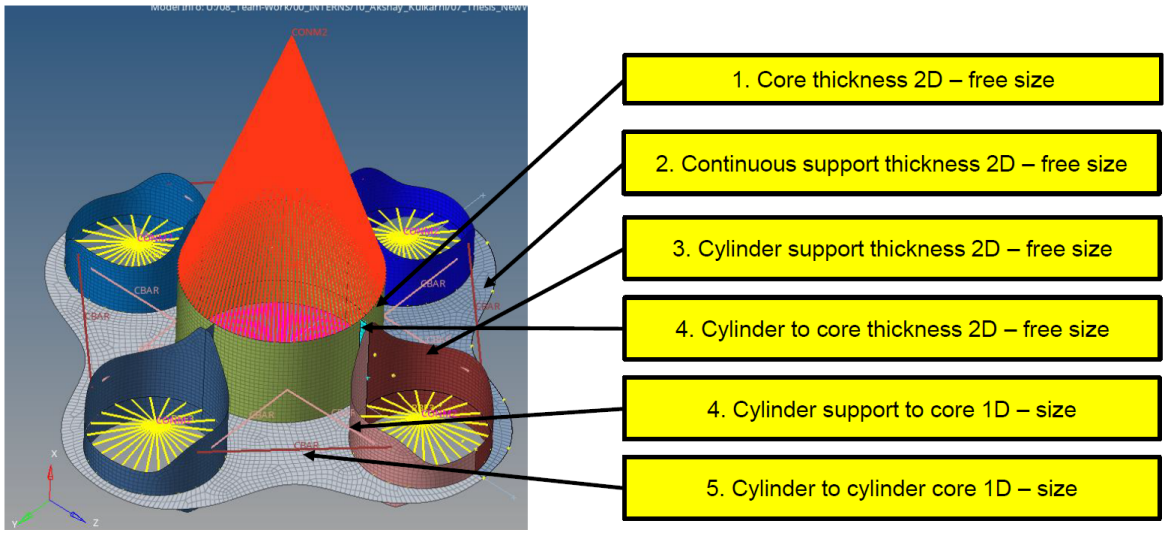

Figure 6.2: Meshing and optimization card details for the sizing optimization studies

6.2 Solution methodology – Optimization input mesh, constraints, objective, and loads

The solution methodology and the optimization process parameters including the constraints, loads, and objectives of the sizing optimization analysis is described.

- **Stress constraint (upper bound)** – The maximum stress is governed by the yield stress of the material and a factor of safety. The design space elements are expected to not exceed the von mises stress higher than this specification.
- **Frequency constraint (lower bound)** – The design requires a minimum of 15Hz as the first frequency requirement. Hence there is a lower bound constraint on the frequency response.
- **Frequency response constraint (upper bound)** – The frequency response analysis is done for the entire model for each iteration. The resultant magnitude of the acceleration has an upper bound of $88.29\,\mathrm{m/s^2}$ which is a convergent criteria for 9g. This is the qualification level for which the propellant tanks are qualified. The constraint is applied on the propellant tank point masses, so that the solution acceleration is below the maximum upper bound.
- **Design objective** – The design objective is the minimization of the mass of the structure.
- **Design space** – The entire design space within the geometric constraints is provided as input for optimization. The scope of this design volume changes in each of the analyses mentioned further. The model meshed using SHELL and BAR elements.
- **Design Variables** – The design variables are a range of lower-end to upper-end values on the design responses for the inner and outer diameter of the strut and the thicknesses

of the shell elements. The element size for the shell elements is 4cm. Each of the design variables is then assigned to the corresponding design property.

- **Load cases** – The QSL load cases are considered for the linear static load cases and compliance evaluation, with 9g for the longitudinal and 5g for the lateral accelerations. The modal load case for the first frequency calculation is provided as well. The first frequency is calculated as an eigenvalue problem as described in the earlier sections. The fixed boundary conditions are representing the interface of the kick stage to the upper stage. The dynamic frequency response solution is also requested, with the sine input specific excitation in all three directions. The damping factor for the dynamic frequency response function is 0.3. The buckling load case is assigned to the solution as well, to calculate the buckling modes.

- **Responses** – The design evaluation and responses are recorded by the DRESP cards for variables such as mass, mass fraction, displacement, frequency, buckling value, dynamic frequency acceleration response, and weighted compliance. Some of these response cards are written back to the constraint card for the optimization loop to complete and meet the constraint requirements, while others are for monitoring the solution.

6.3 Developing two solution models

The next step involves developing two models corresponding to two shapes from this result as seen in Figure 6.3. The central core and the flat platform as 2D shell meshes and are the same in both models. Model 1 corresponds to a design in which the central core to propellant tanks is stiffened by strut based 1D bar elements. Model 2 corresponds to a design in which the design is stiffened by 2D shell mesh representing pairs of shear webs. The angle of inclination of both bar and shear webs is determined by the topology optimization result mesh.

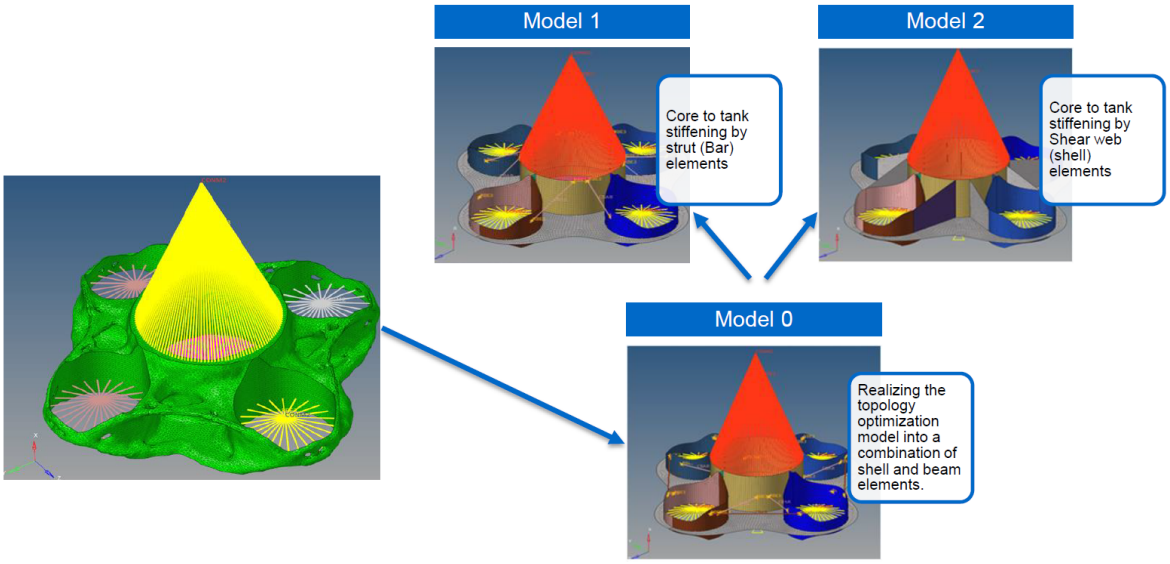

Figure 6.3: Model design methodology for shape and sizing optimization

6.4 Model 1 – description and optimization solutions

In this model, the connection from the central core to the propellant tanks is modeled by a strut which is in turn modeled by 1D CBAR elements. The joining points are as seen from the model, with one end towards the top end of the shell element, and the bottom end on the propellant tank stiffeners. There are REB3 elements at the ends to distribute the load over a set of nodes. The model is shown in Figure 6.4.

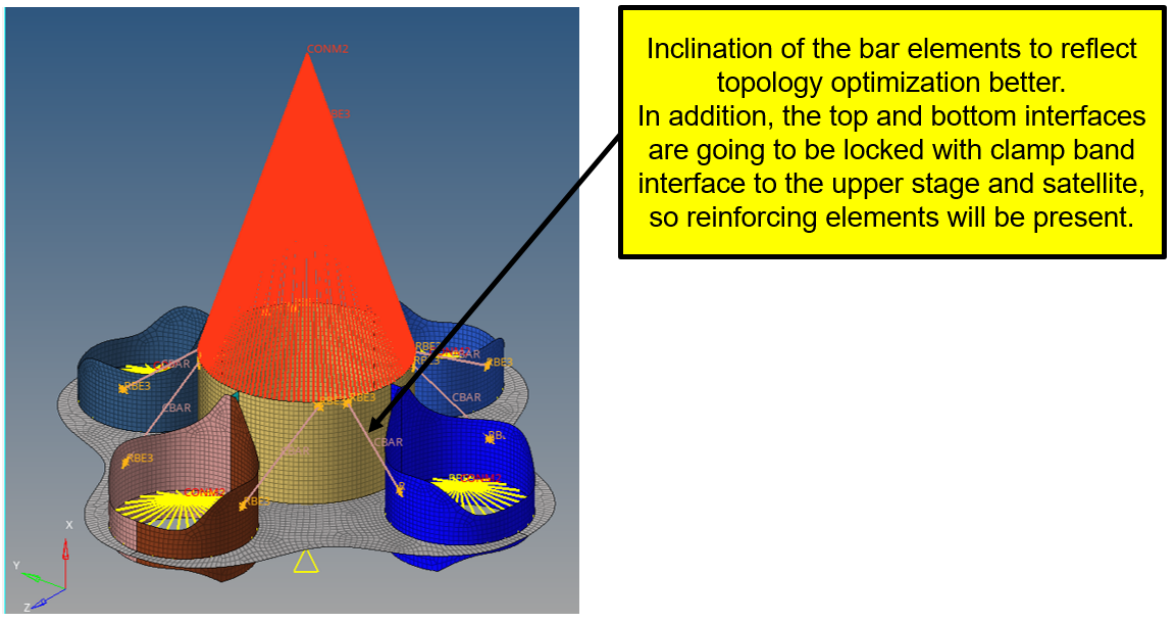

Figure 6.4: Description of Model 1 – input mesh for sizing optimization study

6.5 Model 1 solution 1 – analysis excluding the frequency response function constraint

The first analysis does not have the frequency response calculations defined within the sizing optimization loop. This is to understand the driving conditions for the analysis convergence when the dynamic frequency response is not an optimization constraint. This also provides feedback on the solution when considering only the primary constraints of stress levels and frequency requirements.

6.5.1 Analysis evaluation

The optimization result leads to a structure with modified design parameters. The difference in the result for the first iteration and the final iteration for this configuration can be seen in Figure 6.5. The graph of the change of mass of the structure and the first modal frequency can be seen in Figure 6.6. For the sizing optimization result, the objective mass is minimized from a total of 6009.5kg to 401kg. This results in a frequency drop from 65.8Hz to 14.9Hz,

which meets the requirement. Additionally, the thickness plot of the shell mesh is seen in Figure 6.7 and the change of the strut diameter is seen in Figure 6.8. The modal analysis results includes the normalized displacement of the first three modes as seen in Figure 6.9 and the modal effective mass plot between the first and the final iteration is Figure 6.10. The difference of the mode shapes and the corresponding effective mass change can be seen here. The dynamic frequency response results are given for all nodes by Figure 6.11 for X direction excitation, Figure 6.12 for Y direction excitation, Figure 6.13 for Z direction excitation. For the node for reference node MON tank, the maximum peak acceleration is 14.9g at 90Hz which is exceeding the qualification value of 9g. The quasi-static stresses are seen in Figure 6.14. It can be seen here that all the stresses are within the stress constraint limits and found safe. The buckling load for the structure is 3.899E6N and the mode shape is seen in Figure 6.15.

It can be seen that in the case of a mass minimization objective, the solution is driven by the frequency requirements constraint. However, the peak responses in directions exceed the propellant tank qualification value. Hence, the next step is to include these responses within the optimization framework.

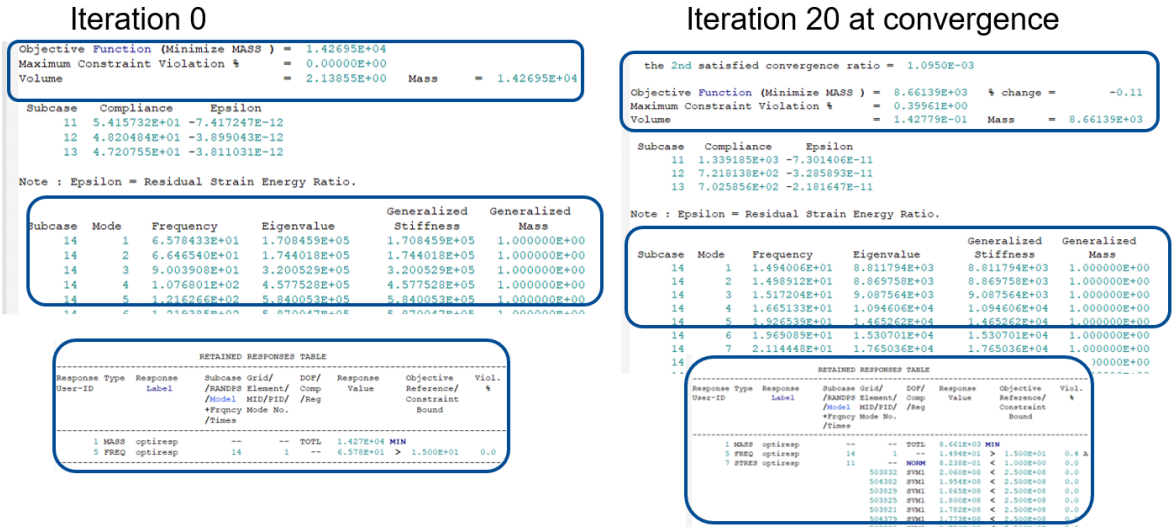

Figure 6.5: Model 1 solution 1 – iteration data comparison

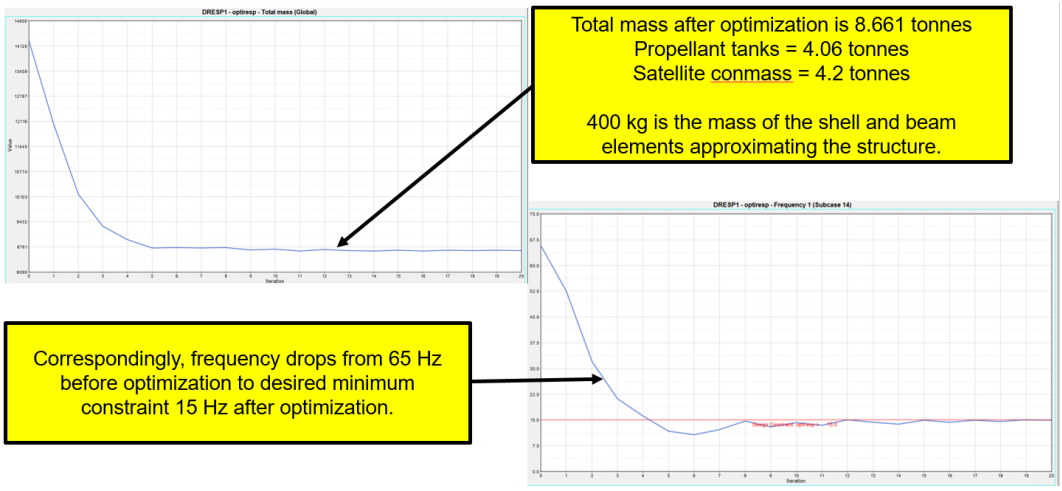

Figure 6.6: Model 1 solution 1 – mass and frequency data comparison

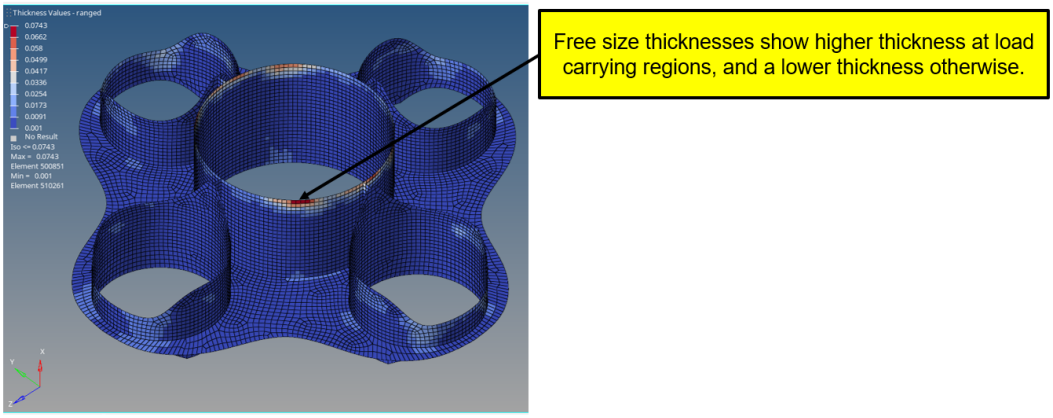

Figure 6.7: Model 1 solution 1 – mass distribution for the free size shell optimization

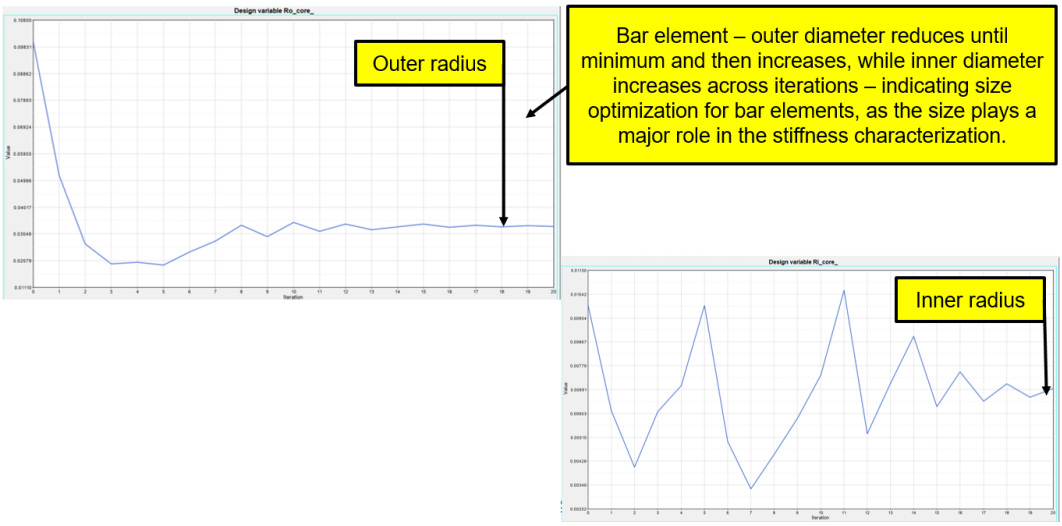

Figure 6.8: Model 1 solution 1 – strut diameter across iterations

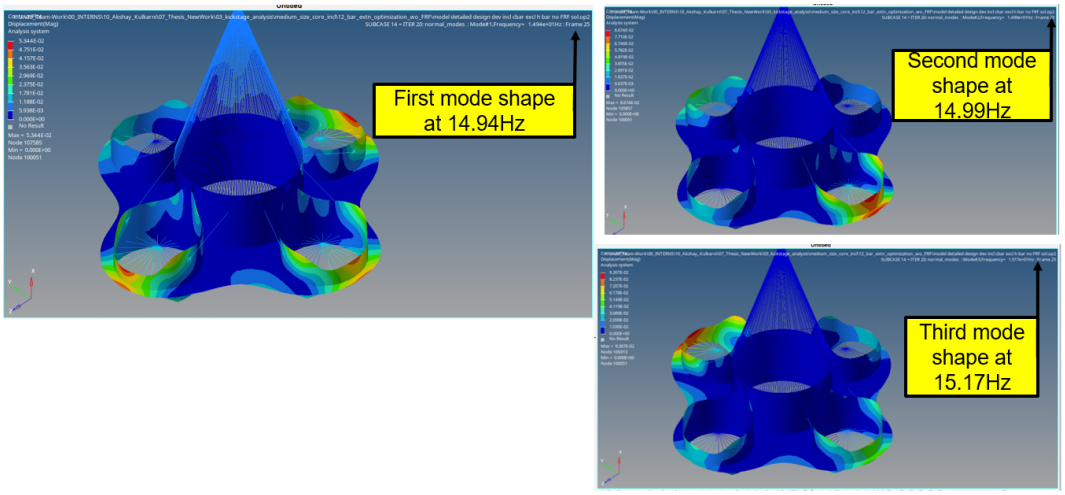

Figure 6.9: Model 1 solution 1 – modal analysis results for the converged iteration

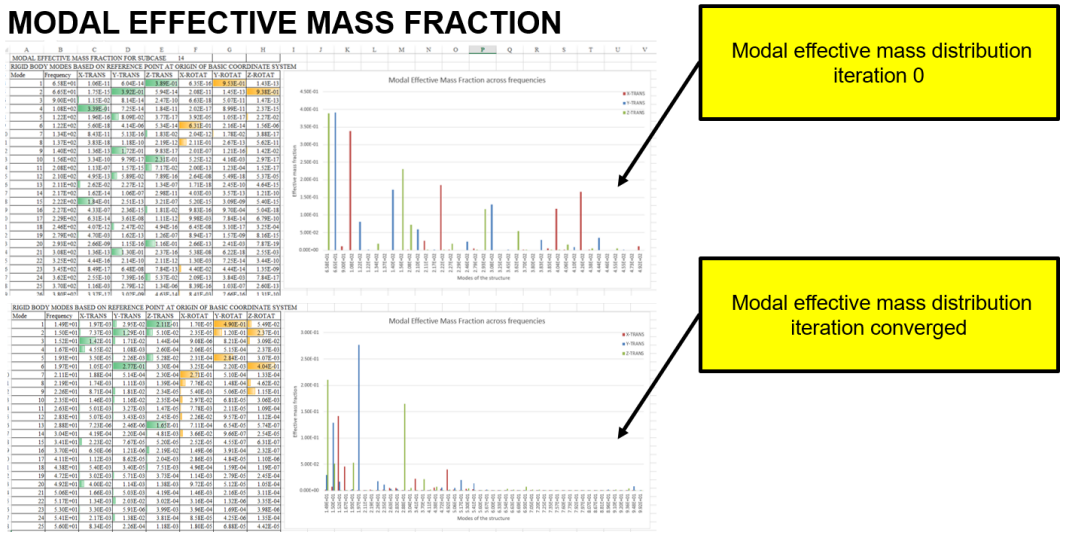

Figure 6.10: Model 1 solution 1 – modal effective mass fraction for the starting and converged iteration

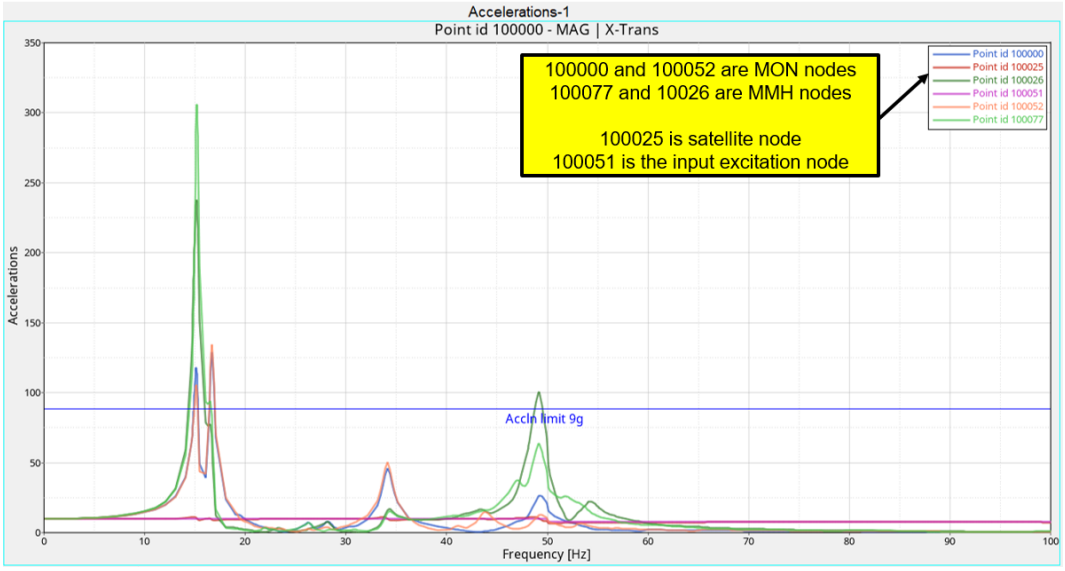

Figure 6.11: Model 1 solution 1 – dynamic analysis results for the converged iteration – X excitation

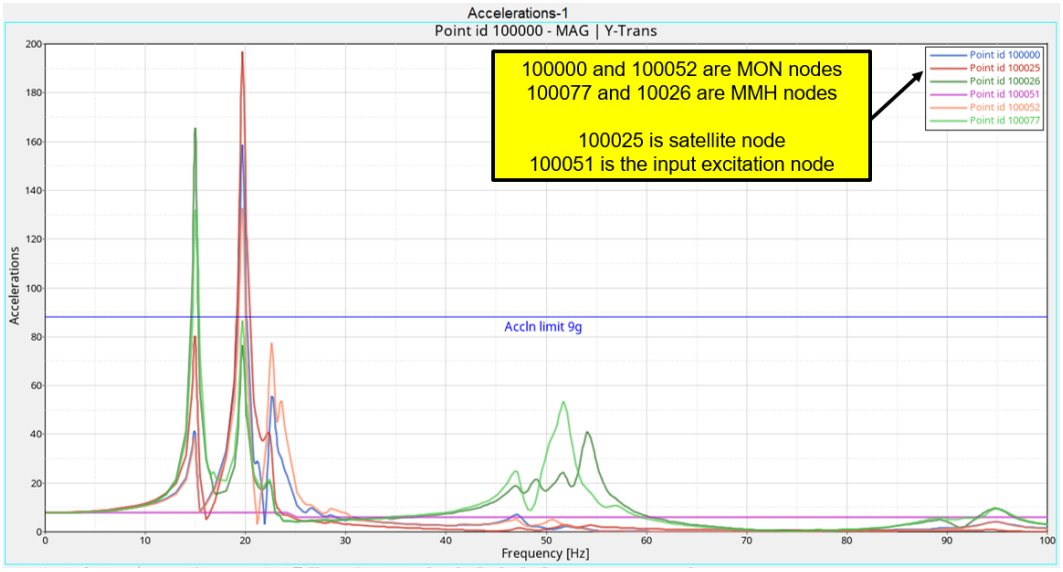

Figure 6.12: Model 1 solution 1 – dynamic analysis results for the converged iteration – Y excitation

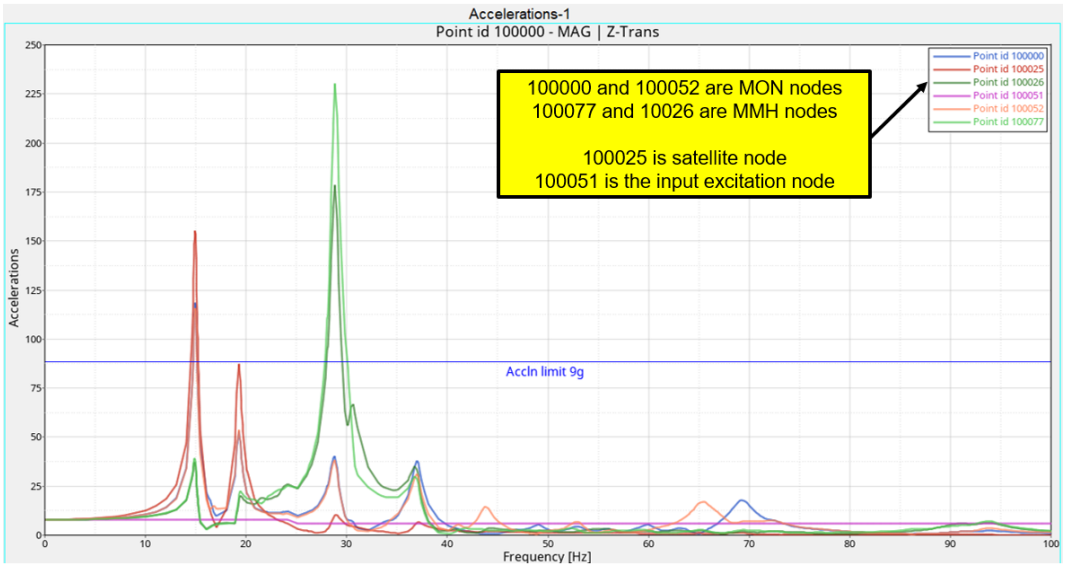

Figure 6.13: Model 1 solution 1 – dynamic analysis results for the converged iteration – Z excitation

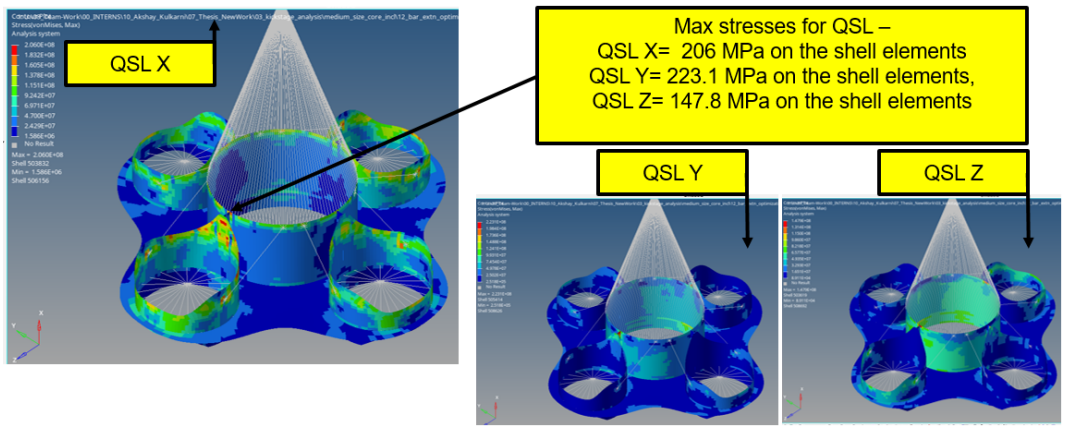

Figure 6.14: Model 1 solution 1 – quasi-static stresses results

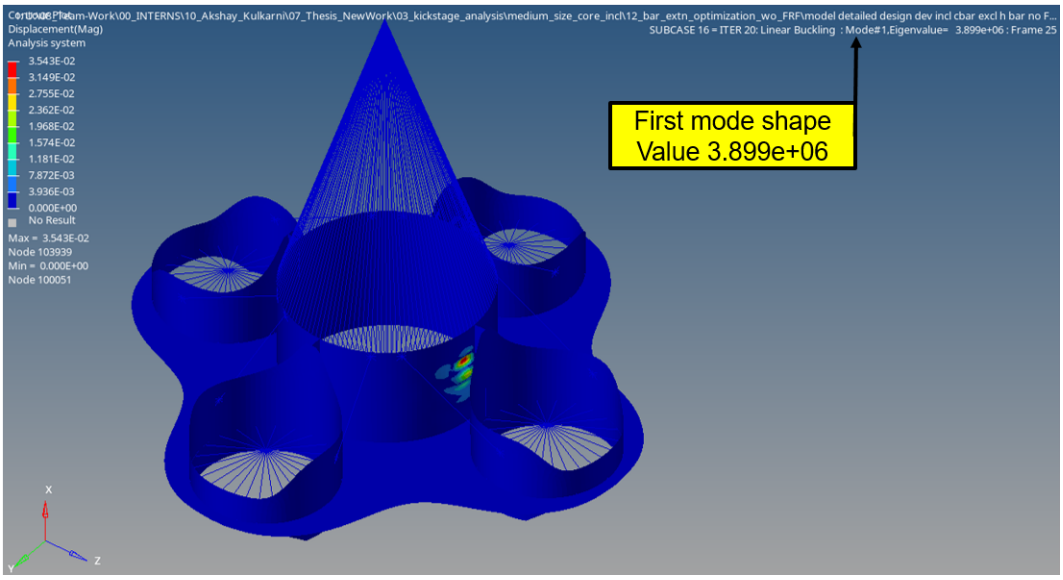

Figure 6.15: Model 1 solution 1 – first buckling mode results

6.6 Model 1 solution 2 – analysis including the frequency response function constraint

In this analysis, the dynamic frequency response calculations are included within the framework of sizing optimization. The upper limit on the constraint for the frequency responses is limiting the responses of the propellant tank nodes to within 9g levels.

6.6.1 Analysis evaluation

The optimization result leads to a structure with modified design parameters. The difference in the result for the first iteration and the final iteration for this configuration can be seen in Figure 6.16. The graph of the change of mass of the structure and the first modal frequency can be seen in Figure 6.17. For the sizing optimization result, the objective mass is minimized from a total of 6009.5kg to 2935.6kg. This results in a frequency drop from 65.8Hz to 47.2Hz, which meets the requirement. Additionally, the thickness plot of the shell mesh is seen in Figure 6.18 and the change of the strut diameter is seen in Figure 6.19. The thicker shells reflect the additional mass present on the main structure to meet the dynamic considerations. The modal analysis results includes the normalized displacement of the first three modes as seen in Figure 6.20 and the modal effective mass plot between the first and the final iteration is Figure 6.21. The difference of the mode shapes and the corresponding effective mass change can be seen here. The dynamic frequency response results are given for all nodes by Figure 6.22 for X direction excitation, Figure 6.23 for Y direction excitation, Figure 6.24 for Z direction excitation. For the node for reference node MON tank, the maximum peak acceleration is 8.72g at 90.1Hz which meets the required limiting value of 9g. Thus, the design impact shows the result in which the mode shapes and the modal effective masses are modified to reduce the peak response. The quasi-static stresses are seen in Figure 6.25. It can be seen here that all the stresses are within the stress constraint limits and found safe. The buckling load for the structure is 2.36E8N and the mode shape is seen in Figure 6.26.

It can be seen that in the case of a mass minimization objective, the solution is driven by the dynamic frequency response solution. The dynamic responses for all tanks are within the limits. The additional mass provided adds to the stiffness of the structure and modifies the mode shapes by redistributing the modal effective masses at particular frequencies. This is seen in the modal effective mass plots between the first and the final iteration in Figure 6.21, and the frequency response curves.

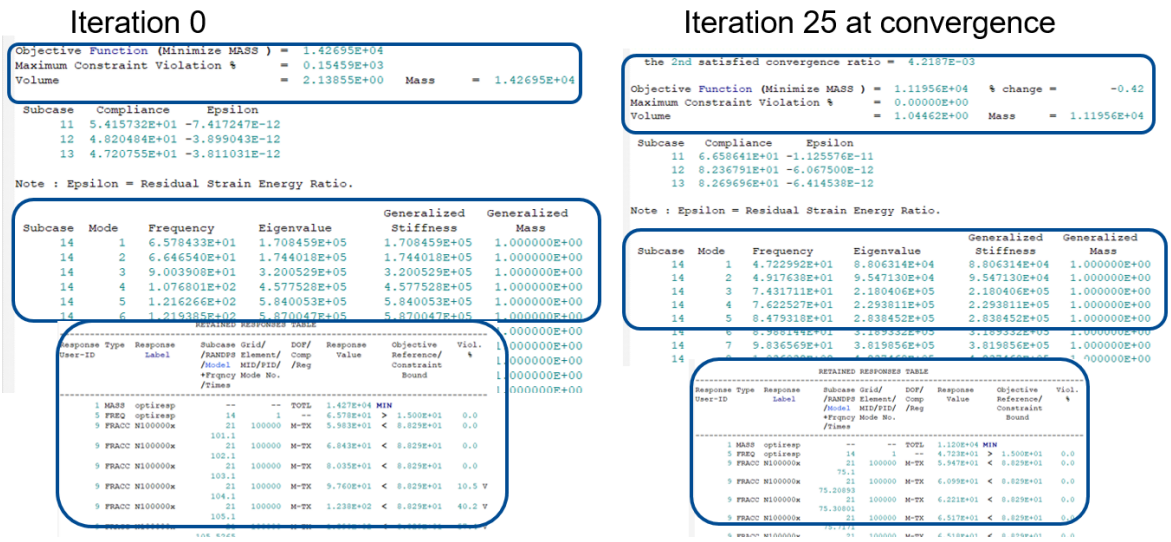

Figure 6.16: Model 1 solution 2 – iteration data comparison

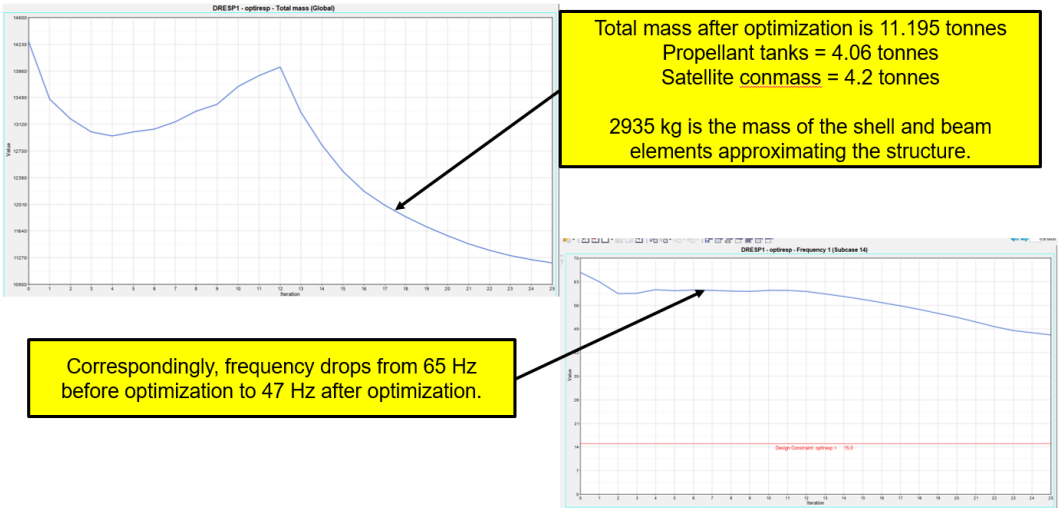

Figure 6.17: Model 1 solution 2 – mass and frequency data comparison

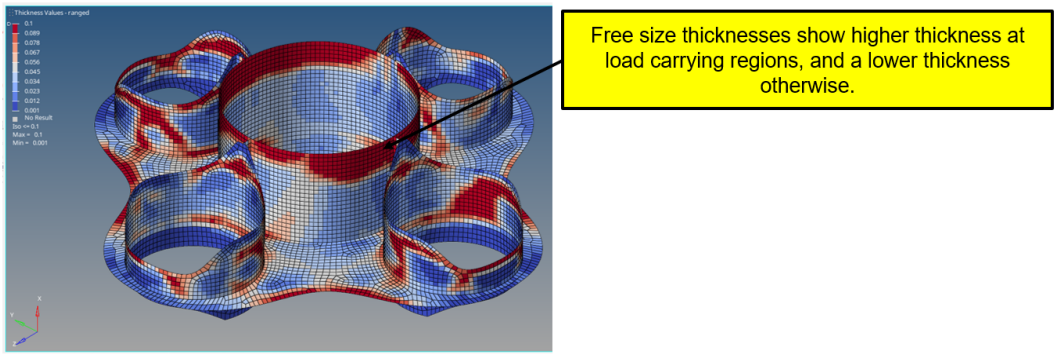

Figure 6.18: Model 1 solution 2 – mass distribution for the free size shell optimization

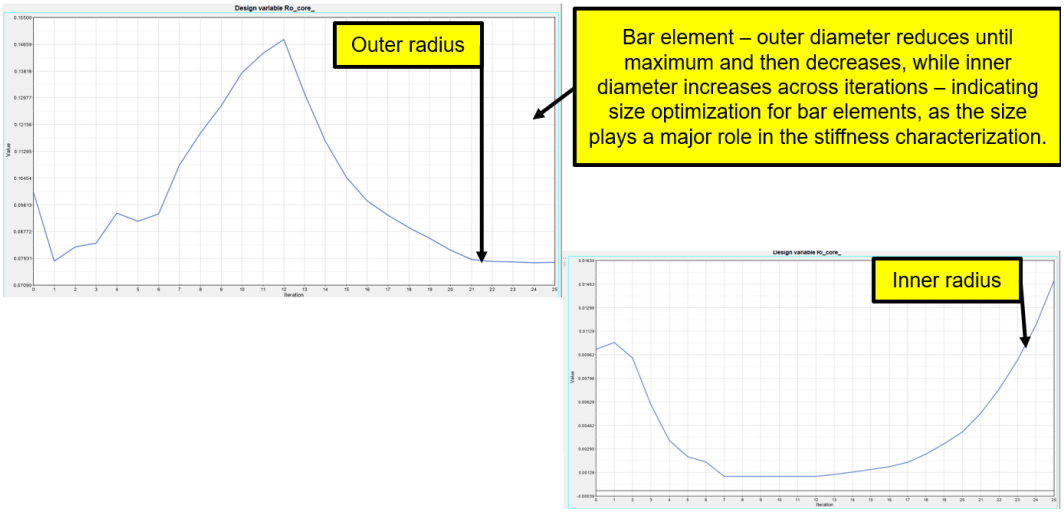

Figure 6.19: Model 1 solution 2 – strut diameter across iterations

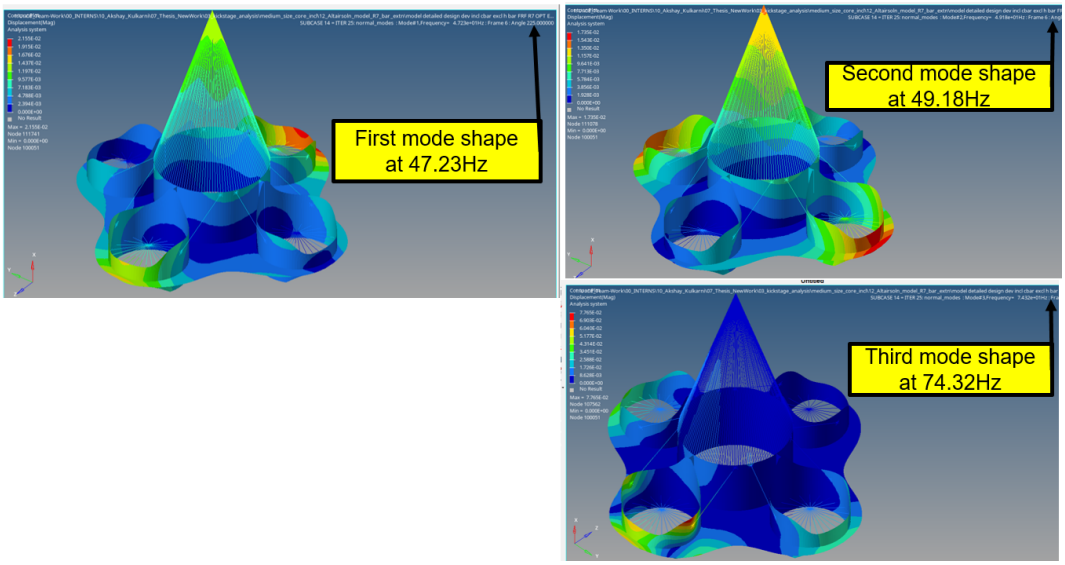

Figure 6.20: Model 1 solution 2 – Modal analysis results for the converged iteration

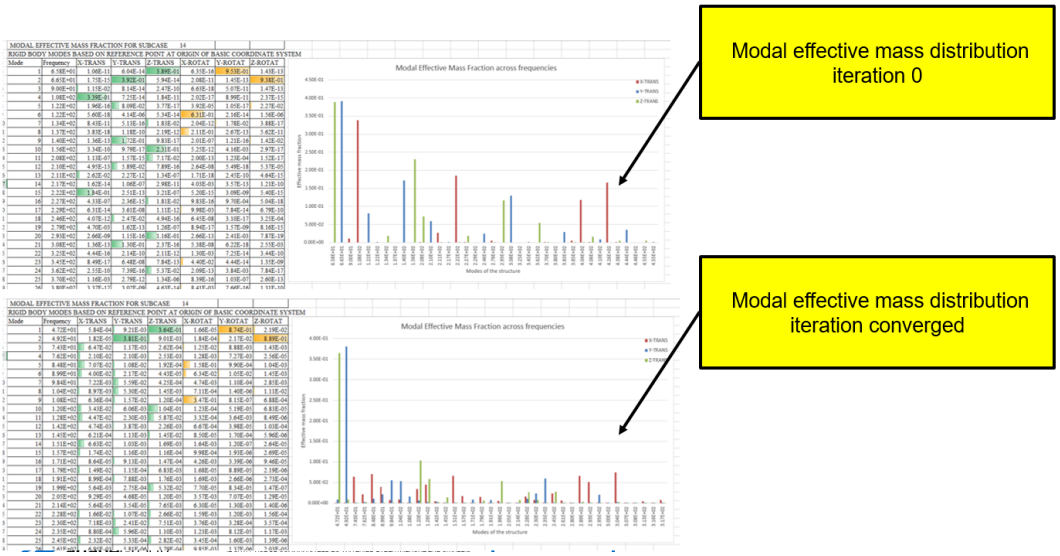

Figure 6.21: Model 1 solution 2 – modal effective mass fraction for the starting and converged iteration

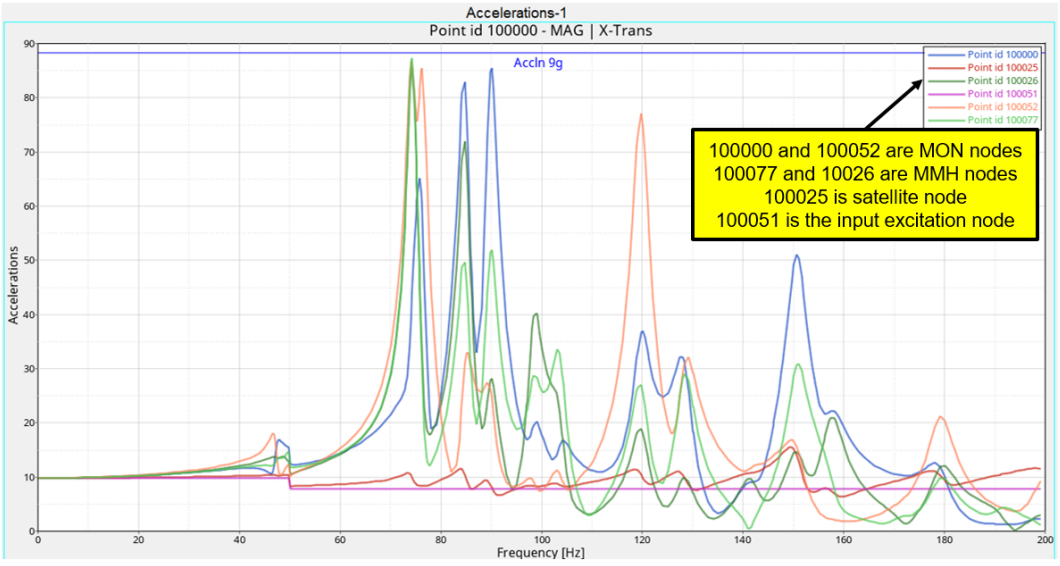

Figure 6.22: Model 1 solution 2 – Dynamic analysis results for the converged iteration – X excitation

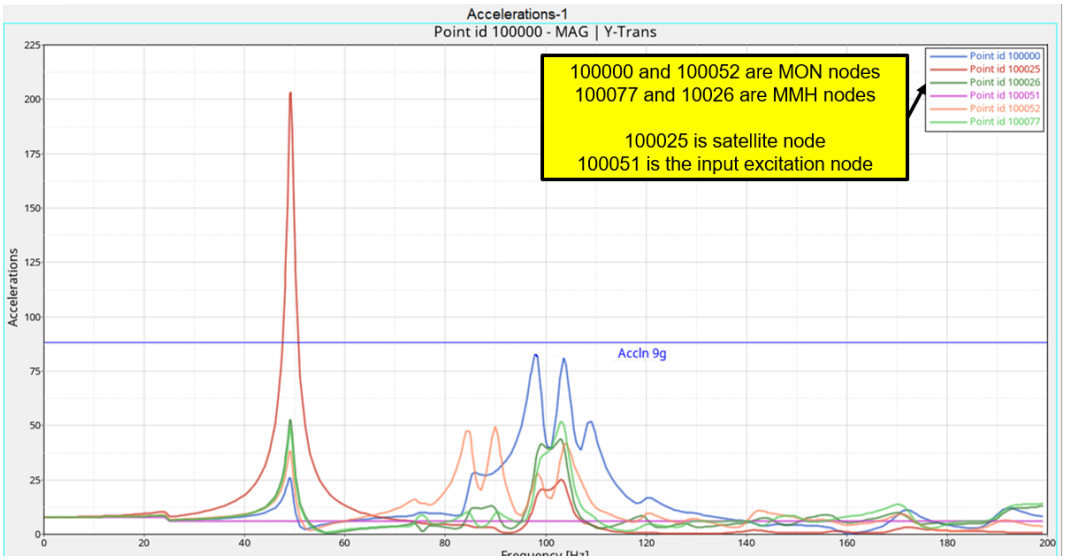

Figure 6.23: Model 1 solution 2 – dynamic analysis results for the converged iteration – Y excitation

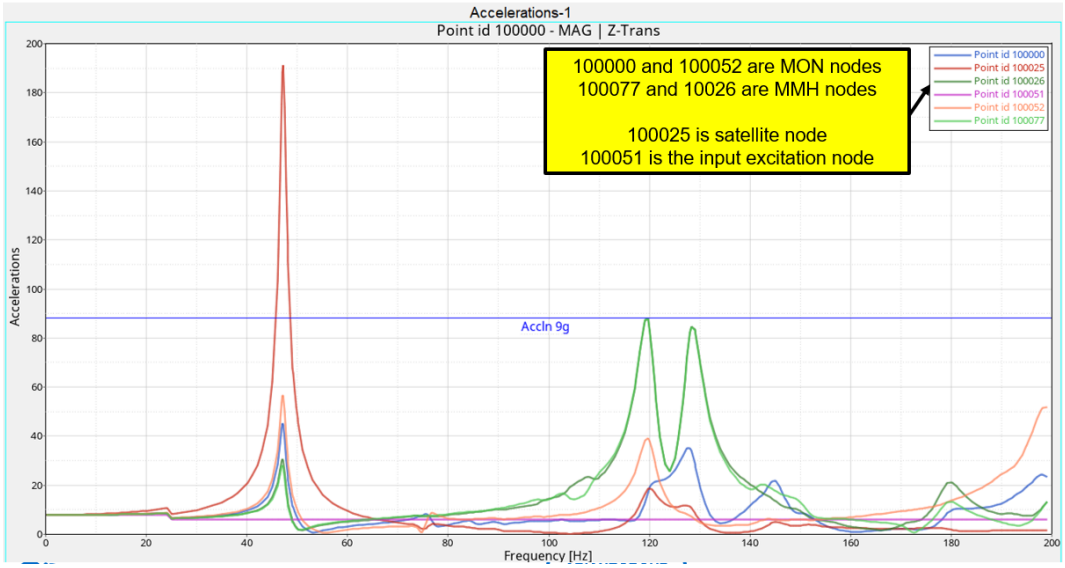

Figure 6.24: Model 1 solution 2 – dynamic analysis results for the converged iteration – Z excitation

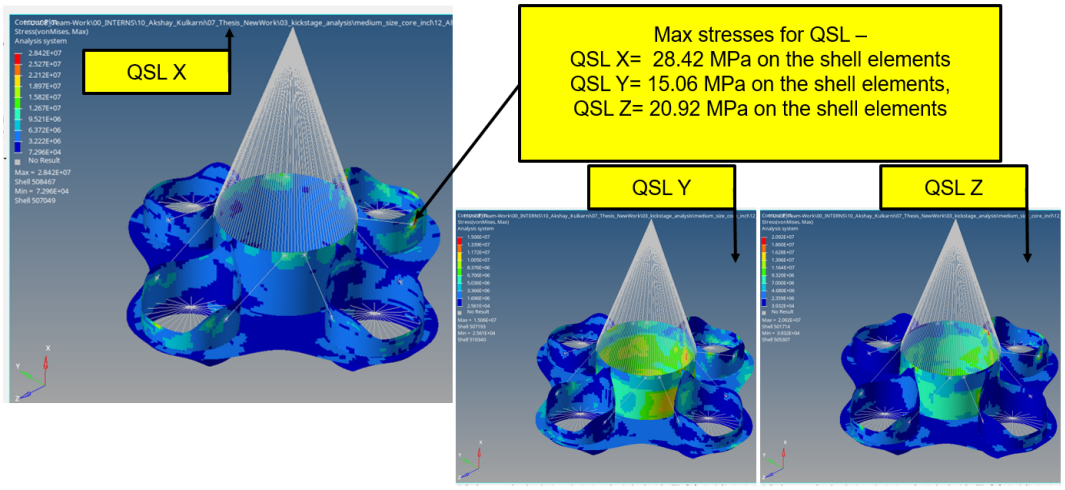

Figure 6.25: Model 1 solution 2 – quasi-static stresses results

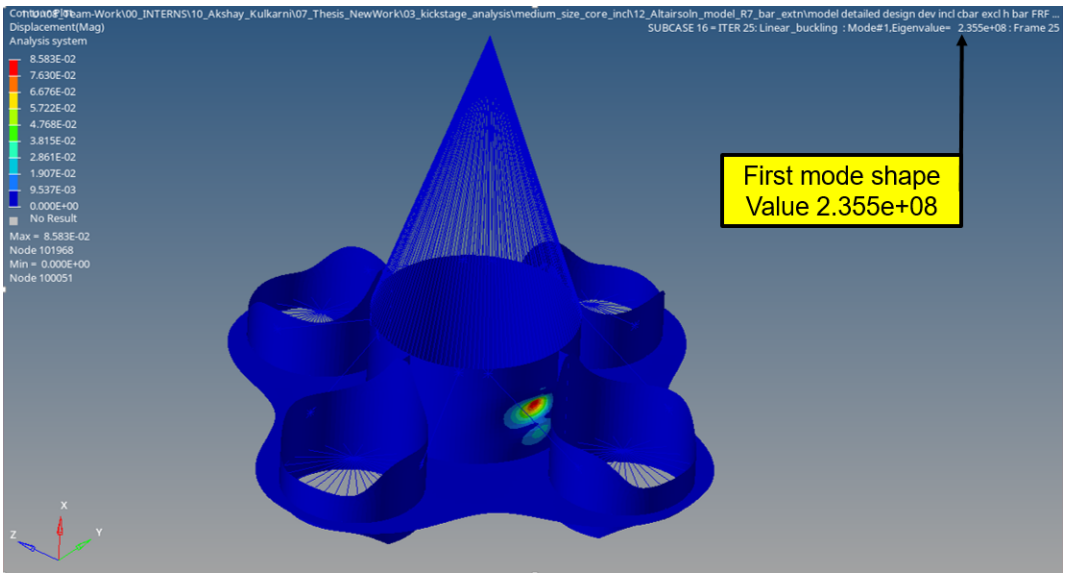

Figure 6.26: Model 1 solution 2 – first buckling mode results

6.7 Model 1 solution 3 – analysis including the frequency response function constraint with a reduced input excitation

The specifications on the dynamic frequency response input, in this case, the sine input function is considered as per the launcher user manual [6]. There are safety factors prescribed on top of the actual vibration profiles seen during the launcher development. An additional notching factor can also be requested to reduce the input at certain frequencies. Combining these factors, a new input spectrum of one-fifth of the original sine input specification is then considered in this analysis. These reduced dynamic frequency response calculations are included within the framework of sizing optimization iteration. The response is notched from a level of 1g to a level of 0.2g. The upper limit on the constraint for the frequency responses is limiting the responses of the propellant tank nodes to within 9g levels.

6.7.1 Analysis evaluation

The optimization result leads to a structure with modified design parameters. The difference in the result for the first iteration and the final iteration for this configuration can be seen in Figure 6.27. The graph of the change of mass of the structure and the first modal frequency can be seen in Figure 6.28. For the sizing optimization result, the objective mass is minimized from a total of 6009.5kg to 326.7kg. This results in a frequency drop from 65.8Hz to 15.0Hz, which meets the requirement. Additionally, the thickness plot of the shell mesh is seen in Figure 6.29 and the change of the strut diameter is seen in Figure 6.30. The modal analysis results includes the normalized displacement of the first three modes as seen in Figure 6.31 and the modal effective mass plot between the first and the final iteration is Figure 6.32. The difference of the mode shapes and the corresponding effective mass change can be seen here. The dynamic frequency response results are given for all nodes by Figure 6.33 for X direction excitation, Figure 6.34 for Y direction excitation, Figure 6.35 for Z direction excitation. For the node for reference node MON tank, the maximum peak acceleration is 2.85g at 20.0Hz which is within the qualification value of 9g. The quasi-static stresses are seen in Figure 6.36. It can be seen here that all the stresses are within the stress constraint limits and found safe. The buckling load for the structure is 4.47E6N and the mode shape is seen in Figure 6.37.

It can be seen that in the case of a mass minimization objective, the solution is driven by the frequency requirement, as the dynamic peak responses for all tanks are within the limits. In practicality, this is an extreme case, with the real case being somewhere in between case 2 and case 3. The solutions for such cases can be a combination of load inputs with some frequencies being notched to a low value of one-fifth and others being full level. This combination will depend on the other systems on the launcher and the sensitivity of the payload to certain frequencies.

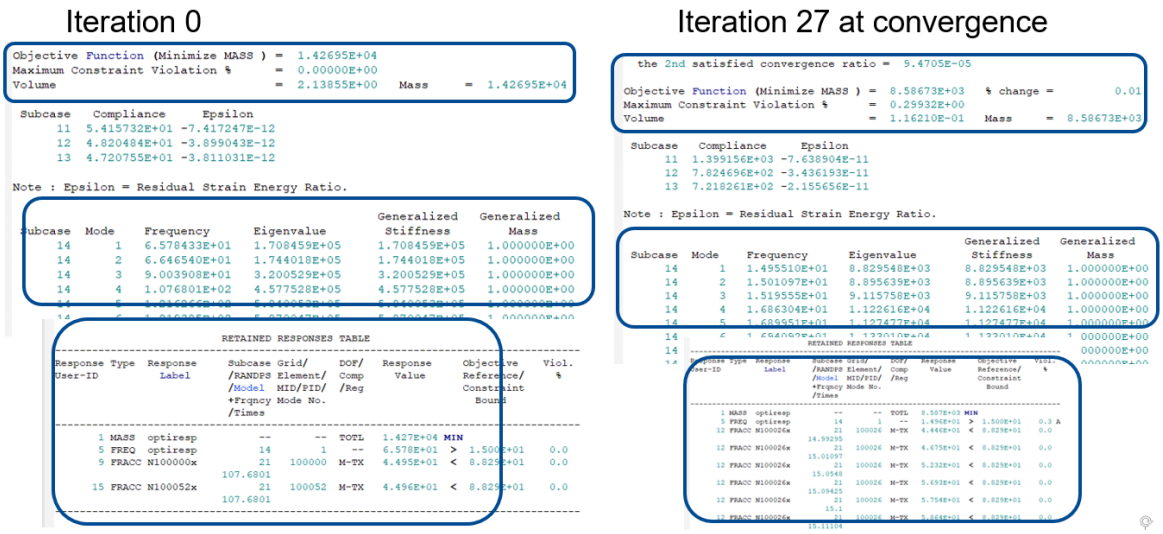

Figure 6.27: Model 1 solution 3 – iteration data comparison

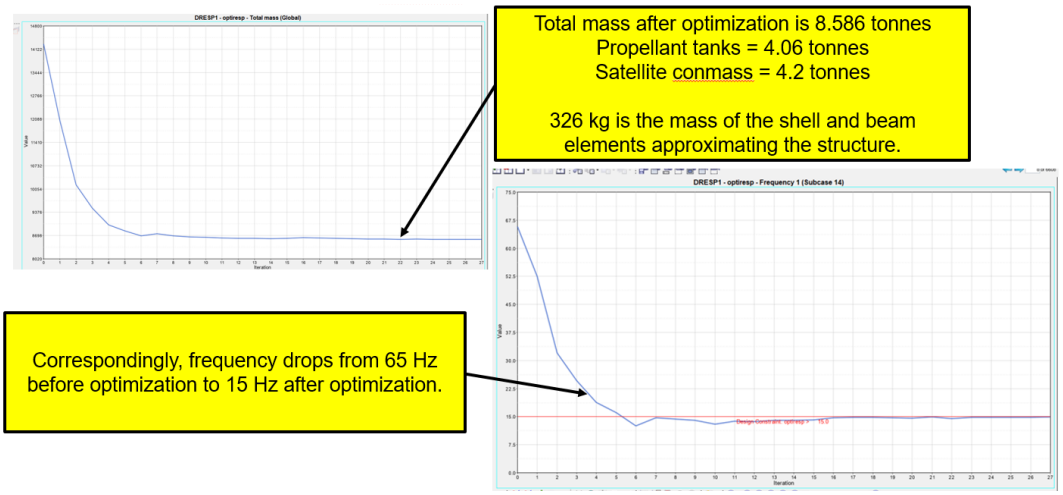

Figure 6.28: Model 1 solution 3 – mass and frequency data comparison

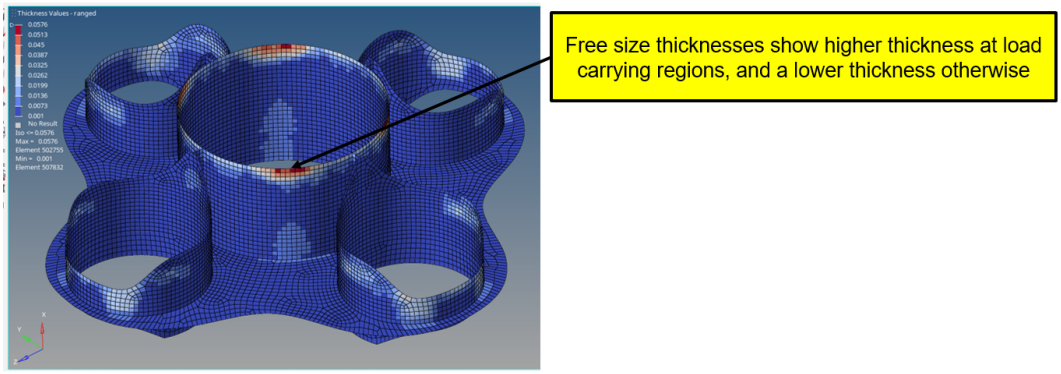

Figure 6.29: Model 1 solution 3 – mass distribution for the free size shell optimization

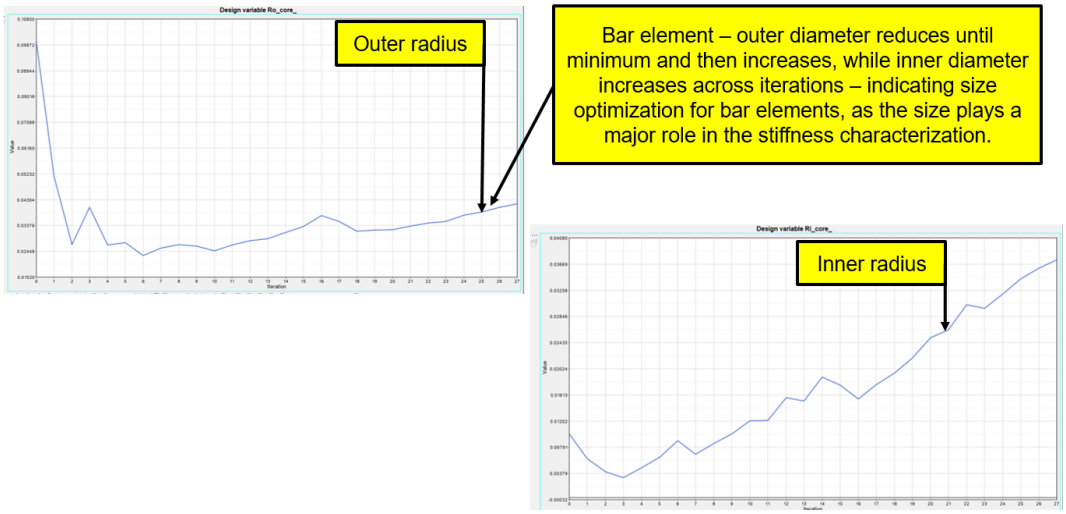

Figure 6.30: Model 1 solution 3 – strut diameter across iterations

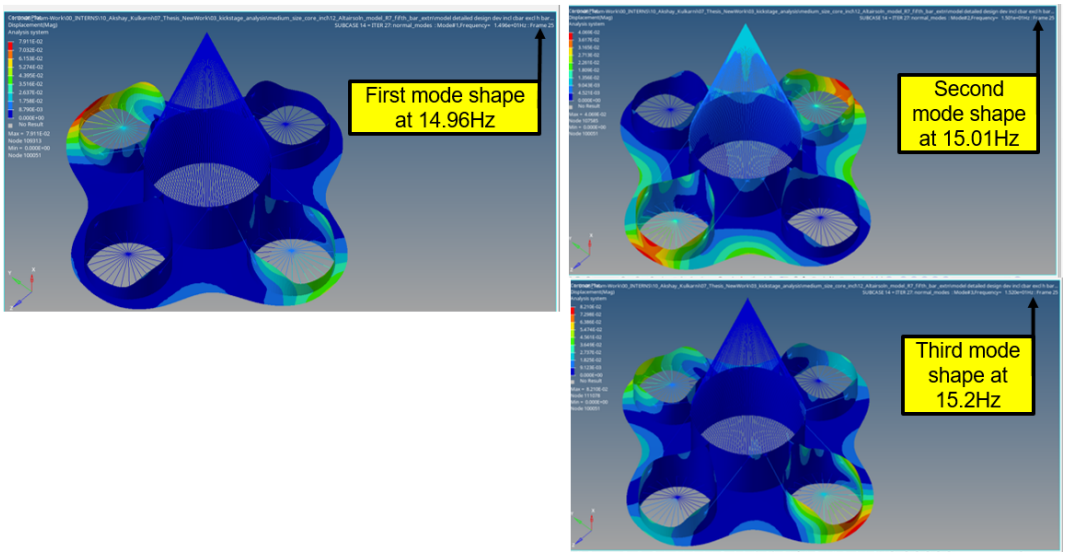

Figure 6.31: Model 1 solution 3 – modal analysis results for the converged iteration

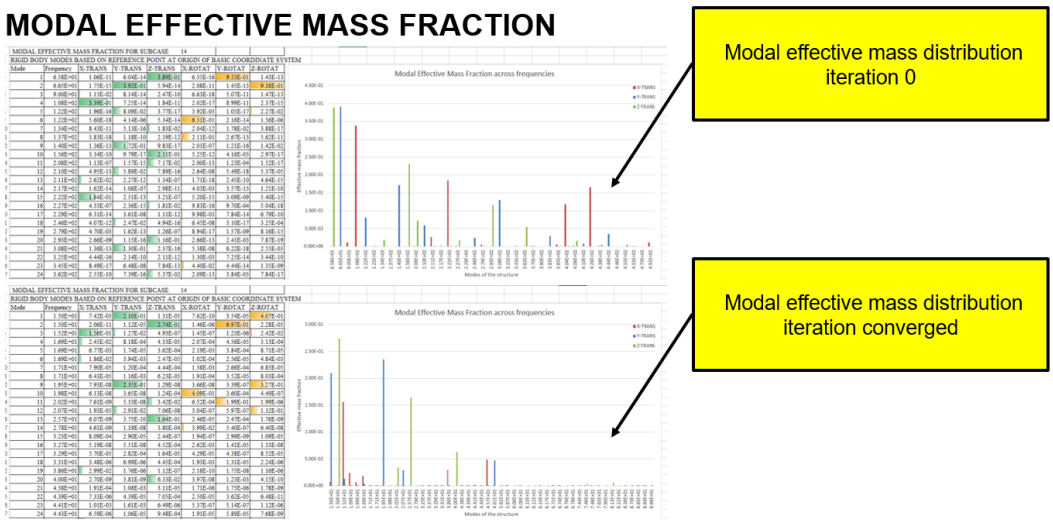

Figure 6.32: Model 1 solution 3 – modal effective mass fraction for the starting and converged iteration

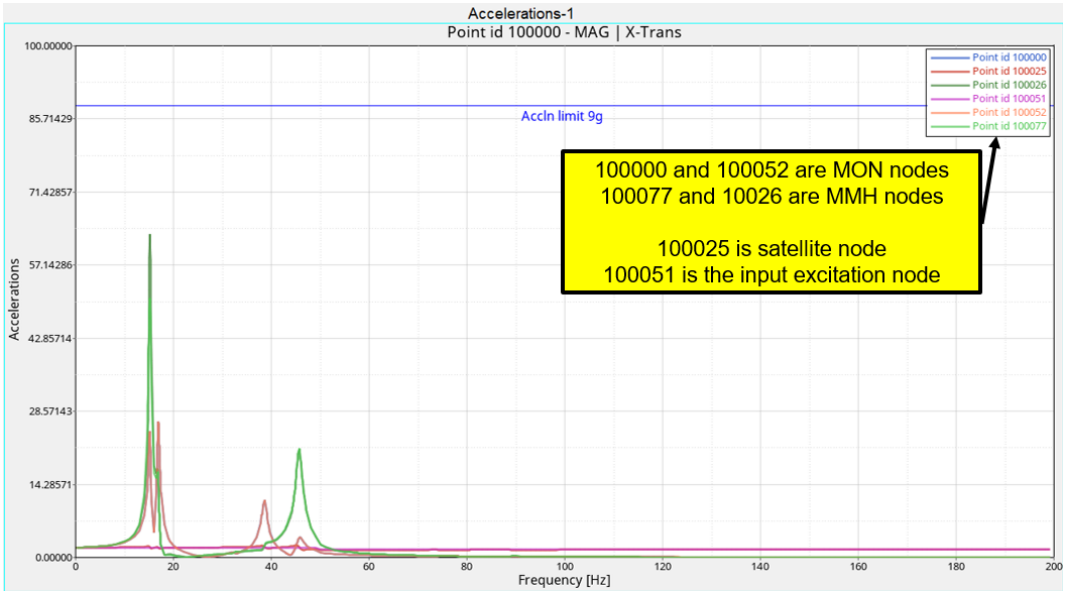

Figure 6.33: Model 1 solution 3 – dynamic analysis results for the converged iteration – X excitation

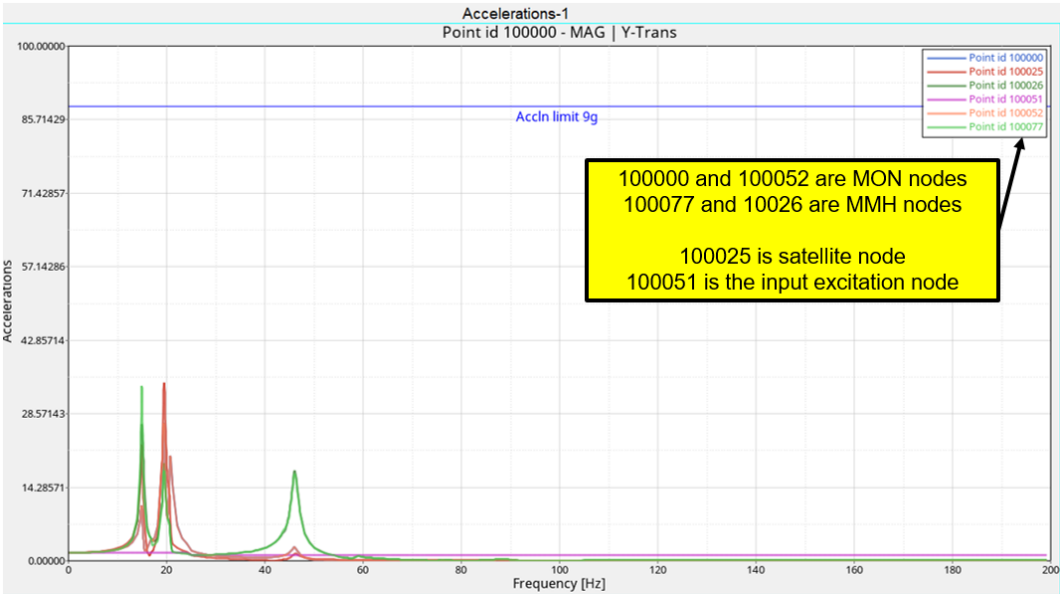

Figure 6.34: Model 1 solution 3 – dynamic analysis results for the converged iteration – Y excitation

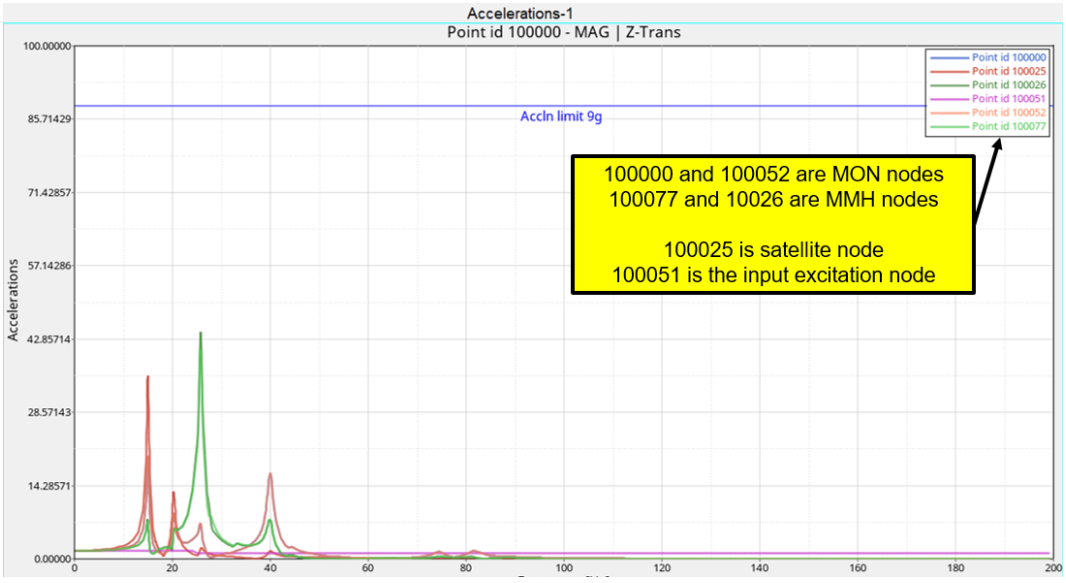

Figure 6.35: Model 1 solution 3 – dynamic analysis results for the converged iteration – Z excitation

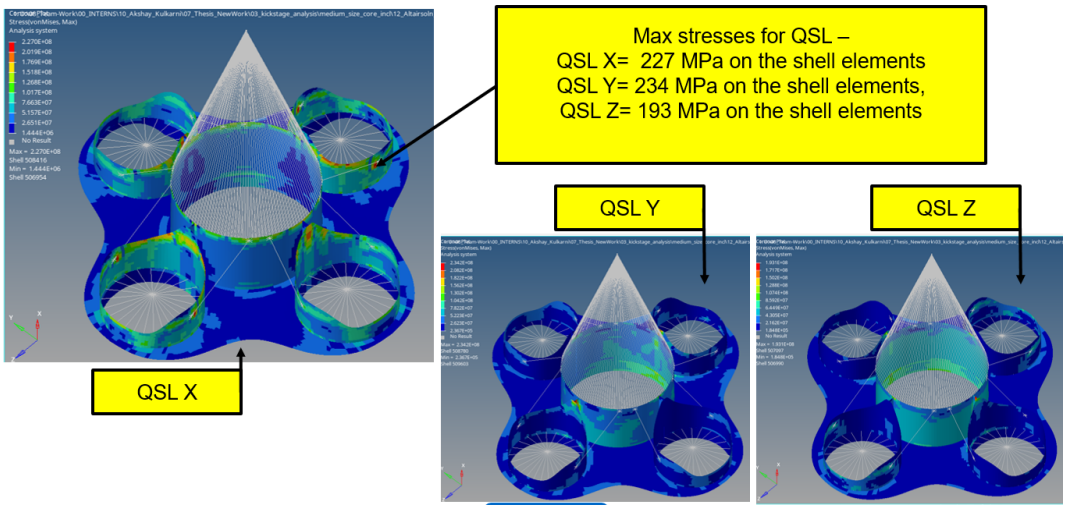

Figure 6.36: Model 1 solution 3 – quasi-static stresses results

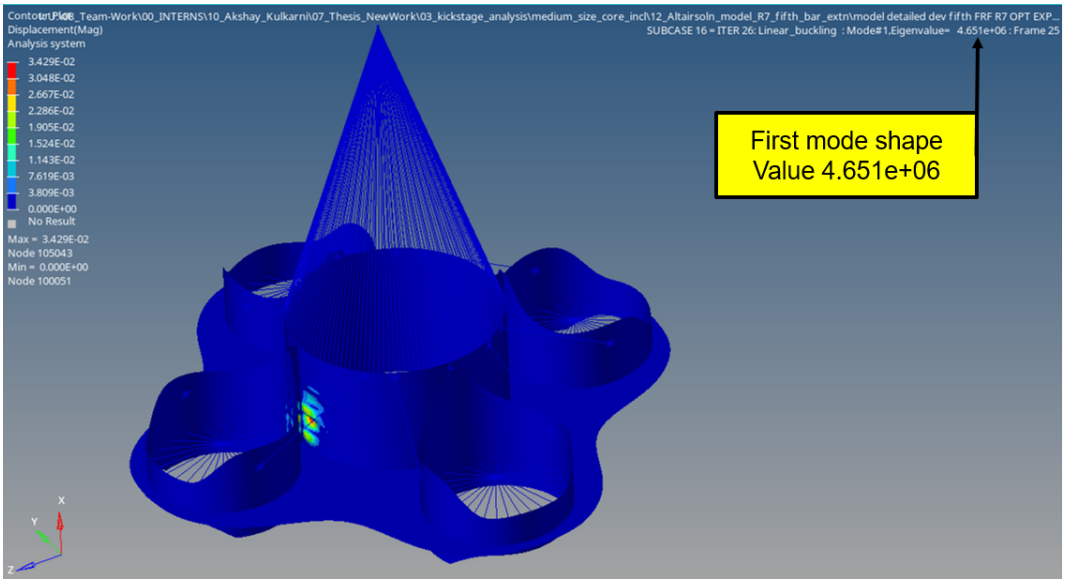

Figure 6.37: Model 1 solution 3 – first buckling mode results

6.8 Model 1 result interpretation and discussion

The comparison of the results for Model 1 can be seen in Table 6.1. It can be seen that the first case of the topology-optimized result has the highest mass but also has a higher peak response for the propellant tank. sizing optimization helps us reduce the extra mass until we get to a more manageable mass budget, while the frequency requirement is being met. The best-case scenario of meeting the peak loading requirement is realized by solution 2, however, the mass budget is also high. It is interesting that the regions of mass distribution change significantly in Solution 2 and the modal effective mass distribution table also changes between the first and last iteration. This solution also provides a higher buckling load. This indicates that while it would be useful to implement this solution to some frequency intervals, the higher mass budget due to it, would not be acceptable. Solution 3 has a reduced input so it is valid that all the responses are within the peak response values. In practicality, a notching request cannot be possible for the entire spectrum. Hence, a good design can include these design methodology implications from Solution 2 and Solution 3 combined. It can also be seen that the stresses in all three solutions are within limits. Thus, the sizing optimization is driven primarily by the dynamic behavior of the structure and the size modification can be useful to assist in some frequency intervals, while being ignored at other intervals.

Model 1 - with inclined strut support elements				
	Baseline 0th Iteration	Solution 1 - after optimization	Solution 2 - after optimization	Solution 3 - after optimization
Description- for the result	Baseline 0th Iteration	Dynamic sine without optimization	Dynamic sine with optimization	one fifth Dynamic sine with optimization
Structural mass (in kg) - excluding conm2	6009.50	401.00	2935.60	326.70
First frequency mode (in Hz)	65.8	14.9	47.2	15.0
Peak Dynamic response for MON node 100 000 (in g)	22.83	16.31	8.72	2.85
Excitation direction	X	Y	X	Y
Above Peak dynamic response is at frequency (in Hz)	107.68	19.69	90.10	20.00
First buckling mode value (in N)	1.32E+09	3.90E+06	2.36E+08	4.47E+06

Table 6.1: Summary table for the Model 1 sizing optimization analysis

The mass distribution of different 2D elements after optimization can be seen in Table 6.2. It can be seen here that the central core has about 30% mass budget of the total structure. The circular panels along the propellant tanks get more stiffened for the case with full load base input excitation, indicating that the mass redistribution occurs in this region to affect the modal and dynamic behaviour of the structure. The strut element sizing varies proportional

to the loading conditions on the propellant tanks, indicating that the design can be tuned by increasing the thickness, leading correspondingly the elemental stiffness of the strut elements.

Model 1 - with inclined strut support elements				
Mass distribution of size optimized results		Solution 1 - after optimization	Solution 2 - after optimization	Solution 3 - after optimization
Mass distribution	Result description	Dynamic sine without optimization	Dynamic sine with optimization	one fifth Dynamic sine with optimization
Central core	absolute (in kg)	127.01	879.20	116.60
	fraction (in %)	31.67%	29.95%	35.69%
Circular panels around the propellant tanks	absolute (in kg)	117.90	1059.00	111.20
	fraction (in %)	29.40%	36.07%	34.04%
Bottom flat panel	absolute (in kg)	87.76	615.70	77.22
	fraction (in %)	21.89%	20.97%	23.64%
Strut elements	absolute (in kg)	68.33	381.70	21.68
	fraction (in %)	17.04%	13.00%	6.64%

Table 6.2: Mass distribution summary table of the Model 1 sizing optimization analysis

Chapter 7

Sizing Optimization 2 – shear panel design

This chapter discusses the sizing optimization results of the model 2 design. The design includes using shear panels mounted along the propellant tanks for better stability and load path transfer.

7.1 Model 2 description and designed solutions

In this model, the connection from the central core to the propellant tanks is modeled by shear webs which are in turn modeled by 2D shell elements. The model is shown in Figure 7.1.

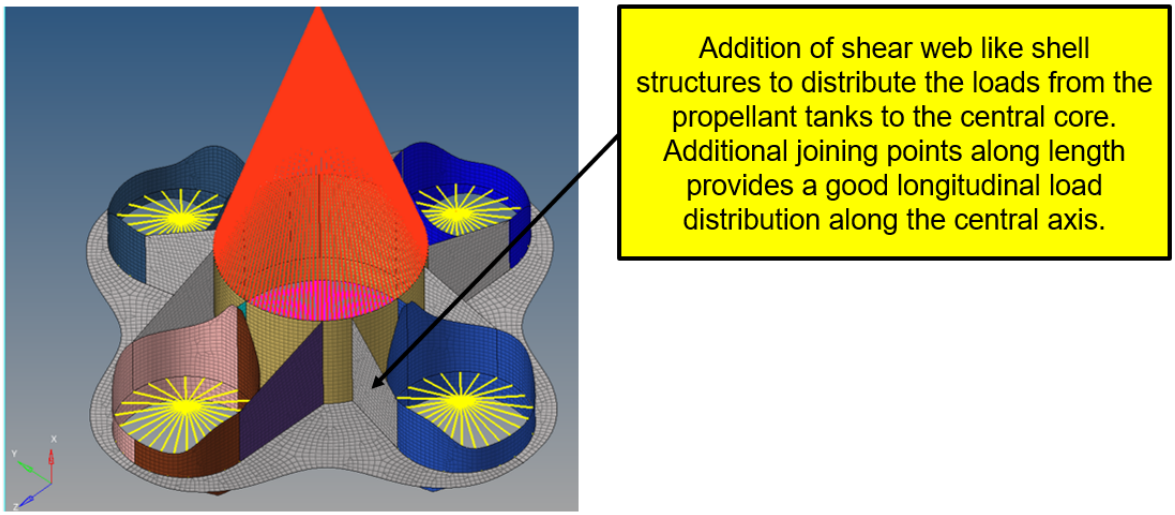

Figure 7.1: Description of Model 2 – input mesh for sizing optimization study

7.2 Model 2 solution 1 – analysis excluding the frequency response function constraint

Similar to model 1, the first analysis does not have the frequency response calculations defined within the sizing optimization loop. This is to understand the driving conditions for the analysis convergence when the dynamic frequency response is not an optimization constraint.

7.2.1 Analysis evaluation

The optimization result leads to a structure with modified design parameters. The difference in the result for the first iteration and the final iteration for this configuration can be seen in Figure 7.2. The graph of the change of mass of the structure and the first modal frequency can be seen in Figure 7.3. For the sizing optimization result, the objective mass is minimized from a total of 6486.7kg to 450.22kg. This results in a frequency drop from 69.7Hz to 15.0Hz, which meets the requirement. Additionally, the thickness plot of the shell mesh is seen in Figure 7.4. The modal analysis results include the normalized displacement of the first three modes as seen in Figure 7.5 and the modal effective mass plot between the first and the final iteration is Figure 7.6. The difference of the mode shapes and the corresponding effective mass change can be seen here. The dynamic frequency response results are given for all nodes by Figure 7.7 for X direction excitation, Figure 7.8 for Y direction excitation, Figure 7.9 for Z direction excitation. For the node for reference node MON tank, the maximum peak acceleration is 21.92g at 17Hz which is exceeding the qualification value of 9g. The quasi-static stresses are seen in Figure 7.10. It can be seen here that all the stresses are within the stress constraint limits and found safe. The buckling load for the structure is 3.22E6N and the mode shape is seen in Figure 7.11.

It can be seen that in the case of a mass minimization objective, the solution is driven by the frequency requirements constraint. However, the peak responses in directions exceed the propellant tank qualification value. Hence, the next step is to include these responses within the optimization framework.

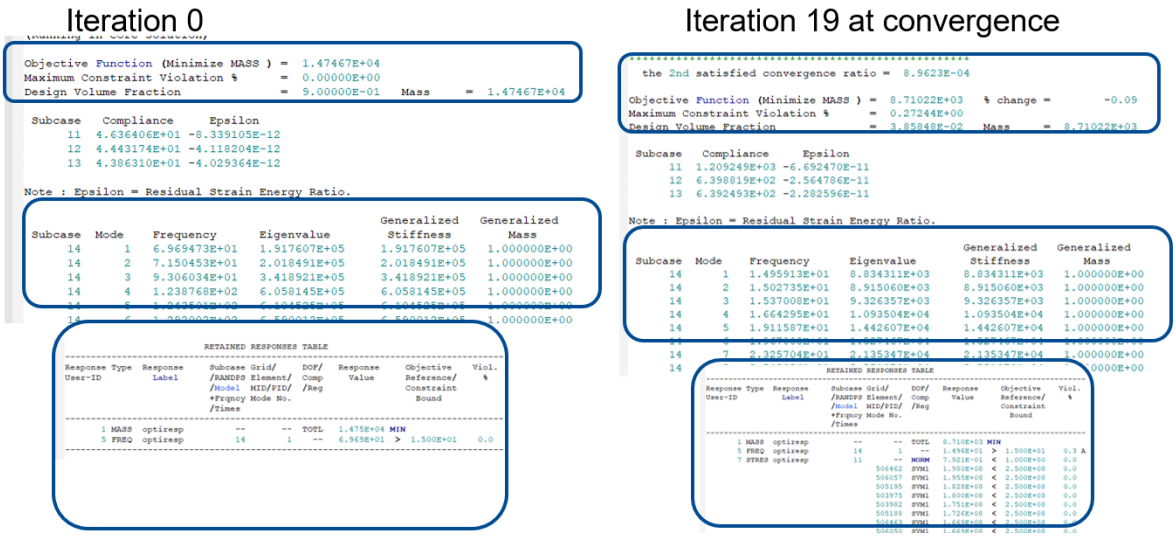

Figure 7.2: Model 2 solution 1 – iteration data comparison

Figure 7.3: Model 2 solution 1 – mass and frequency data comparison

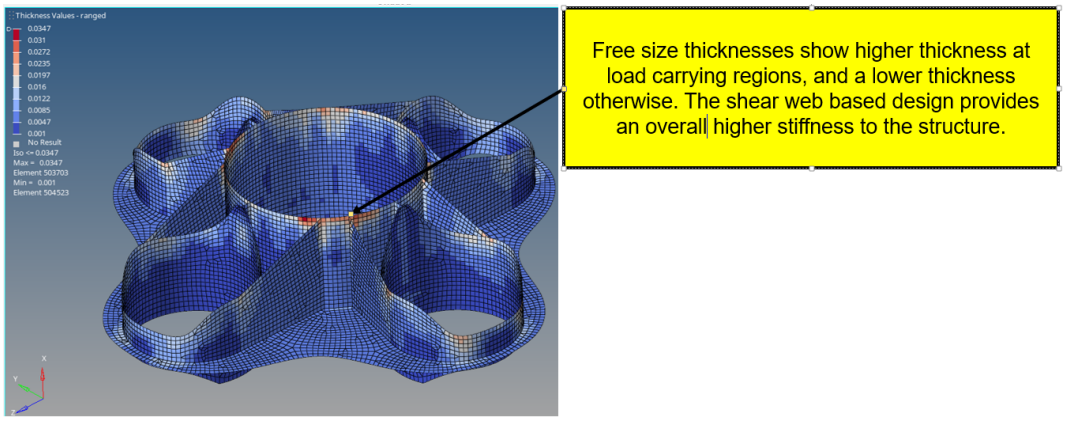

Figure 7.4: Model 2 solution 1 – mass distribution for the free size shell optimization

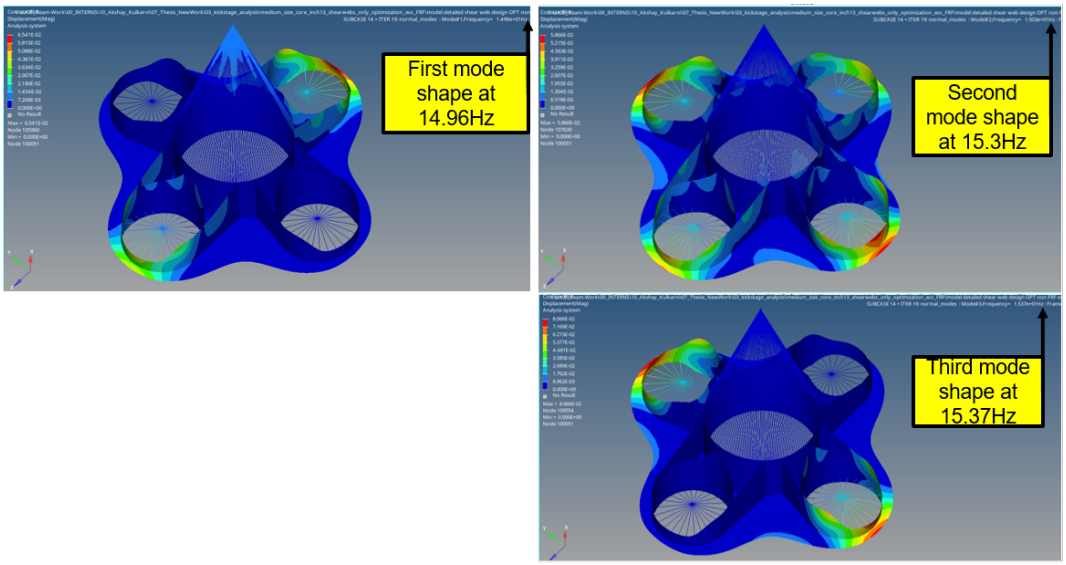

Figure 7.5: Model 2 solution 1 – modal analysis results for the converged iteration

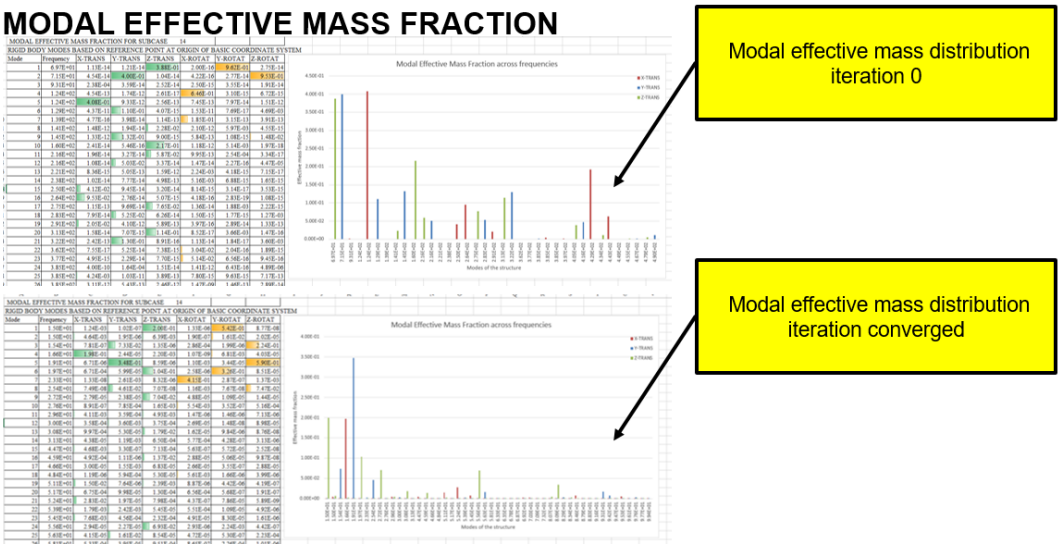

Figure 7.6: Model 2 solution 1 – modal effective mass fraction for the starting and converged iteration

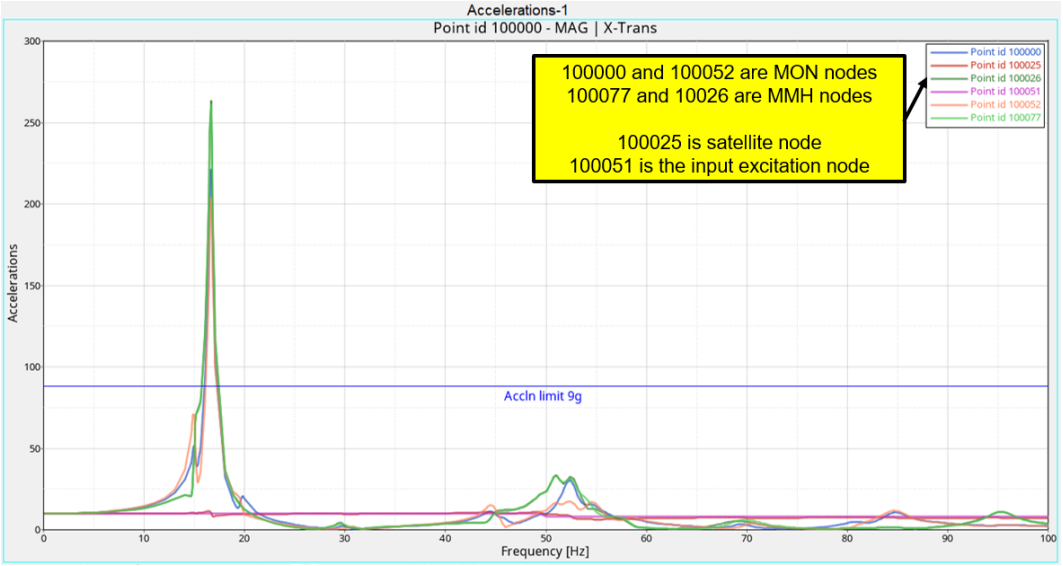

Figure 7.7: Model 2 solution 1 – dynamic analysis results for the converged iteration – X excitation

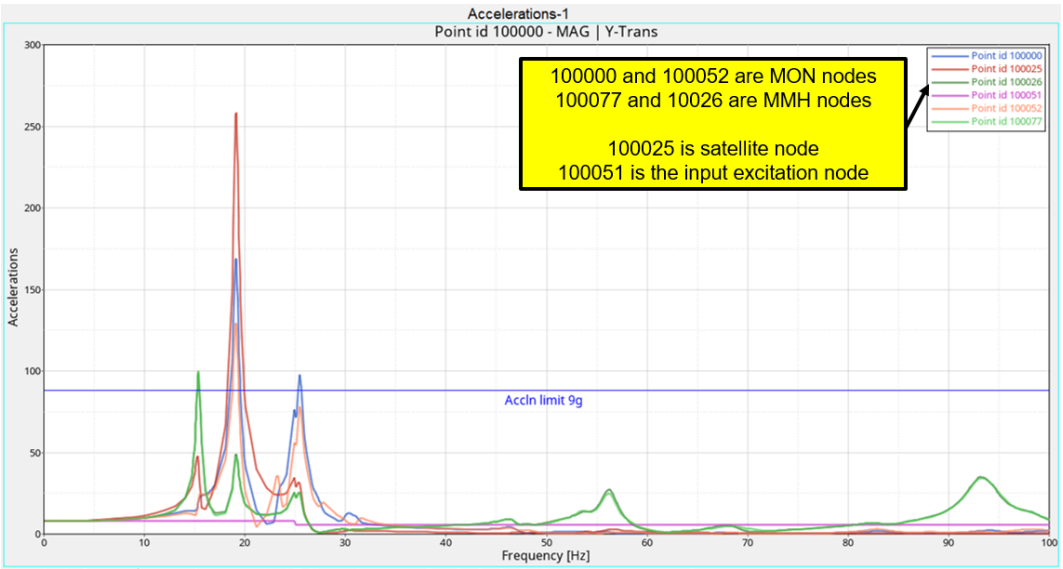

Figure 7.8: Model 2 solution 1 – dynamic analysis results for the converged iteration – Y excitation

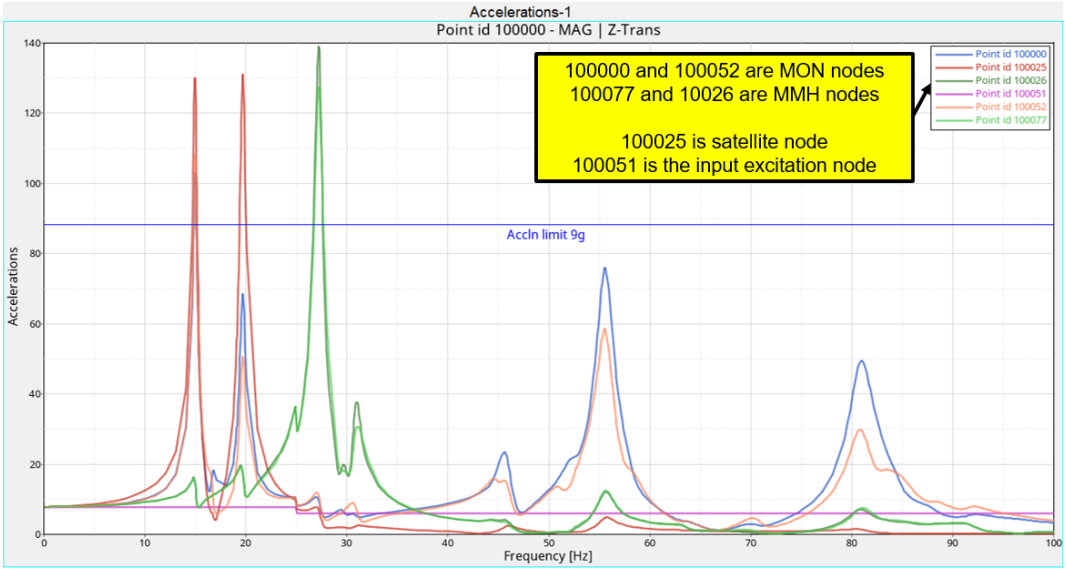

Figure 7.9: Model 2 solution 1 – dynamic analysis results for the converged iteration – Z excitation

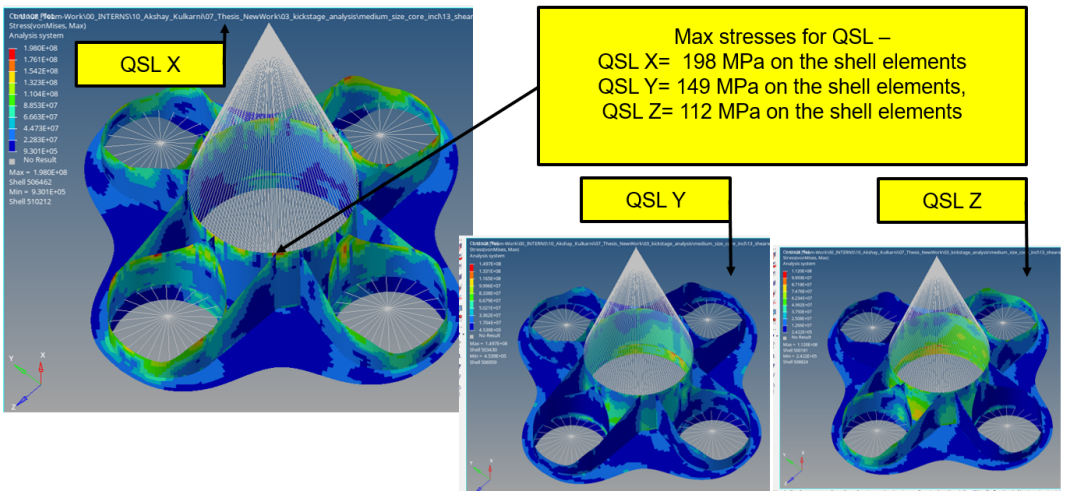

Figure 7.10: Model 2 solution 1 – quasi-static stresses results

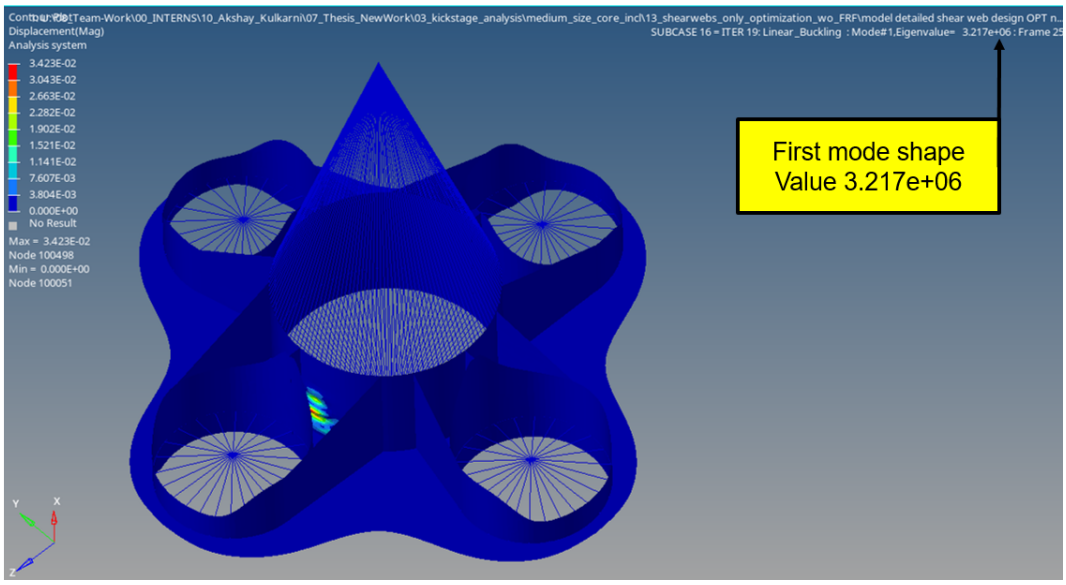

Figure 7.11: Model 2 solution 1 – first buckling mode results

7.3 Model 2 solution 2 – analysis including the frequency response function constraint

Similar to the earlier model, the dynamic frequency response calculations are included within the framework of sizing optimization. The upper limit on the constraint for the frequency responses is limiting the responses of the propellant tank nodes to within 9g levels.

7.3.1 Analysis evaluation

The optimization result leads to a structure with modified design parameters. The difference in the result for the first iteration and the final iteration for this configuration can be seen in Figure 7.12. The graph of the change of mass of the structure and the first modal frequency can be seen in Figure 7.13. For the sizing optimization result, the objective mass is minimized from a total of 6009.5kg to 2977.4kg. This results in a frequency drop from 69.7Hz to 49.9Hz, which meets the requirement. Additionally, the thickness plot of the shell mesh is seen in Figure 7.14. The thicker shells reflect the additional mass present on the main structure to meet the dynamic considerations. The modal analysis results include the normalized displacement of the first three modes as seen in Figure 7.15 and the modal effective mass plot between the first and the final iteration is Figure 7.16. The difference of the mode shapes and the corresponding effective mass change can be seen here. The dynamic frequency response results are given for all nodes by Figure 7.17 for X direction excitation, Figure 7.18 for Y direction excitation, Figure 7.19 for Z direction excitation. For the node for reference node MON tank, the maximum peak acceleration is 9.00g at 90.0Hz which meets the required limiting value of 9g. The quasi-static stresses are seen in Figure 7.20. It can be seen here that all the stresses are within the stress constraint limits and found safe. The buckling load for the structure is 9.25E7N and the mode shape is seen in Figure 7.21.

It can be seen that in the case of a mass minimization objective, the solution is driven by the dynamic frequency response solution. The dynamic responses for all tanks are within the limits. The additional mass provided adds to the stiffness of the structure and modifies the mode shapes by redistributing the modal effective masses at particular frequencies. This is seen in the modal effective mass plots between the first and the final iteration in Figure 7.16, and the frequency response curves.

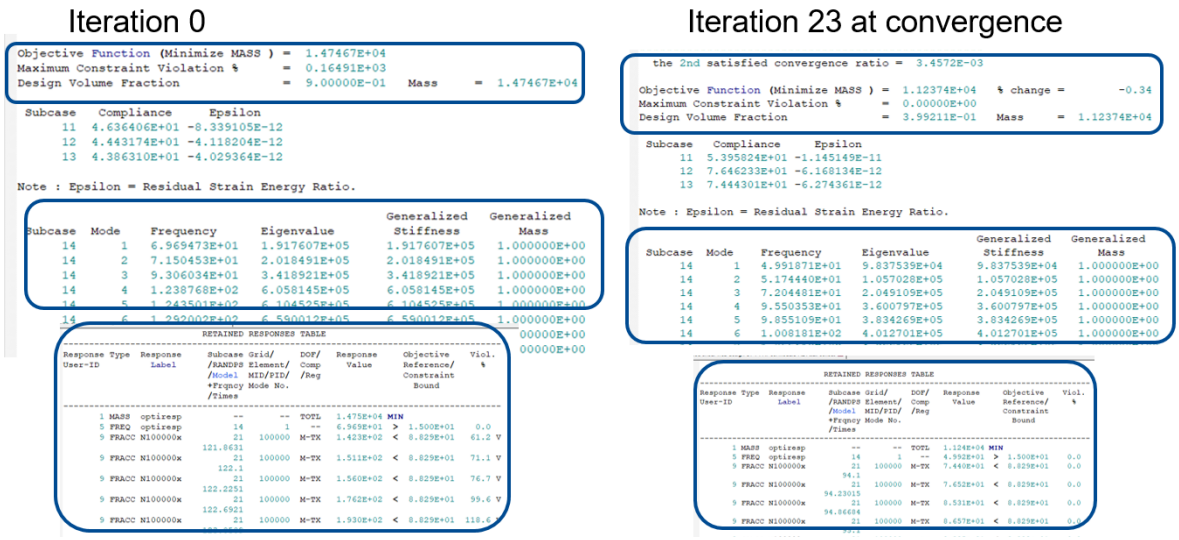

Figure 7.12: Model 2 solution 2 – iteration data comparison

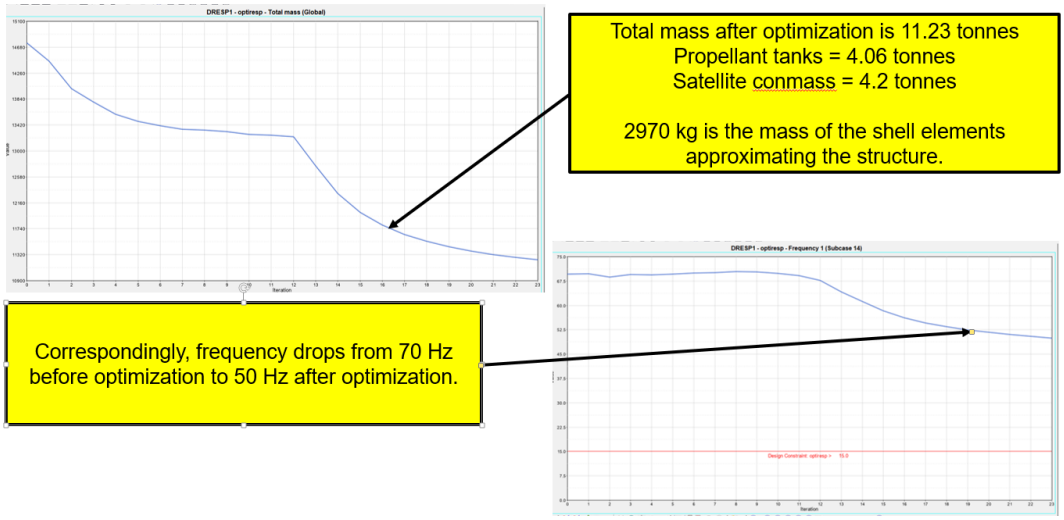

Figure 7.13: Model 2 solution 2 – mass and frequency data comparison for Model 1 iterations

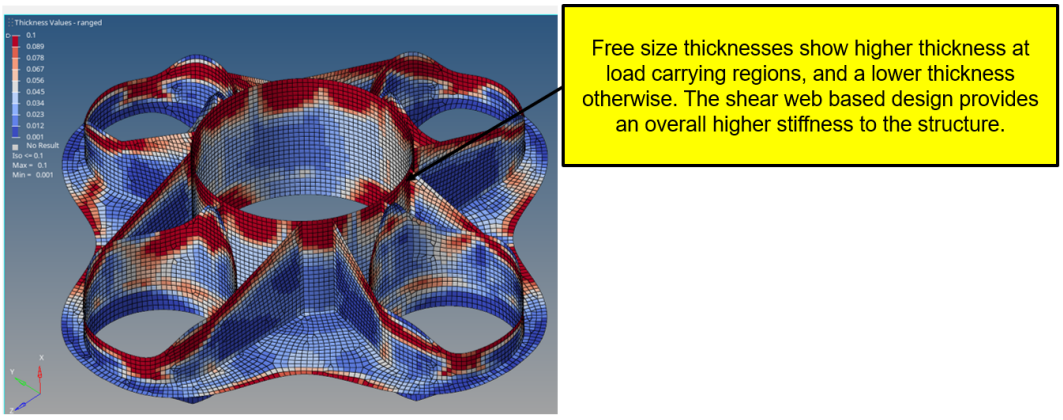

Figure 7.14: Model 2 solution 2 – mass distribution for the free size shell optimization

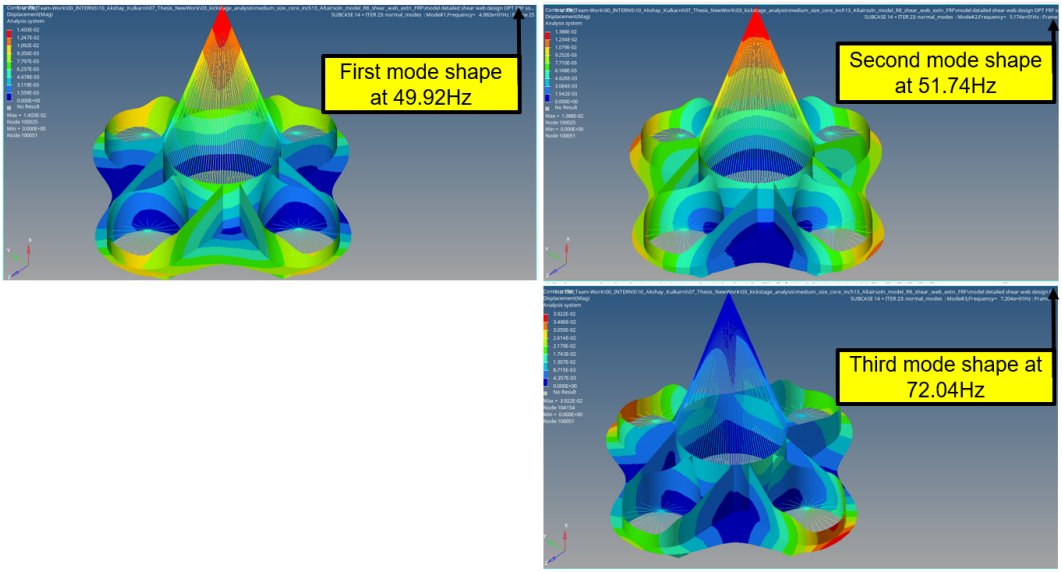

Figure 7.15: Model 2 solution 2 – modal analysis results for the converged iteration

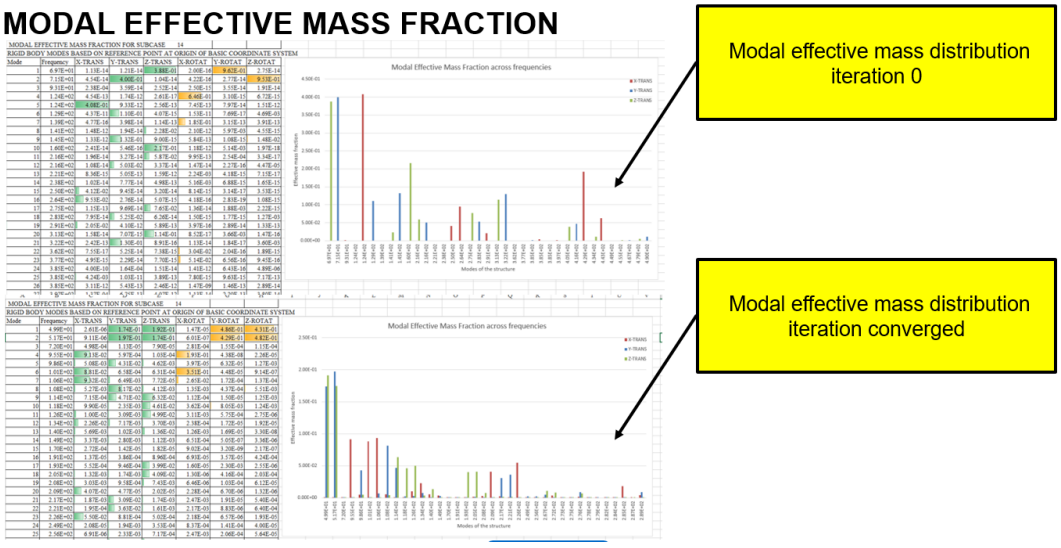

Figure 7.16: Model 2 solution 2 – modal effective mass fraction for the starting and converged iteration

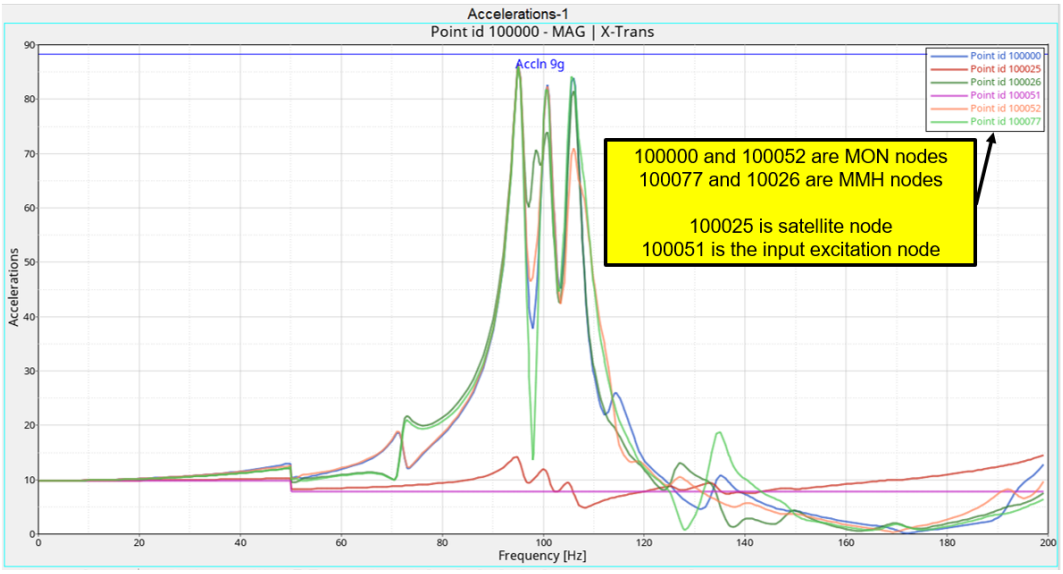

Figure 7.17: Model 2 solution 2 – dynamic analysis results for the converged iteration – X excitation

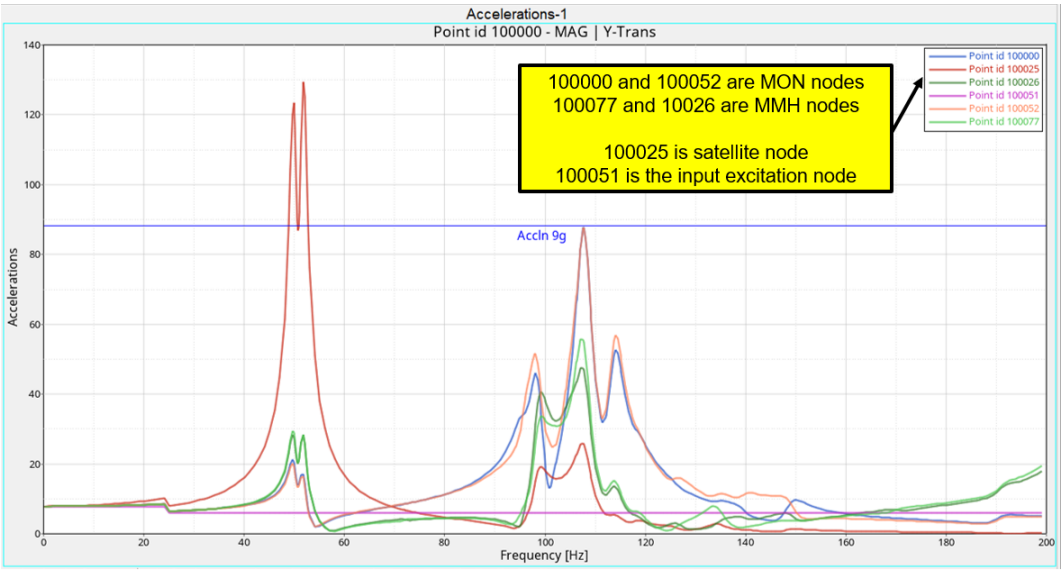

Figure 7.18: Model 2 solution 2 – dynamic analysis results for the converged iteration – Y excitation

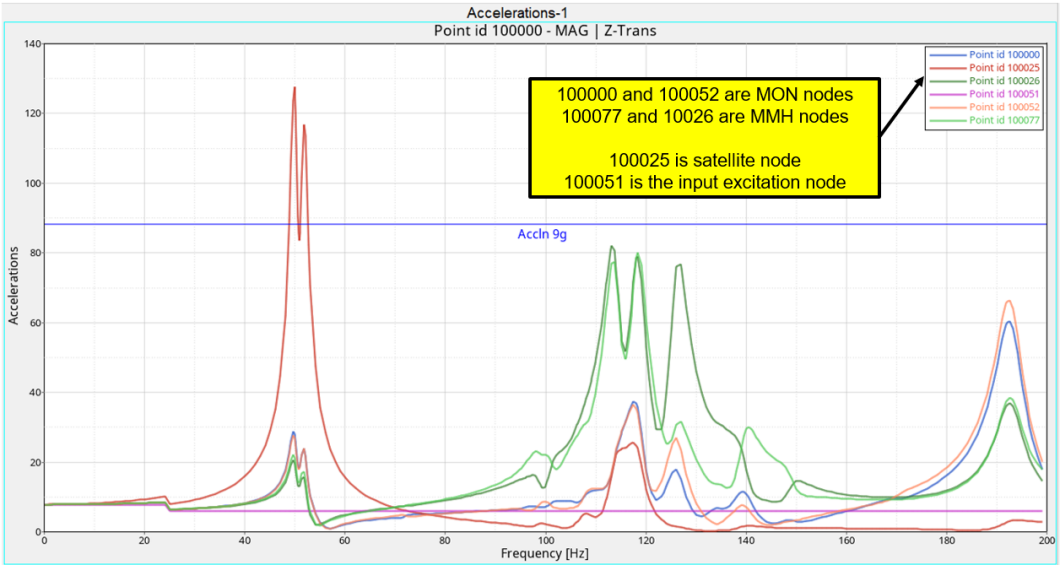

Figure 7.19: Model 2 solution 2 – dynamic analysis results for the converged iteration – Z excitation

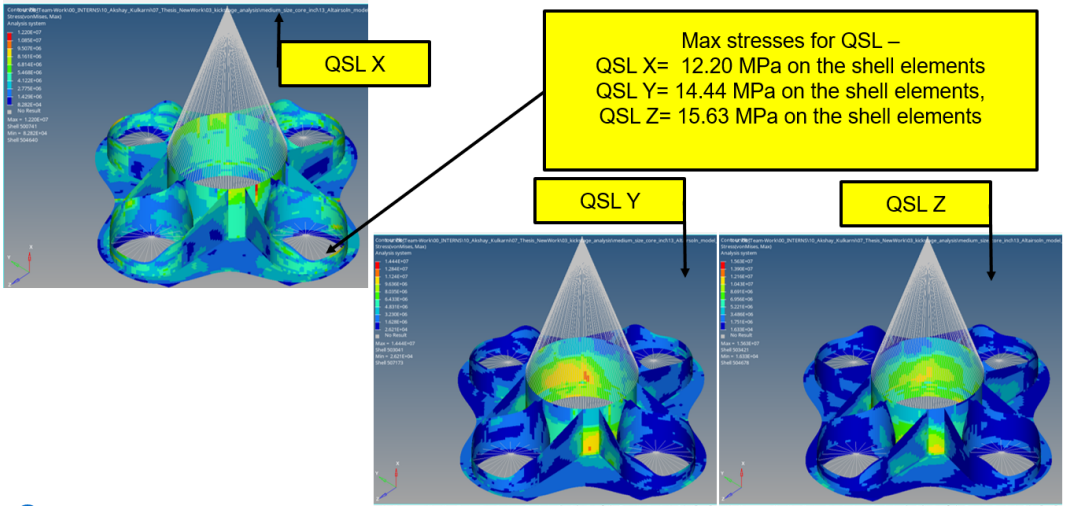

Figure 7.20: Model 2 solution 2 – quasi-static stresses results

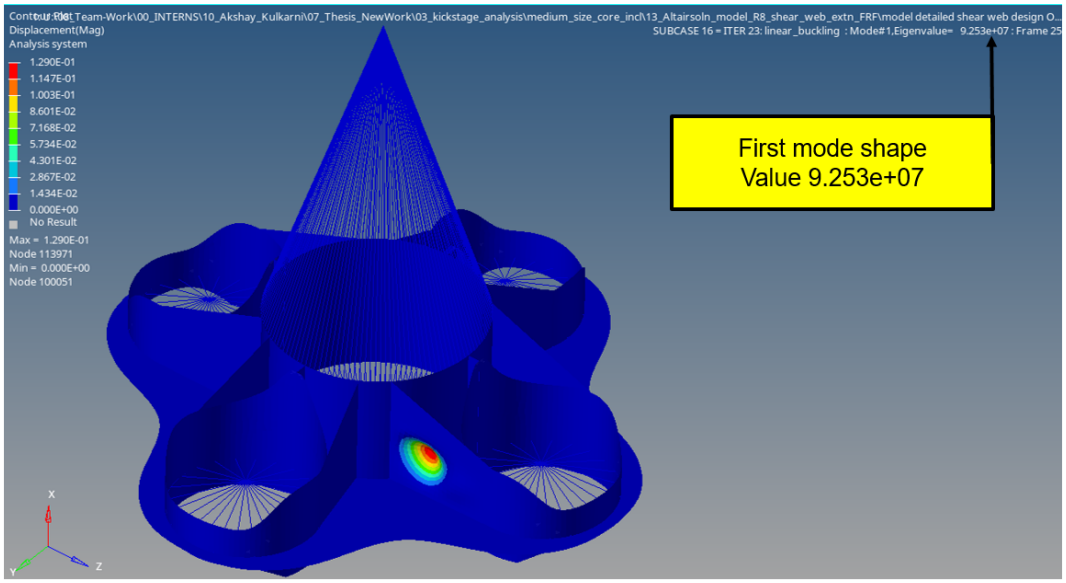

Figure 7.21: Model 2 solution 2 – first buckling mode results

7.4 Model 2 solution 3 – analysis including the frequency response function constraint with a reduced input excitation

Similar to the previous model, the values for the reduced input are assigned one-fifth of the sine input value.

7.4.1 Analysis evaluation

The optimization result leads to a structure with modified design parameters. The difference in the result for the first iteration and the final iteration for this configuration can be seen in Figure 7.22. The graph of the change of mass of the structure and the first modal frequency can be seen in Figure 7.23. For the sizing optimization result, the objective mass is minimized from a total of 6486.7kg to 341.88kg. This results in a frequency drop from 69.7Hz to 14.9Hz, which meets the requirement. Additionally, the thickness plot of the shell mesh is seen in Figure 7.24. The modal analysis results include the normalized displacement of the first three modes as seen in Figure 7.25 and the modal effective mass plot between the first and the final iteration is Figure 7.26. The difference of the mode shapes and the corresponding effective mass change can be seen here. The dynamic frequency response results are given for all nodes by Figure 7.27 for X direction excitation, Figure 7.28 for Y direction excitation, Figure 7.29 for Z direction excitation. For the node for reference node MON tank, the maximum peak acceleration is 5.44g at 20.0Hz which is within the qualification value of 9g. The quasi-static stresses are seen in Figure 7.30. It can be seen here that all the stresses are within the stress constraint limits and found safe. The buckling load for the structure is 2.4E6N and the mode shape is seen in Figure 7.31.

It can be seen that in the case of a mass minimization objective, the solution is driven by the frequency requirement, as the dynamic peak responses for all tanks are within the limits. In practicality, this is an extreme case, with the real case being somewhere in between case 2 and case 3. The solutions for such cases can be a combination of load inputs with some frequencies being notched to a low value of one-fifth and others being full level. This combination will depend on the other systems on the launcher and the sensitivity of the payload to certain frequencies.

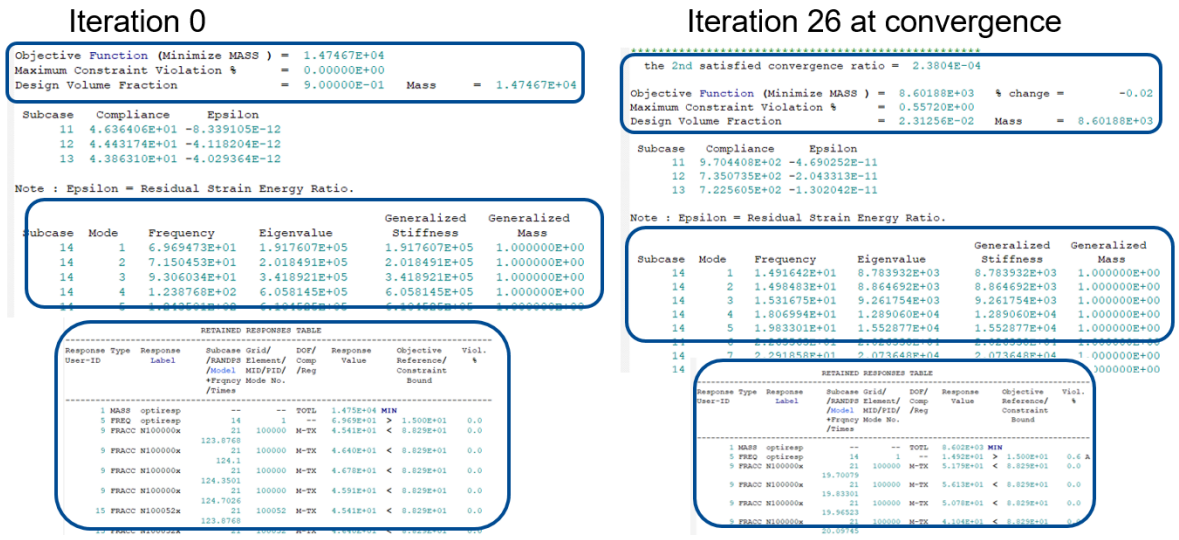

Figure 7.22: Model 2 solution 3 – iteration data comparison

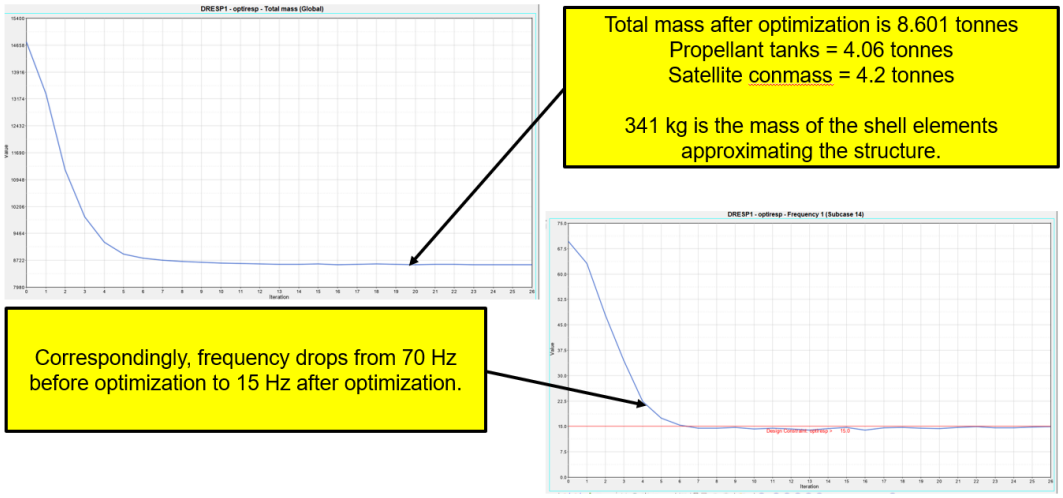

Figure 7.23: Model 2 solution 3 – mass and frequency data comparison

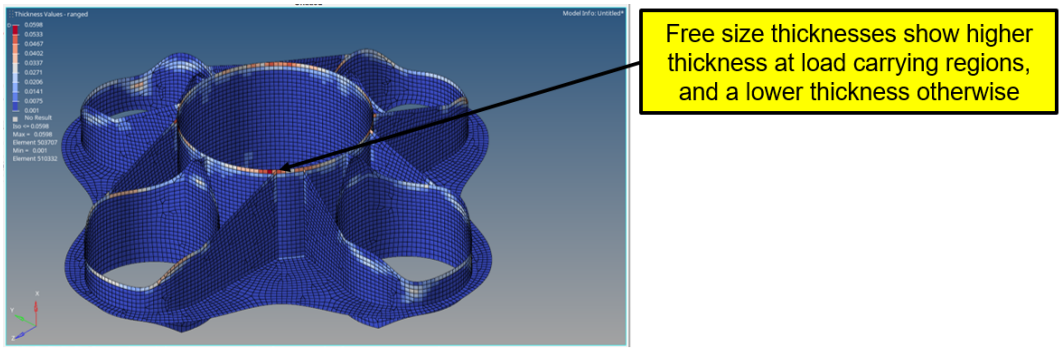

Figure 7.24: Model 2 solution 3 – mass distribution for the free size shell optimization

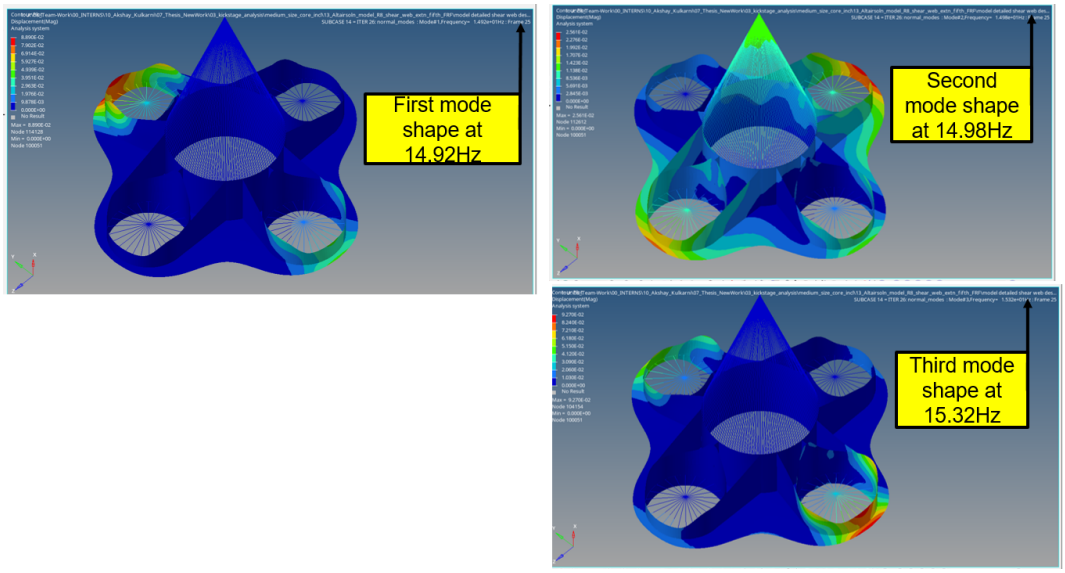

Figure 7.25: Model 2 solution 3 – modal analysis results for the converged iteration

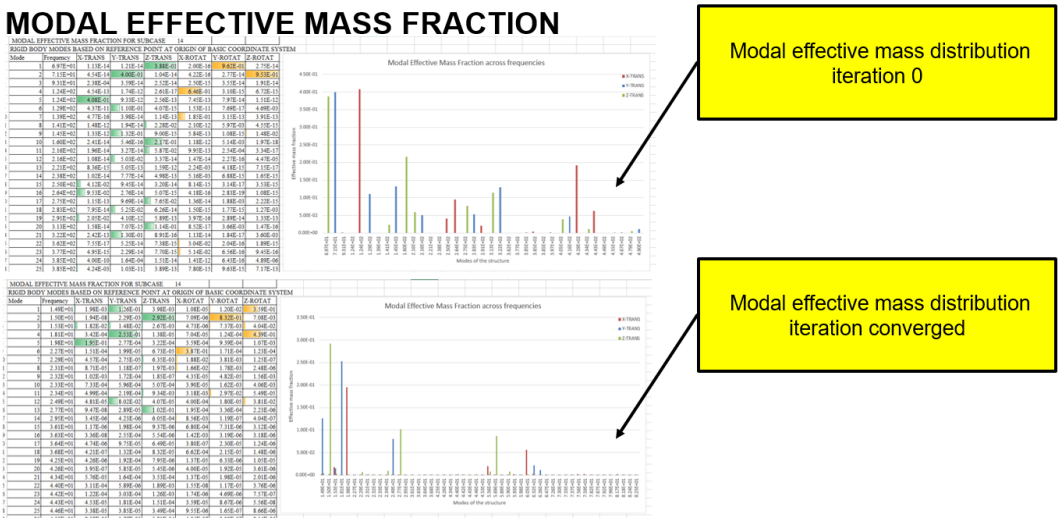

Figure 7.26: Model 2 solution 3 – modal effective mass fraction for the starting and converged iteration

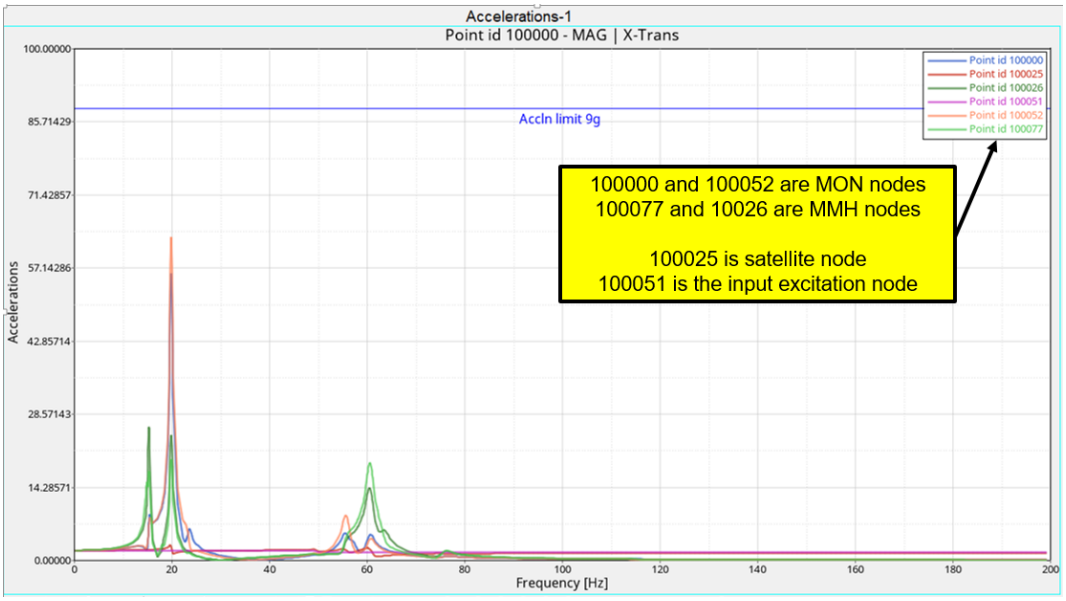

Figure 7.27: Model 2 solution 3 – dynamic analysis results for the converged iteration – X excitation

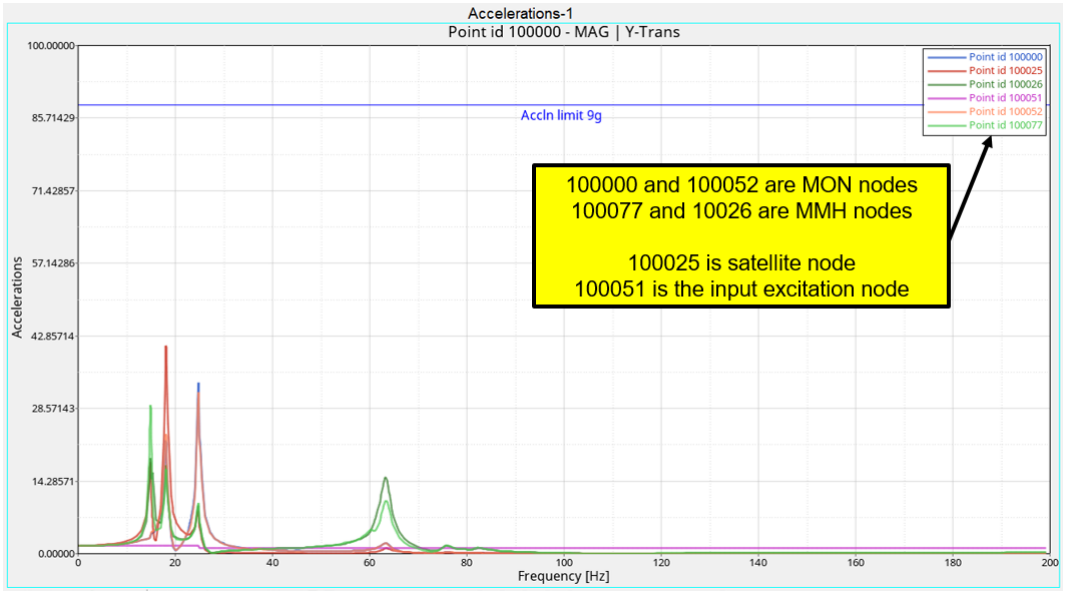

Figure 7.28: Model 2 solution 3 – dynamic analysis results for the converged iteration – Y excitation

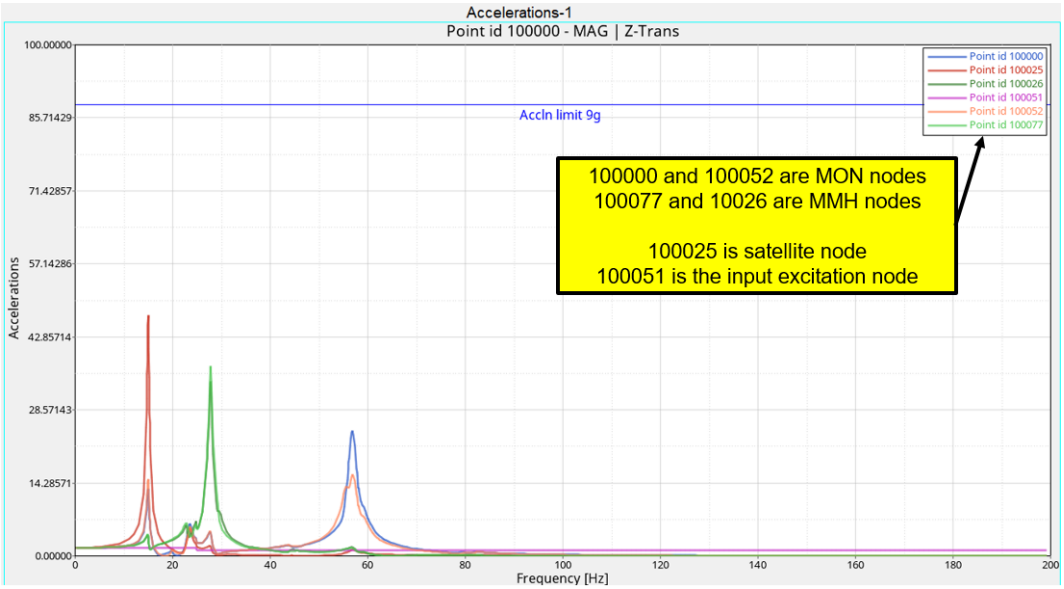

Figure 7.29: Model 2 solution 3 – dynamic analysis results for the converged iteration – Z excitation

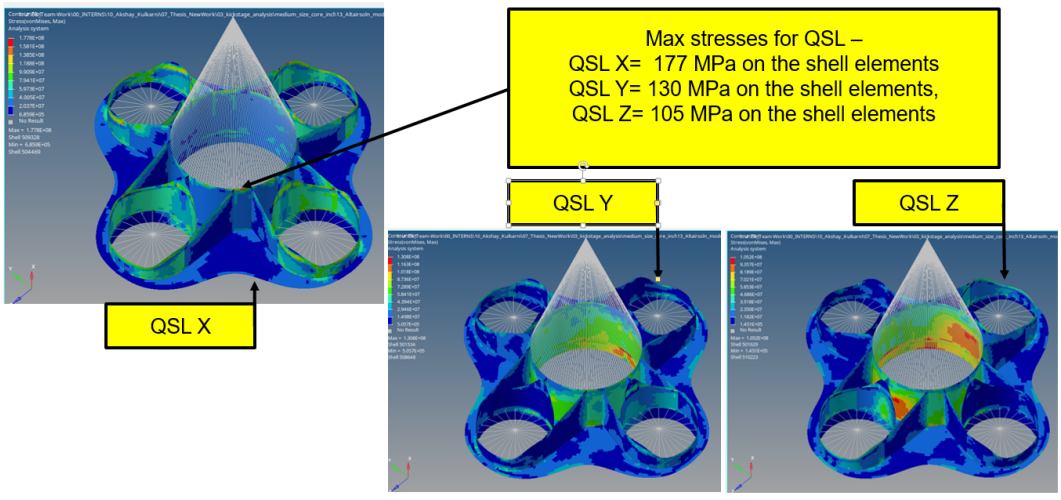

Figure 7.30: Model 2 solution 3 – quasi-static stresses results

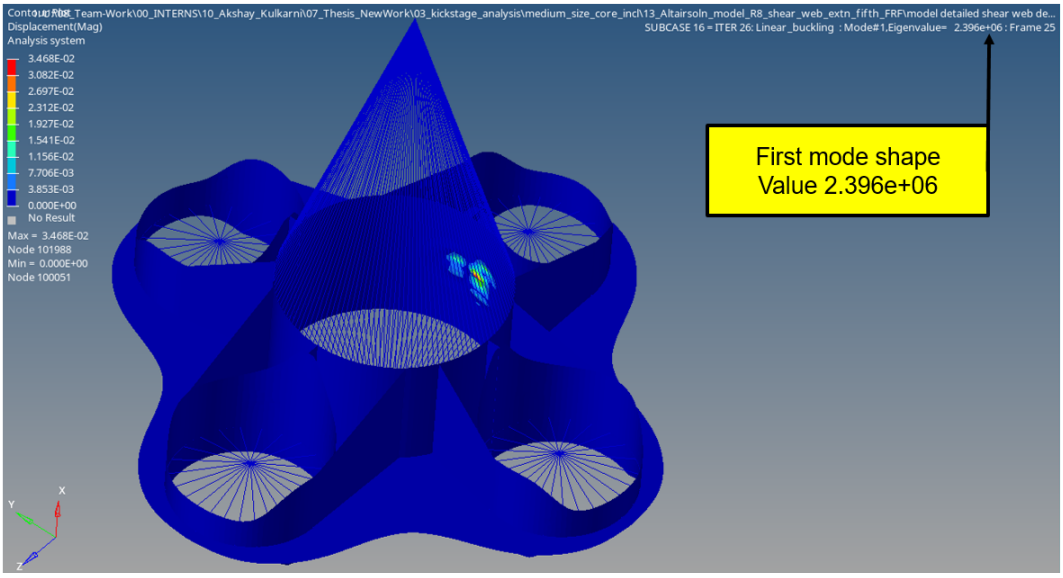

Figure 7.31: Model 2 solution 3 – first buckling mode results

7.5 Model 2 results discussion

The comparison of the results for Model 2 can be seen in Table 7.1. It can be seen that the first case of the topology-optimized result has the highest mass but also has a higher peak response for the propellant tank. Similar to model 1, The best-case scenario of meeting the peak loading requirement is realized by solution 2, however, the mass budget is also high. It is interesting that the regions of mass distribution change significantly in Solution 2 and the modal effective mass distribution table also changes between the first and last iteration. This solution also provides a higher buckling load. This indicates that while it would be useful to implement this solution to some frequency intervals, the higher mass budget due to it, would not be acceptable. Solution 3 has a reduced input so it is valid that all the responses are within the peak response values. In practicality, a notching request cannot be possible for the entire spectrum. Hence, a good design can include these design methodology implications from Solution 2 and Solution 3 combined. It can also be seen that the stresses in all three solutions are within limits. Thus here as well, the sizing optimization is driven primarily by the dynamic behavior of the structure and the size modification can be useful to assist in some frequency intervals, while being ignored at other intervals.

Model 2 - with shear web support elements				
	Baseline 0th Iteration	Solution 1 - after optimization	Solution 2 - after optimization	Solution 3 - after optimization
Description- for the result	Baseline 0th Iteration	Dynamic sine without optimization	Dynamic sine with optimization	one fifth Dynamic sine with optimization
Structural mass (in kg) - excluding conm2	6486.70	450.22	2977.40	341.88
First frequency mode (in Hz)	69.7	15.0	49.9	14.9
Peak Dynamic response for MON node 100 000 (in g)	23.65	21.92	9.00	5.44
Excitation direction	X	X	X	X
Above Peak dynamic response is at frequency (in Hz)	124.10	17.00	90.00	20.00
First buckling mode value (in N)	1.29E+09	3.22E+06	9.25E+07	2.40E+06

Table 7.1: Summary table of the Model 2 sizing optimization analysis

The mass distribution of different 2D elements after optimization can be seen in Table 7.2. It can be seen here that the central core has about 30% mass budget of the total structure. The circular panels along the propellant tanks get more stiffened for the case with full load base input excitation, indicating that the mass redistribution occurs in this region to affect the modal and dynamic behaviour of the structure.

Model 2 - with shear web support elements				
Mass distribution of size optimized results		Solution 1 - after optimization	Solution 2 - after optimization	Solution 3 - after optimization
Mass distribution	Result description	Dynamic sine without optimization	Dynamic sine with optimization	one fifth Dynamic sine with optimization
Central core	absolute (in kg)	112.54	886.94	96.00
	fraction (in %)	25.00%	29.79%	28.08%
Circular panels around the propellant tanks	absolute (in kg)	157.00	1220.00	101.00
	fraction (in %)	34.87%	40.98%	29.54%
Bottom flat panel and side shear webs	absolute (in kg)	178.00	806.00	144.00
	fraction (in %)	39.54%	27.07%	42.12%

Table 7.2: Mass distribution summary table of the Model 2 sizing optimization analysis

7.6 Discussion for sizing optimization

Based on the two sizing optimization analyses and results discussed, the following can be concluded. Higher mass savings are possible in the bar-based model, however, more stability for dynamics and buckling is present in the shear web-based model. Some regions of the cylinder close to the propellant tanks with a very thin thickness can be seen as redundant due to the presence of the surrounding shear panels. The buckling load in some solutions leads to the side panels being buckled instead of the central cylinder. In addition, the cylindrical mesh has a buckling mode shape at the more heavily loaded regions, near the interface with propellant tanks. Thus, additional stiffening is present in the area. The sizing optimization algorithm has rightfully provided regions where high thickness could be added, to influence the dynamic behavior. This limits the peak response of the propellant tank, typically seen in solution 2 of both designs. This is a very useful feature to avoid coupling of propellant tanks, which could result in very high loads for a case of resonance.

Chapter 8

Composite Design and Modelling

The previous chapters focused on building the model based on topology optimization and sizing optimization in a step-wise manner. This chapter discusses the innovative design of anisogrid composite structure for the central core of the rocket. The advantages of such a design are discussed in the literature study subsection 3.1.3, making this design proposal one of the direct outcomes of the literature study. The technical implementation content here discusses the analytical design equations followed by a preliminary design proposal for the kick stage central core loading conditions. Finally, this design has been verified in FEM using a simplified model and optimized to meet the dynamic requirements.

8.1 Composite design analytical model proposal for central core design

There are three main design methods considered for anisogrid design [34].

1. Geometric Programming methods
2. Minimization of safety factors corresponding to possible failure modes
3. Numerical method.

In this chapter for implementation of anisogrid design for the kick stage central core, the second and third methods are used. Firstly, a model is developed using the analytical equations and relations provided for the design methodology. This model is then modeled in FEM using a simplified version, and further modified using a sizing optimization method.

8.1.1 Failure modes for an anisogrid structure

There are three possible failure modes for an anisogrid structure, and they are listed below. Correspondingly, there are three factors of safety each associated with a particular failure mode.

1. Global buckling of the shell n_g
2. Local buckling of the helical rib segments between the triangular meshes n_l
3. Fracture failure of the helical ribs under compressive loads, i.e. strength failure n_s

The minimization of these safety factors will provide the dimensions of the structure to be designed.

8.1.2 Analytical equations applied to kick stage structure dimensions

The dimensions of the anisogrid composite cylindrical structure are mentioned in Figure 8.1. The angle made by the helical ribs with the vertical axis is 2φ, the geometrical separation between the circumferential ribs is a_c and the geometrical separation between the helical ribs is a_h. The width of the helical ribs is given by δ_h and that of the circumferential ribs is given by δ_c. The thickness of the ribs is then assumed to be perpendicular to the plane and given by h [34][33].

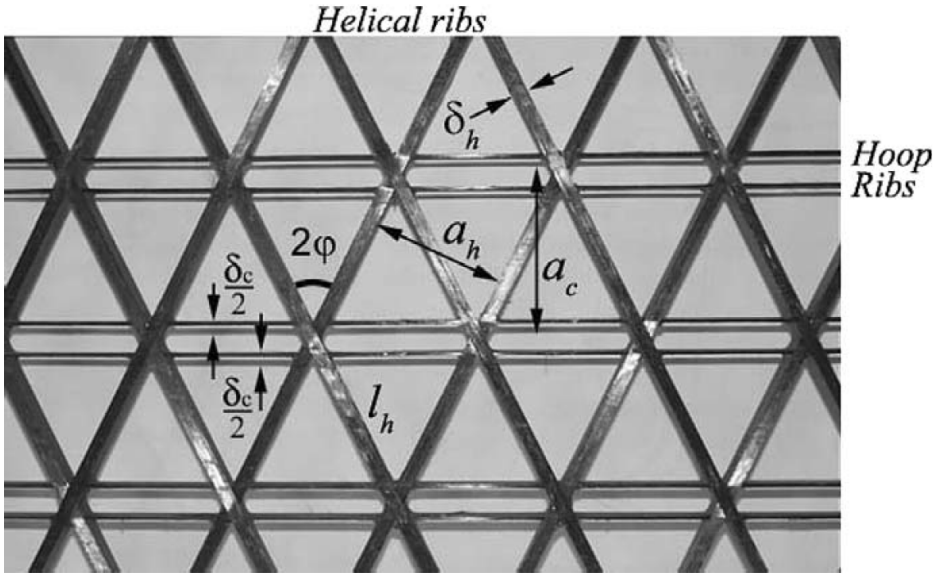

Figure 8.1: Variables governing the anisogrid design [34]

The detailed derivation of the governing equations is beyond the scope of this document. However, the equations and the citations are provided separately in Appendix C.

The relation between the scaling factors of the geometry to the safety factors is then written as:

$$\bar{\delta}_h = \frac{\delta_h}{a_h}, \bar{\delta}_c = \frac{\delta_c}{a_c},$$

These factors are then step-wise calculated as follows. An axial compressive force F and a bending moment M acting on the cylindrical shell result in an equivalent axial compressive

force F is given in Equation 8.1, where D is the diameter of the shell and in the case of the kick stage is $D = 1.666$m.

$$P = F + \frac{4M}{D} \tag{8.1}$$

For the compressive loads on the kick stage, a higher margin of safety is considered on the forces acting on it. As discussed in earlier chapters, the design is being carried out for the peak qualification of propellant tanks, the same being 9g. Correspondingly, the payload of 4.2t, the combination of four propellant tanks equating to 4058kg acting as a bending load, and an additional approximate 440kg mass for the support structures are considered. The bending moment equivalent of the term is 1.2929E6N. The axial load term is 2.086E6N. The total equivalent force of $P = 2.086$E6N is then considered as the loading parameter for which the structure is to be designed.

The buckling loading parameter p for this structure would then be given by Equation 8.2, resulting in a value of $p = 0.9569$MPa.

$$p = \frac{4P}{\pi D^2} \tag{8.2}$$

The buckling critical condition for comparatively lower loads is the case in which the equivalent buckling loading parameter p is less than the buckling critical parameter of the structure p_s. This is given by Equation 8.3, where E is the rib modulus, $\bar{\sigma}$ is the compressive rib strength, k is the local buckling factor in the Euler condition.

$$p \leqslant p_s = \frac{48\bar{\sigma}^2}{\pi E}\sqrt{\frac{\bar{\sigma}}{kE}} \tag{8.3}$$

For circumferential ribs being closer to the intersection nodes of the helical ribs, $k = 1.15$ is a good approximation [34]. For the coarse design proposal, the material properties of a CFRP rib structure can be considered in this case, with $E = 90$GPa and $\bar{\sigma} = 650$MPa, the buckling loading parameter $p_s = 5.68M$Pa[34].

Since this meets the inequality in the above equation, this is a buckling active condition of loading on the grid structure.

The strength safety factor is then given by Equation 8.4, and to meet the failure limit, should have satisfied the inequality greater than one.

$$n_s = 4\bar{\sigma}\left(\frac{9}{4\pi^2 p^2 k E^3}\right)^{1/5} > 1 \tag{8.4}$$

Substituting the numbers, the result is $n_s = 1.9832$ that is satisfying the inequality, indicating a positive safety factor.

The geometric parameters of the anisogrid structure are then calculated. The thickness of the ribs is given by Equation 8.5 and after substituting the values, results in a thickness of $t = 10.21$mm.

$$h = \frac{D}{4}\left(\frac{48\pi^4}{E^4}k^2 p^4\right)^{1/10} \tag{8.5}$$

The inclination angle of the helical ribs is given by Equation 8.6 and after substituting the values, results in an angle of $\varphi = 26.565\,\text{deg}$.

$$\tan\varphi = \frac{1}{2} \tag{8.6}$$

The values for the rib fractions are given by Equation 8.7 and Equation 8.8.

$$\bar{\delta}_h = \frac{5}{4\pi}\left(\frac{108\pi^2 p^2}{E^2 k^4}\right)^{1/10} \tag{8.7}$$

$$\bar{\delta}_c = \frac{\bar{\delta}_h}{2} \tag{8.8}$$

These result to a helical rib width fraction of $\bar{\delta}_h = 0.07648$, and a circumferential rib width fraction of $\bar{\delta}_c = 0.03824$.

The mass total for the structure is given by Equation 8.9, where ρ is the density of the material.

$$m = \pi DLh\rho\left(2\bar{\delta}_h + \bar{\delta}_c\right) \tag{8.9}$$

In this case ρ =1450 kg/m^3, and substituting for the cylinder with diameter $D = 1.666$m and a length of $L = 1.12$m, we get a mass of $m = 16.59$kg. This can also be written as mass per unit area of the shell cylinder given by $\bar{m} = m/(piDL)$ =2.83 kg/m^2.

This mass is equivalent to the same mass of an aluminium sheet with about 1mm thickness. The buckling load for this sheet as per the buckling equation Equation 4.4 is given by $P_{Al} = 3.004$E5N. However, due to the presence of imperfections with the knockdown factorEquation 4.5, the buckling load is further reduced by the knockdown of $KDF = 24\%$, resulting in a small value of $P_{KDF} = 7.405$E4N. Thus, in comparison to an aluminium shell, the critical buckling load of a composite anisogrid shell $P_{composite} = 2.086$E6N are substantially higher.

The geometric dimensions of the spacing and the widths are given by the earlier-mentioned formulae. The number of ribs dictates the geometric separation for a given diameter, and this in turn will dictate the widths of the helical and circumferential ribs. A large number of ribs will decrease the geometric spacing and so will also decrease the width of the structure. This will bring with it another set of manufacturing difficulties.

Based on considering iterations and calculating the geometric spacing and widths for a large number of ribs, the total number of ribs is chosen as 40. The iterations for rib sizing and geometric spacing are shown in Appendix D. The circumferential separation along the curve of the rib intersection points is then given by the simple geometric equation as $a = \pi D/40 =$ 0.1308m= 13.08cm.

This leads to a helical rib normal separation of $a_h = acos\phi = 0.117$m= 117mm and the circumferential ribs separation of $a_c = a/(2tan\phi) = 0.1308$m= 130.8mm. The width of the helical ribs is given by $\delta_h = 8.951$mm and that of the circumferential ribs is given by $\delta_c = 5.004$mm.

These are analytical values for the given combination of parameters and they are considered the baseline design for the next step of FEM verification.

8.2 Preliminary composite design proposal in FEM

The FEM modeling of the anisogrid shell cylinder has been carried out in the literature. The first level model is only a cylindrical shell composed of 1D elements as seen in a work by Belardi et al. [7].

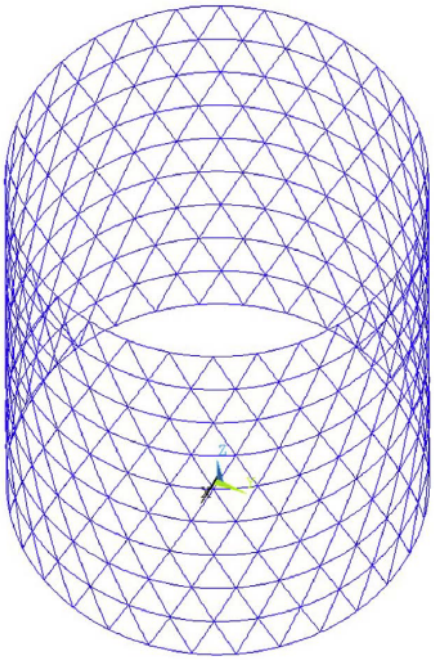

Figure 8.2: 1D element based model of the design [7]

Based on this reference, a simple model is first proposed using these analytical values. An analysis is completed with the given parameters, and then optimization is carried out as per similar boundary conditions.

8.2.1 Model description of the design proposal

The model formulated above is checked in the Hypermesh FEM solver. The complete FE modeling of the kick stage in a composite grid structure would not be practically feasible given the complexity of the surrounding structures and the scope of this project. This also serves as a comparison for the numerical method to validate the analytical design calculations. The first step is to verify the results of the analytical model. The second step is to optimize these results for constraints that are not met by the analytical model dimensions.

The spacecraft payload is modeled as a point mass with CONM2 properties. The fixed boundary condition is assigned to all the nodes on the inner surface of the central hollow

tube. This represents the central core that connects the upper stage to the payload and houses all the kick stage components. The input mesh view along with the modeling method can be seen in Figure 8.3.

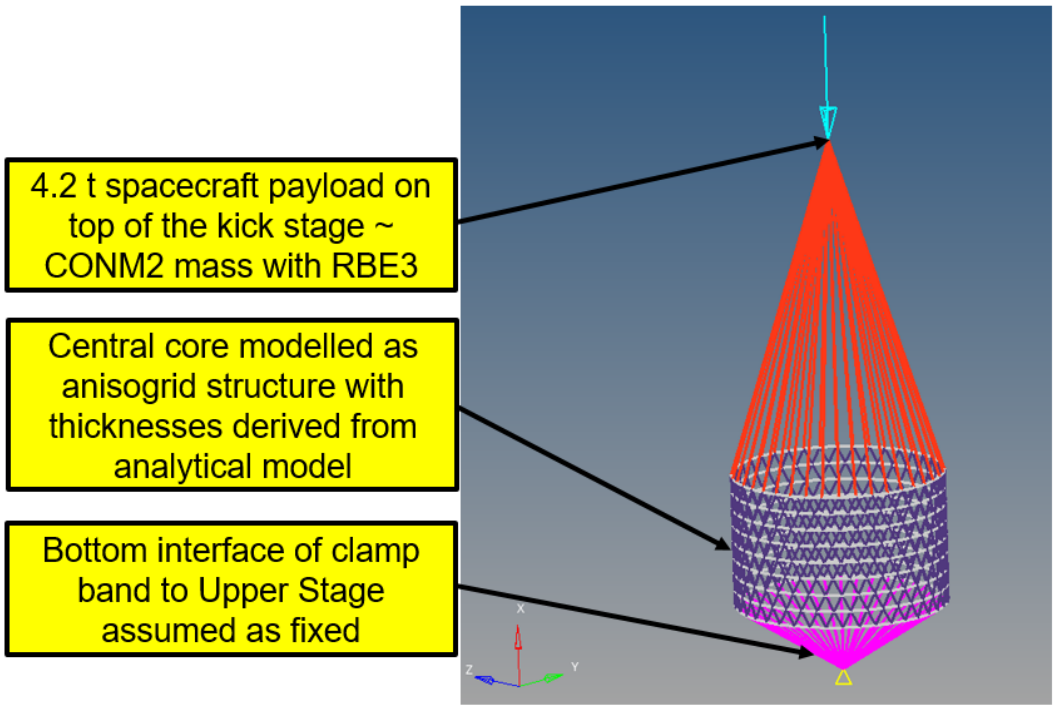

Figure 8.3: Composite model design proposal baseline – input mesh

The CBAR type elements are used to model the 1D bar elements in this mesh. This is not a very accurate modeling of a composite structure. This is because the property assignment for CBAR, the PBAR property allows only for MAT1 isotropic elastic material properties. So as in this case, the matrix contribution is assumed negligible, and only the fiber is assumed to contribute to the rib strength and stiffness. Thus for this simplified model, the numbers discussed earlier E, σ, ρ are assumed. Additionally, this way of modeling has certain advantages such as quick estimation of results and easier sizing optimization scope. The first iteration point of the analysis is the width and geometric dimensions obtained in the analytical model proposal.

The following constraints are also applied for the sizing optimization analysis.

- **Frequency constraint (lower bound)** – For optimization, the design requires a minimum of 15Hz as the first frequency requirement. Hence there is a lower bound constraint on the frequency response.
- **Design objective** – The design objective is the minimization of the mass of the structure.
- **Design Variables** – The design variables are a range of lower-end to upper-end values on the design responses for the thickness of the anisogrid and the widths of the helical and circumferential ribs.

- **Load cases** – The QSL load cases are considered for the linear static load cases and compliance evaluation, with 9g for the longitudinal and 5g for the lateral accelerations. The modal load case for the first frequency calculation is provided as well. The first frequency is calculated as an eigenvalue problem as described in the earlier sections. The fixed boundary conditions are representing the interface of the kick stage to the upper stage. The buckling load case is assigned to calculate the buckling modes.
- **Responses** – The design evaluation and responses are recorded by the DRESP cards for variables such as mass, frequency, and first buckling value. Some of these response cards are written back to the constraint card for the optimization loop to complete and meet the constraint requirements, while others are for monitoring the solution.

8.2.2 FEM results corresponding to the analytical solution

The baseline model is designed without the vertical ribs to approximate the analytical model and can be seen in Figure 8.3. The modal analysis deformation results of the first three modes as seen in Figure 8.4. The first two modes 7.29Hz are the lateral movements along Y and Z primarily driven by the payload point mass. The third mode is at a higher value of 48.38Hz and is the main mode of the shell cylinder and is radially outward. The quasi-static stresses are seen in Figure 8.5, indicating that for the input load, the axial stresses are within the tensile strength of the composite $\bar{\sigma} = 650\text{MPa}$. The buckling load for the structure is 1.414E6N and the mode shape is seen in Figure 8.6. This is lower than the value in the analytical buckling load predicted as $P = 2.086E + 6\text{N}$.

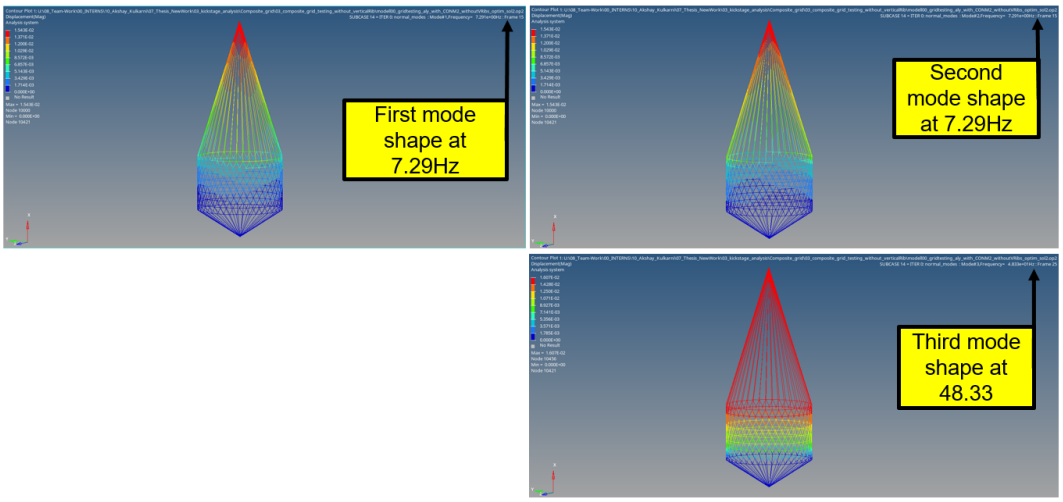

Figure 8.4: Coarse composite design FEM baseline – mode shapes and frequencies

8.2.3 Sizing optimization of the initial model and results

The purely analytical structure does not meet the requirements of the main structure, so an optimization process is carried out. The optimization input mesh view can be seen in Figure 8.7. Additional four vertical stiffeners are added along the sides, encircled in the image,

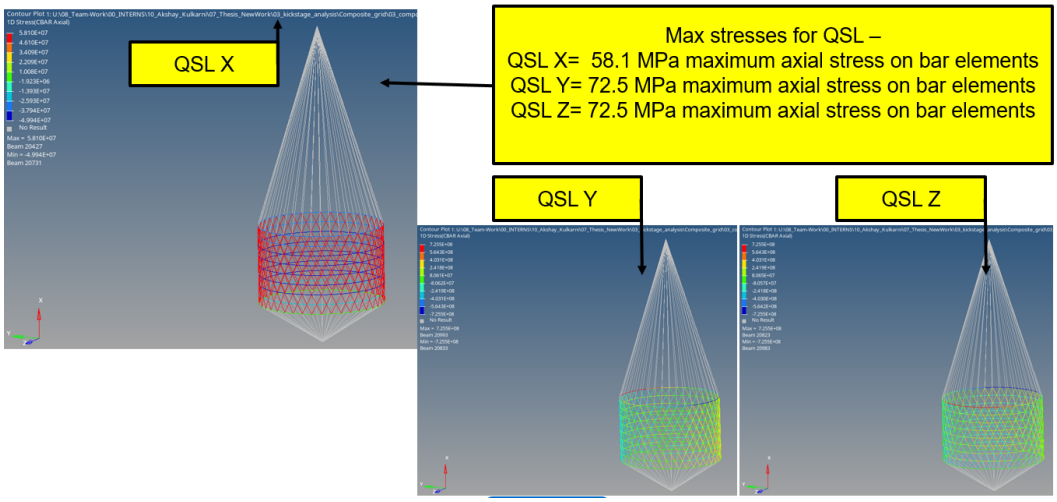

Figure 8.5: Coarse composite design FEM baseline – quasi-static stresses

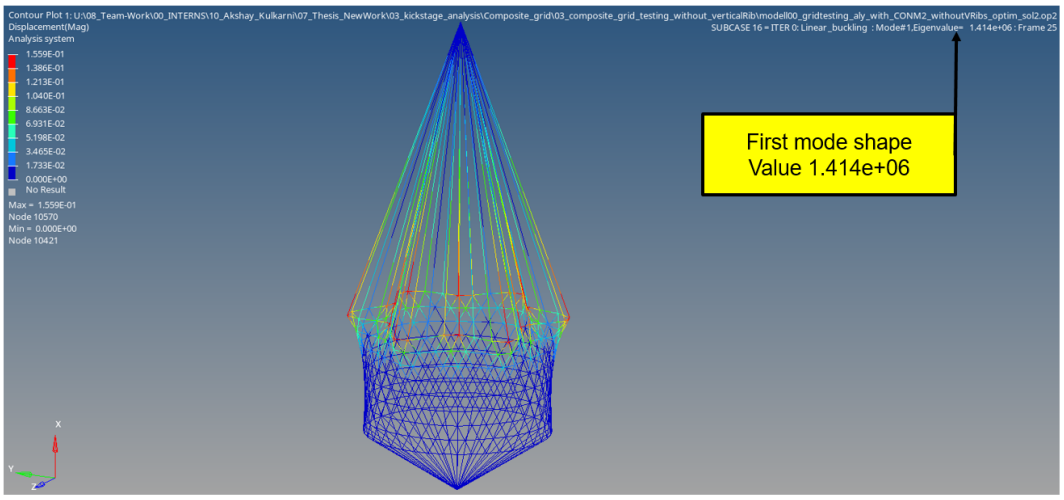

Figure 8.6: Coarse composite design FEM baseline – first buckling mode

to act as joining and stiffening ribs for the propellant tank connections. This conclusion to add vertical stiffeners is derived from the literature study section 3.1.3 and the analytical modeling results of the previous section.

The sizing optimization is carried out, with stress and frequency constraints, so that the frequency constraints of 15Hz are met by the final design.

Sizing optimization results

The difference in the result for the first iteration and the final iteration for this configuration can be seen in Figure 8.8. For the sizing optimization of the composite anisogrid result, the objective mass actually increases from a total of 16.20kg to 63.55kg. The converged result happens to meet the constraint on the frequency requirement as the initial model with the first mode at 7.4Hz does not meet the requirement. This leads to a first mode value of 15.0Hz,

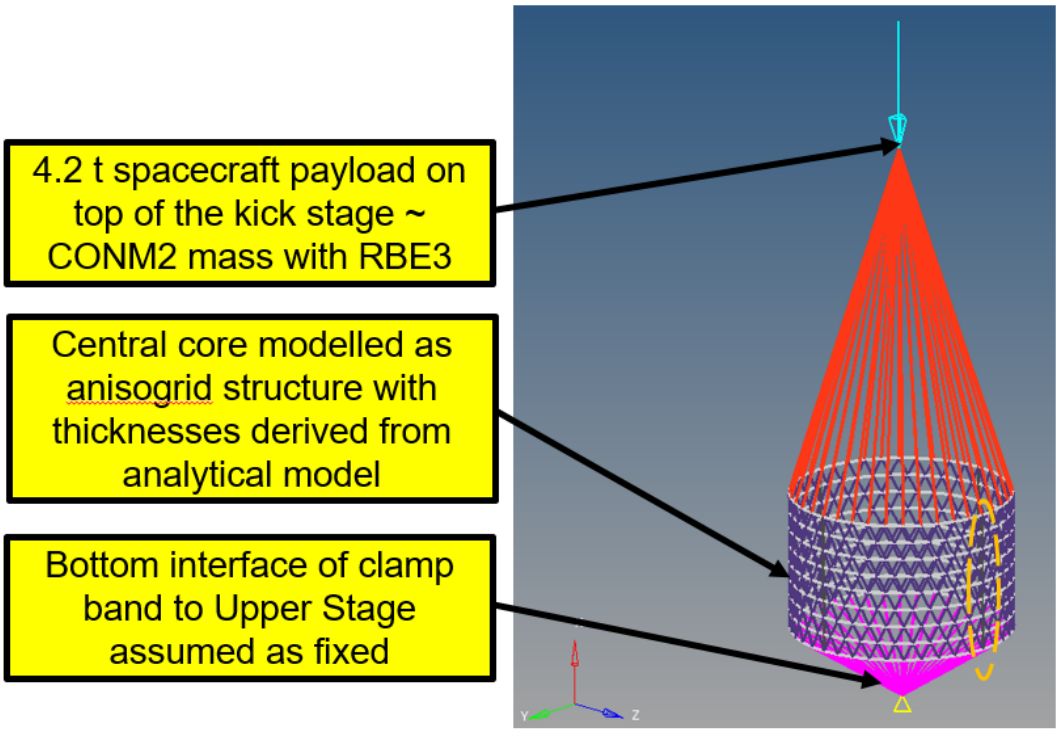

Figure 8.7: Composite model design proposal – input mesh

which meets the optimization constraint. The thickness parameters increase, resulting in, the helical rib width as $\delta_{hFE} = 10.77$mm, the circumferential rib width as $\delta_{cFE} = 6.13$mm, and the thickness as $h_{FE} = 33.14$mm. A higher percentage increase is seen in the thickness parameter as compared to the width parameters, validating the principle that the bending stiffness is proportional to the cube of the thickness. The modal analysis results include the normalized displacement of the first three modes as seen in Figure 8.9. The first two modes 15Hz are the lateral movements along Y and Z primarily driven by the payload point mass. The third mode is at a higher value of 98.69Hz and is the main mode of the shell cylinder and is radially outward. The region that is not vertically stiffened contributes more to the relative modal displacement, indicating higher mass participation of the regions not vertically stiffened. Thus, if the design requires, additional stiffness desired along the axial direction can be achieved by the addition of more vertically stiffened ribs.

The quasi-static stresses are seen in Figure 8.10. It can be seen here that the axial stresses are within the stress constraint limits and found safe. Figure 8.11 shows the stresses on the grid structure when subjected to a compressive quasi-static load of 9g. As discussed earlier, the helical ribs and the vertical ribs experience compressive stresses, however, at the same time, the circumferential ribs experience tensile stresses. This leads to the self-stabilization behavior, as it is preferred that the composite ribs be loaded in tension. This enhances the ability of the structure to perform against compressive loading and increases the buckling performance, particularly given the compressive load due to payload. The buckling load for the structure has increased from 1.12E6N to 1.39E7N a nearly ten-fold increase and the mode shape is seen in Figure 8.12. It can be seen that in the case of a mass minimization objective, the solution is driven by the frequency requirement. This on the contrary leads to an increase

in the mass of the structure.

Iteration 0

```
Objective Function (Minimize MASS ) =  4.21620E+03
Maximum Constraint Violation %      =  0.50208E+02
Volume                              =  1.11710E-02   Mass     =  4.21620E+03
```

Subcase	Compliance	Epsilon
11	1.678173E+02	-2.133948E-14
12	2.296719E+03	-4.712369E-14
13	2.296648E+03	-4.910518E-14
15	1.215792E-09	-1.871000E-14

Note : Epsilon = Residual Strain Energy Ratio.

Subcase	Mode	Buckling Eigenvalue
16	1	1.467739E+06
16	2	1.479257E+06
16	3	1.485770E+06
16	4	1.486696E+06
16	5	1.530673E+06

Subcase	Mode	Frequency	Eigenvalue	Generalized Stiffness	Generalized Mass
14	1	7.468740E+00	2.202188E+03	2.202188E+03	1.000000E+00
14	2	7.468855E+00	2.202256E+03	2.202256E+03	1.000000E+00
14	3	4.974612E+01	9.769630E+04	9.769630E+04	1.000000E+00
14	4	1.028430E+02	4.175504E+05	4.175504E+05	1.000000E+00
14	5	1.029405E+02	4.183424E+05	4.183424E+05	1.000000E+00

Iteration 9 at convergence

```
ITERATION   9
  the 2nd satisfied convergence ratio =  6.2073E-04

Objective Function (Minimize MASS ) =  4.26355E+03   % change =       -0.06
Maximum Constraint Violation %      =  0.00000E+00
Volume                              =  4.38272E-02   Mass     =  4.26355E+03
```

Subcase	Compliance	Epsilon
11	4.289026E+01	-1.921717E-14
12	5.701438E+02	-5.543328E-14
13	5.701520E+02	-5.623007E-14
15	3.073088E-10	-1.985123E-14

Note : Epsilon = Residual Strain Energy Ratio.

Subcase	Mode	Buckling Eigenvalue
16	1	1.393773E+07
16	2	1.420554E+07
16	3	1.556816E+07
16	4	1.559924E+07
16	5	1.629631E+07

Subcase	Mode	Frequency	Eigenvalue	Generalized Stiffness	Generalized Mass
14	1	1.501363E+01	8.898789E+03	8.898789E+03	1.000000E+00
14	2	1.501373E+01	8.898918E+03	8.898918E+03	1.000000E+00
14	3	9.868770E+01	3.844907E+05	3.844907E+05	1.000000E+00
14	4	1.754291E+02	1.214963E+06	1.214963E+06	1.000000E+00
14	5	1.755355E+02	1.216438E+06	1.216438E+06	1.000000E+00

Figure 8.8: Coarse composite design FEM – comparison of first and converged iteration

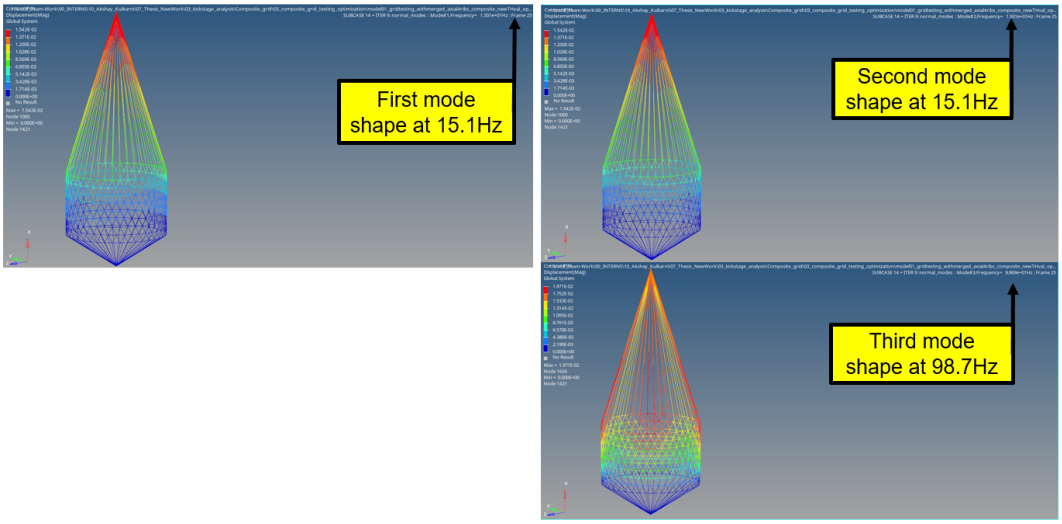

Figure 8.9: Coarse composite design FEM – mode shapes and frequencies

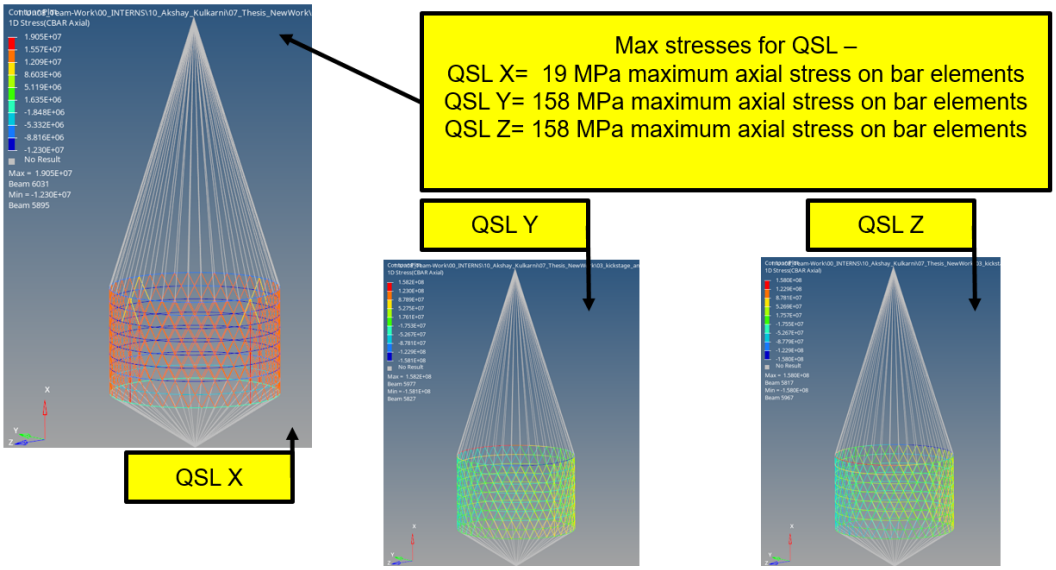

Figure 8.10: Coarse composite design FEM – quasi-static stresses

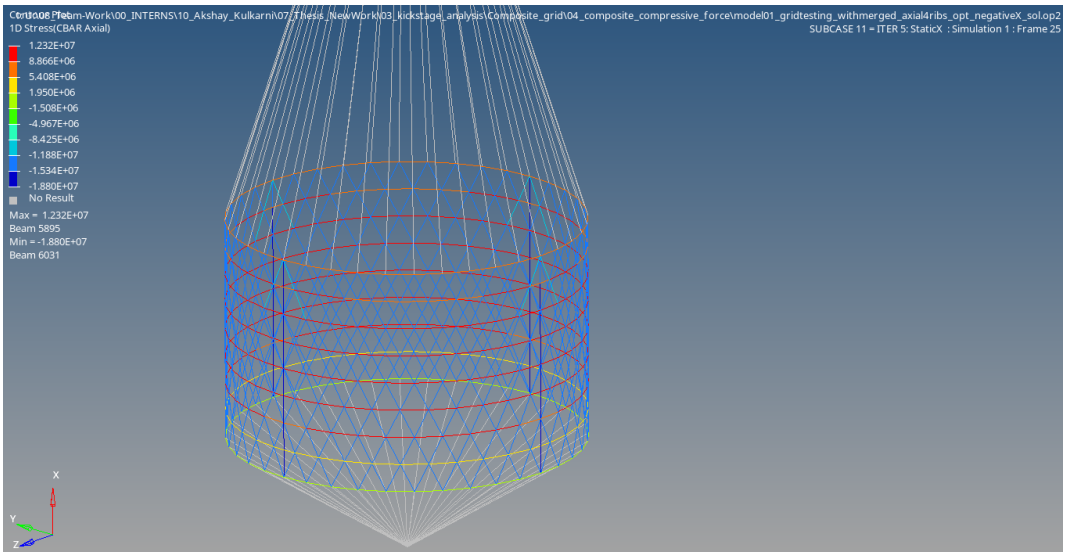

Figure 8.11: Coarse composite design FEM – axial stresses due to compressive loads

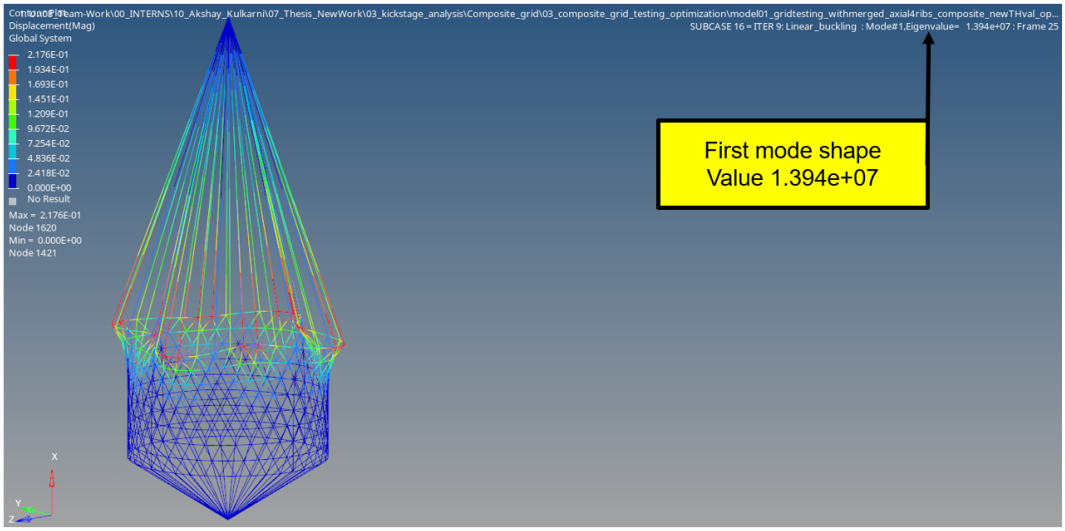

Figure 8.12: Coarse composite design FEM – first buckling mode

8.3 Optimization summary results

The results for the composite design are summarized in Table 8.1. The analytical result and the first iteration result of the FEM are nearly identical results with only 1kg mass difference and the same order of magnitude buckling value.

For the two FEM models, the mass actually increases from the first iteration to the last iteration, and this is because the modal frequency requirement is not being met. The mass increases by about four times as compared to the analytical modeling. This is attributed to the modal frequency requirement to be fulfilled in the design. Additionally, buckling behavior also improves. The value here is higher than the design value of the analytical model as well. This shows that the central core design with anisogrid structures is a promising design for the kick stage.

The analytical model design thus seems to be a very preliminary design approach and needs to be modified to meet the structural analysis requirements of particularly dynamics. The mass fraction of the central core is approximately 30% of the total mass of the structure as shown in the previous studies on sizing optimization. If we assume the same relation holds true, the total mass for the anisogrid structure results to only 211kg. The model as compared to an aluminium central core has a better performance. This is a significant reduction compared to the values in the aluminium design. Of course, a detailed analysis of the propellant tanks needs to be carried out and validate this prediction. The mass here for the anisogrid composite design is lower than the central core mass obtained in the size optimization analysis in **??**

Composite design proposal				
Description - for the result	Analytical model numbers	Analytical model in FEM	Baseline 0th iteration in FEM (with vertical ribs)	Solution after optimization in FEM (with vertical ribs)
Structural mass (in kg) - excluding conm2	16.59	15.56	16.20	63.55
First frequency mode (in Hz)	NA	7.3	7.4	15.0
First buckling mode value (in N)	2.09E+06	1.41E+06	1.12E+06	1.39E+07

Table 8.1: Summary table of composite design proposal and FEM validation

Chapter 9

Conclusion

The concluding remarks for individual analysis methods have been discussed at the end of the specific chapter. An overall conclusion and scope for future research are presented in this section.

9.1 Thesis conclusion and insights

A methodology for the development of a main structure for the kick stage has been developed using the principles of structural optimization, and lightweight structure design with a special focus on the dynamics of propellant tank structures. The step-wise assessment of topology optimization followed by the development of the shape corresponding to the output and finally following it up with a size optimization matches the steps of the structural optimization. Thus, the research also demonstrates that a combination of optimization methods can provide results that are well-suited for complex loading requirements such as a combination of static, dynamic, and buckling load cases.

The design insights gained in topology optimization and the organic structures that we arrive at as a result, provide a better insight into the understanding of load path, load transfers, and the dynamic aspect of structural design. These insights could not be achieved simply by using conventional design methods or continuing the established spacecraft bus concepts. In addition, the density method for topology optimization can provide additional feedback on the material reassignment in not-so-commonly thought areas, particularly for large structures or cases in which the loading ratios along the three axes are different. The topology results are not enough for detailed design, as they are more continuous structures, however, the results show the impact of the presence of material in the design space availability impacts the structural performance.

The shape selection and size optimization remodeling step provides a more detailed and realistic design result. This also includes the considerations due to the design trinity aspects such as splitting the component into individual components which ease the manufacturability and assembly. The joining features are also carefully noted so as to match the layout obtained

in the earlier topology optimization result. The detailed design constraints of acceleration limit on the propellant tank affect the size optimization process more in comparison to the concept design optimization. This can be seen in the sensitivity to the normal modes analysis and the modal frequency response analysis. The frequency for which the propellant tank has a higher than qualified peak acceleration can be successfully modified by changing the stiffness and the mass distribution of the material. This can be seen in the results of the size optimization analysis, where for the same start design, the higher excitation load leads to a higher mass design. The design impact of this on the structural analysis is that the modal analysis and frequency response analysis can be included within an optimization framework along with the static loading conditions.

The next step proposed is to provide a step input, which can be notched in different frequencies, based on the considerations of dynamic excitation input of the core stage and solid boosters and also accounting for different levels of flight. The notched values can correspond to the solution 3 type of analysis, where the input excitation is at a lower level, while the higher resonant frequencies can correspond to the full-scale solution 2 type analysis. Additionally, after the Ariane6's first flight, actual measurements on the top of the upper stage will be obtained. These values could provide more realistic design values for future flight models of the kick stage. This would further help to bring out a better design. However, the methodology of dynamic consideration would still remain the same as proposed in this thesis. The impact of the selection of propellant tanks can also be varied in the model, as shown in the development of the topology model. The size of the tanks or the volume of propellant in the tanks could be varied, and this could lead to a revised design, which could be valid for other missions. A similar argument is possible for the spacecraft payload, where the satellite mass and center of gravity can be varied and this methodology could still work. This shows the modularity or interchangeability of the design for different propellant tanks or satellite payloads.

The composite design proposal using anisogrid design is a very promising design for the kick stage main structure. The single-cylinder design proposal and the preliminary FEM verification results are promising. The self-stabilization aspect of the anisogrid design is of particular relevance here, as this improves the buckling performance of the design by converting the compressive load on the cylinder to a tensile load on the circumferential ribs, thereby eliminating the need for knockdown factors. In addition, a higher redundancy can be expected because of the interlocking of circumferential and helical ribs. The design methodology here also can be modified and scaled quickly as per the input loads on the cylinder. The mass prediction for the composite design indicates that it provides a more lightweight design for the structure under consideration.

Thus, the thesis research objective of developing a design methodology for the kick stage main structure using structural optimization tools has been met. The insights of the literature study were used for developing and meeting two research goals. Firstly the methodology using structural optimization was developed, which took the static and dynamic loading conditions into account. The differences observed due to the oxidizer and propellant were factored into the design development, and this led to an innovative result output for the topology optimization study. These results were combined with the shape selection and size optimization tools to provide a reliable two-step methodology which also accounted for the dynamic responses and trinity principles of design, materials, manufacturing, and assembly. The second research goal of developing an innovative composite design for the kick stage

loading conditions on the central core led to the anisogrid design being selected. The results were prepared firstly using analytical methods and were followed by a FEM validation of the results, as the analytical model was inadequate for the dynamic behavior calculations. The manufacturing elements are addressed briefly, although not in detail, as the scope of the thesis was primarily focused on the design aspect.

9.2 Future work and recommendations

Additional detailing of the kick stage including the engine thrust load case and engine frame design can be added to the topology optimization framework. The current dynamics include only modal analysis and modal frequency response analysis up to 100Hz. Additional models can include high-frequency vibroacoustic analysis using tools such as Wave6 or Actran. While the focus of the thesis and research area was primarily on structural dynamics, a completely new coarser mesh needs to be prepared for the thermal analysis to decide the thermal requirements for the project.

For the model design itself, a more detailed model could be prepared including more segments such as avionics, thermal elements, harness, and fuel lines routing. Such a detailed model then can be tested for detailed interface forces. The final step would then be synchronizing these analyses within the prototype building and testing phase, perhaps with the qualification model of the kick stage. During these tests, the analysis results could be validated and correlated to match the test article responses.

The composite design anisogrid structure was proposed in this study and analysis was done at the preliminary level for the central core design. The additional detailed analysis that is required, could be carried out for the entire kick stage along with the propellant tanks. Additionally, a better modeling parameter for FEM verification could be developed instead of the CBAR element used in the scope of this thesis. The methodology for the optimization could be based on the results of structural optimization and the preliminary model discussed in this thesis. The total exercise would lead to significant challenges for the development of governing equations and the total design domain. It could however lead to a new master's thesis or a full-time work package of its own.

Appendix A

FEM formulation of Optimization

A.1 Optimization process overview

The explanation of topology optimization was done in this detail during the Literature study phase and submitted within the scope of the literature study [21] and is attached here as an appendix for reference. The Nastran implementation of a optimization iteration can be seen in flowchart Figure A.1. Derived from it, a detailed description of the processes within the optimization loop is described here.

Initial design problem

"The initial design is the FEM model that needs to be optimized. These variables are directly changed by the optimizer so as to satisfy the optimization problem statement. For the case of a topological optimization model, the entire design space can be meshed to provide input to the solver as the initial model. The design space can also be input as a small subset of meshes that need to be optimized. For topology optimization analysis, the card type is TOPVAR for MSC Nastran and DTPL for OptiStruct optimization [26] [1]."[21]

Structural analysis – load steps

"The structural analysis covers the FEM design problems for which the optimization has to be evaluated against. These will include the sub cases of structural analysis requirements for the project. These can include nearly all possible FEM structural analysis methods, as seen for the MSC Nastran solver SOL 200 in Table A.1. A near identical types of analyses are also supported in the OptiStruct optimization solver [1]. Each of these structural analysis by itself is identical to the corresponding standalone FEM problem. This implies that the boundary constraints such as fixed nodes, or load conditions such as gravity, forces, etc. and output requests such as displacements, stresses, etc. should be mentioned for each of these analysis within the optimization main problem. For this optimization project, the solutions for

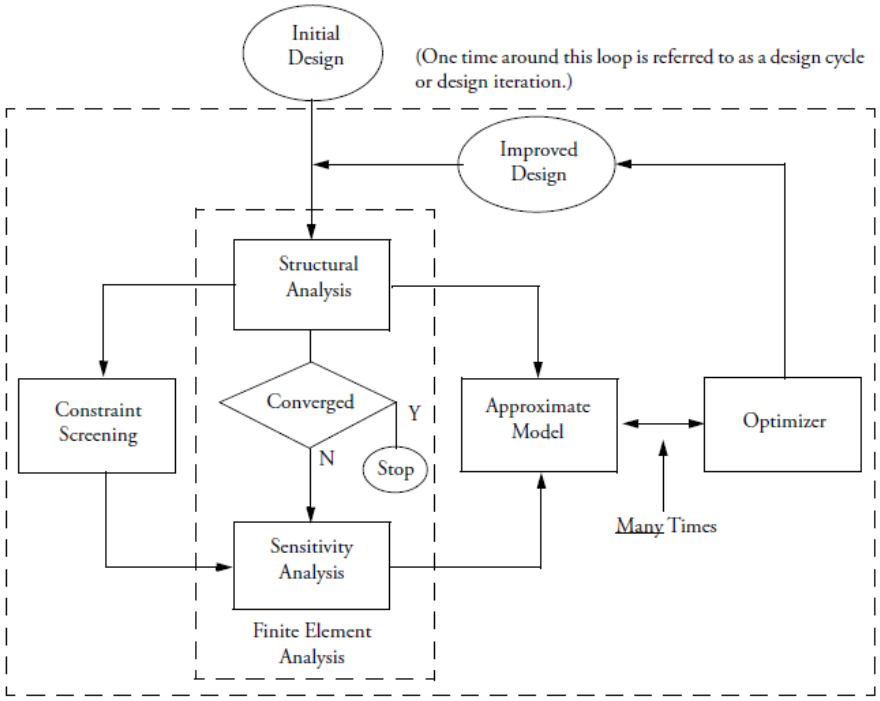

Figure A.1: MSC Nastran optimization process overview [26]

statics, normal modes, and buckling will form the analysis requirements for the optimization iterations. The design responses are evaluated for these structural solutions and recorded in the solver output files. These responses could be in different forms such as mass, compliance, displacement, frequency, stress, etc. The user requests these responses and the structural solutions for which the responses are requested. The bulk data entry cards for this is DRESP type and is discussed later in detail."[21]

Optimization constraints

"The constraints for the optimization problem are defined next. These constraints are different from the boundary conditions for specific structural analysis load step. The DRESP responses which are important to define the optimization design space are then written to a DCONSTR card with the allowed values as constraints. Alternatively, the DCONSTR entries can be collected into a single set using the DCONADD entry. For example, this can include constraints of a lower bound on the frequency requirements for the modal frequency analysis load step, or a upper bound on the stress observed on the critical elements for a static analysis load step, or upper and lower bound on the mass fraction of the entire structure. There could also be multiple constraints assigned from different structural analysis types or a weighted combination of results of each case."[21]

Analysis	SOL Numbers	Multiple Subcases	Multiple Boundary Conditions
Statics	101	Y	Y
Normal Modes	103	Y	Y
Buckling	105	Y	Y
Direct Complex Eigenanalysis	107	N	N
Direct Frequency	108	Y	Y
Modal Complex Eigenanalysis	110	N	N
Modal Frequency	111	Y	Y
Modal Transient	112	N	N
Static Aeroelasticity	144	Y	Y
Flutter	145	Y	Y

Table A.1: Analysis disciplines Supported in optimization solution SOL 200 for MSC Nastran [26]

Constraint Screening

"The constraint screening is then utilised for the selection of those 'killer requirements' that are of primary concern for redesign. This is because not all responses at all nodes/elements would play a role in the redesign. The process works in two steps in MSC Nastran, where the initial screening is done by a threshold, and the second screening is done based on the region of the mesh. The threshold as the name indicates, simply insists the constraint can be ignored if it does not exceed a specific value. The threshold is governed by the TRS parameter. The second step narrows down the largest few constraints which exceed the truncation value by a large margin in each region of the mesh. The regional selection of constraints is governed by the NSTR parameter. The final number can drastically reduce the total number of constraint checks to be performed by the optimizer on the mesh. Due to a concern where the default screening may ignore some critical constraints, the parameters TRS and NSTR can be modified by the user. Moreover, if any of the structural analysis load steps is found unimportant to produce critical design responses, then the entire load case can be ignored in the sensitivity studies. This will also help to reduce the iterations required by the optimizer [26]. Similar constraint screening, selection of suitable gradient search methods, move limit features are also a default characteristic of OptiStruct solver which smooths out the optimization process [1]."[21]

Design objective

"The design objective is a scalar quantity that is minimized or maximized which is the goal of the optimization problem. The optimizer works on approximate models to achieve this design objective. The case control command DESOBJ is used to define the objective. One of the single scalar responses defined by DRESP entry is passed on to DESOBJ to be the design objective [26] ."[21]

Design Sensitivity

"The sensitivity analysis is the computation of rate of change of a structural response with respect to the change of design variables. This function is automatically carried out within

the SOL 200 / OptiStruct framework. The sensitivities are calculated for all the responses that define the constraints retained after screening and the objective function. This develops the right approximate model where the highest impact of sensitivity is seen. Mathematically it is the partial differentiation of the response quantity with respect to the design variable for a particular set of design variables. Based on the structural analysis done in the load step section, the design sensitivities could be different for each case [26]."[21]

Optimizer

"There are two types of design optimization optimizers provided by MSC Nastran, which are MSCADS and IPOPT. MSC Nastran makes a logical decision based on an estimate as to which optimizer will provide better performance [26]. Based on studies that are required for structural analysis and scope of computations, the IPOPT is more often selected as it is suitable for topology optimization studies [12]. The optimization solution of the approximate model in OptiStruct also uses two classes of methods: dual method optimizer and primal method. The choice of optimizer is made automatically by OptiStruct based on the features of the input optimization problem. However, for large scale problems of optimization, the dual method optimizer is selected [1]. The detailed understanding of the optimization algorithm is not very important from the results perspective since both these algorithms use a approximation method for the design evaluation. Both the major optimizers are based on the algorithm of sequential unconstrained minimization technique (SUMT) [12]. The optimizer is a optimization algorithm that solves and develops the approximate model of the optimization problem. In MSC Nastran, the optimizer works within a 'do-while' loop which is linked to the INFO parameter. The optimization algorithm determines which retained constraints after constraint screening are active or violated. The constraints that are neither of these are ignored. This also reduces the number of computations required [26]. "[21]

Approximate model

"The approximate model is a intermediate model based on some of the approximation concepts which make the optimization feasible for large FEMs. Some aspects such as constraint screening and load case deletion are already mentioned before. The additional approximation concepts are based on the Taylor series expansion of the constraints and objectives. The features of linear design space, move limits, and changes of design variable limits or property limits is performed [26]. The detailing of these aspects is beyond the scope of this report, however, the takeaway is that the approximate model simplifies the computations and allows the optimizer loop to continue iterations based on the gradient calculations done for the objective and constraints for variable increments in the design space [26]."[21]

Convergence

"The convergence is a numerical criteria defined so that for the iterative optimization process, the process convergence indicates when the overall process has converged. The design cycle convergence in MSC Nastran is done using two methods. The *hard* convergence check occurs after structural analysis as seen in Figure A.1. The test results of the recent iteration FEM

is compared with those from the previous iteration in this convergence test. These results are conclusive to determine the if to terminate the design cycle or to let it continue. The results for these are also displayed in the output files and the user can check the convergence criteria progress over each iterations. The *soft* convergence check occurs at an intermediate stage between the improved design and the start of new iteration loop. This tests the results of the output of the approximate optimization to the input of the approximate optimization. This is useful for large computational models, where if the user sees that the optimizer has not changed variables significantly, the new iteration may be stopped by exiting the design loop and saving the data of the last iteration [26]. One such condition for convergence in OptiStruct is for two consecutive iterations, the objective function changes is less than the objective tolerance and the constraint violations are less than 1%. At least three analyses to follow this pattern are required for a regular convergence [1]." [21]

A.2 Optimization implementation within MSC Nastran

The flowchart instructions relevant to the input model are written to the solver input file using a series of D type bulk data entries. The sequence of development of these D type bulk data entries and the design modeling process is described in flowchart Figure A.2.

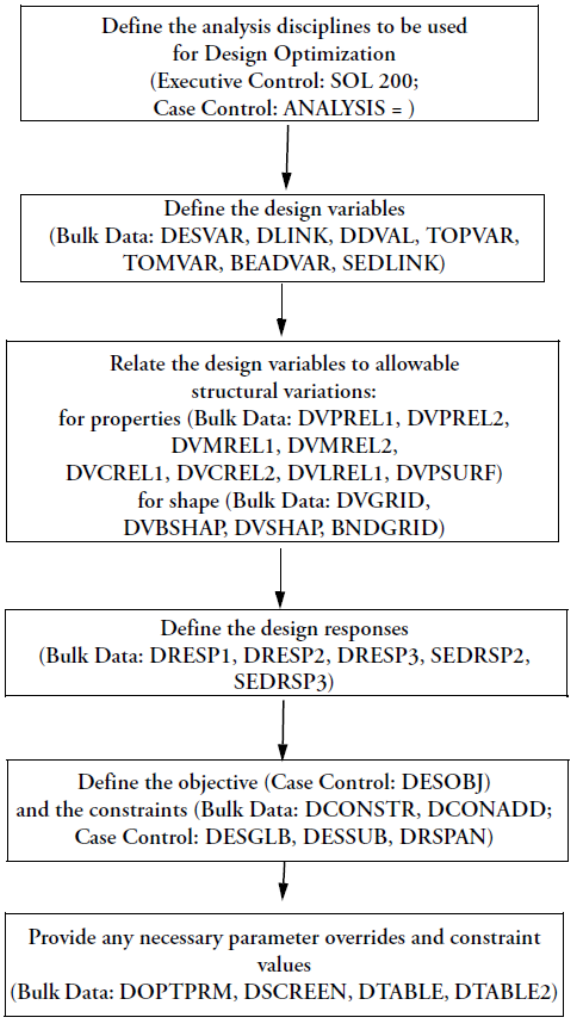

Figure A.2: MSC Nastran design optimization solution modelling process [26]

A.3 FEM data entry cards for optimization and structural analysis

The bulk data entry cards for structural optimization and structural analysis are alphabetically described briefly here. This includes some of the cards discussed in earlier section and mentioned in Figure A.2. This information is taken from the MSC Nastran Optimization user guide [26] and so is defined for MSC Nastran SOL 200 solution. Most of the important ones work for the OptiStruct studies too, although some entries are different and are noted as per the OptiStruct optimization user guide [1]. Most of the entry cards with D preffix are associated with optimization.

- CHEXA / CQUAD4 / CBAR / CONM2 – These define the individual elements in a finite element model. The detailed formatting of each element varies depending on the input nodes, properties of elements, whether 1D or 2D or 3D etc.
- DCONADD – This defines the design constraints as a union of individual DCONSTR

entry sets.

- DCONSTR – This places a limit of upper bound or lower bound or both on a design response entry within the constraints.
- DEQATN – This card is used to define equations for second level responses.
- DESOBJ – This card is the objective of the optimization problem. It is one of the singular scalar DRESP quantity which has to be either maximized or minimized. Typically minimizing mass or mass fraction or minimizing compliance (to maximize stiffness), are examples of the DESOBJ.
- DESVAR – This card defines the design variables in the design sensitivity and optimization analysis.
- DOPTPRM – This card is used for overriding the default values of the parameters in the design optimization analysis. This is important for the user since some analyses may require the user to change the default values of analysis parameters. Important properties that can be modified using DOPTPRM includes the optimizer selection, optimization method, change of convergence criteria, topology optimization variables modification, etc.
- DRESP1 – This important card it for defining each first level direct response created during the structural analysis segment of the optimization study. Also to be noted, the output from this can be passed on to DRESP2 and DRESP3 type responses. DRESP2 is equation responses consisting of one or multiple DRESP1 entries. DRESP3 is defined for external user input responses. Either of DRESP1 or DRESP2 or DRESP3 can be input for a constraint or objective of the optimization.
- DSCREEN – This card can override the information for screening of constraints.
- DVCREL1 / DVLREL1 / DVMREL1 / DVPREL1 – The DV cards are used for defining a relation between the analysis or mesh property to the design variables, particularly useful for size optimization. The DVCREL1 defines relation between a connectivity property and design variables. The DVLREL1 defines relation between analysis model loading and design variables. The DVMREL1 defines relation between material property and design variable. The DVPREL1 defines relation between analysis property and design variables. Similar to the DRESP2, there are also type 2 responses such as DVCREL2 / DVMREL2 / DVPREL2 available, where the relation is defined using a DEQATN entry.
- FREQi – These cards are used for defining the frequencies for which the modal frequency response calculations are done. The spacing of frequencies around the mode is usually denser as compared to regions where no modes are present.
- GRID – Each GRID entry defines a node in the numerical design space of finite element model.
- GRAV – This is used for defining the gravitational loads on the structure. Similarly, FORCE card can also be used.

- MATi – This card is used for defining material properties.
- PARAM – These are a set of cards with multiple suffix entries possible. For example, using a PARAM,POST allows to specify output type, PARAM,G allows for structural damping specifications.
- PSOLID / PSHELL / PBAR – These are the property cards associated with each element type. The material and the thickness parameters are stored for each card which is referred by each element type.
- RBE2 / RBE3 – These cards are used as rigid links between nodes so that they act for transferring assigned degrees of freedom from one node to another directly. They are highly stiff elements.
- RLOADi / DLOAD / TABLEDi – These together are used for providing a base input excitation for the modal frequency response analysis.
- SPC / SPCD – This card defines the constraints at a given node including fixed constraints for SPC and enforced constraint for SPCD.
- TOPVAR – This card defines the topology design region in a topology optimization problem. The card contains the corresponding PTYPE property cards that will be modified during the topology optimization and where the density between zero to 1.0 is assigned to elements. This is only present in MSC Nastran. The card for OptiStruct is DTPL, which allows for the creation of design variables for a topological optimization problem. Additional properties to this card includes MINDIM, MAXDIM which govern the dimensions, or the manufacturing method properties such as draw or extrusion methods, or pattern grouping for symmetry or repetition of the part. This allows the user to define multiple properties for the development of the optimized design space before the solver starts.

In addition, the entries for volume, fractional mass, compliance, eigen values, are also useful in the optimization problem definition. This is in addition to the normal output cards such as displacement, forces, stresses, etc which are useful for the DRESP card definition and plotting results across iterations.

Appendix B

Sine Input excitation

B.1 Sine Input specification for the Ariane 6

The sine input specification at the top of the upper stage is given in Table B.1 and is mentioned in the Ariane 6 User manual [6].

Direction	Frequency band (Hz)	Sine amplitude (g)
Longitudinal	2 – 50	1.0
	50 - 100	0.8
Lateral	2 – 25	0.8
	25 – 100	0.6

Table B.1: Sine excitation at spacecraft base for the Ariane 6 launch vehicle [6]

Appendix C

Anisogrid governing equations

C.1 Composite design anisogrid governing equations

The anisogrid governing equations are described in greater detail in extensive work by Vasiliev et al. [34]. The details can be found in [34], [33], [7], [35], [17].

$$\begin{aligned} N_x &= B_{11}\varepsilon_x + B_{12}\varepsilon_y, \quad M_x = D_{11}k_x + D_{12}k_y \\ N_y &= B_{21}\varepsilon_x + B_{22}\varepsilon_y, \quad M_y = D_{21}k_x + D_{22}k_y \\ N_{xy} &= B_{33}\varepsilon_{xy} \quad M_{xy} = D_{33}k_{xy} \end{aligned} \tag{C.1}$$

$$D_{mn} = \frac{h^2}{12}B_{mn}$$

where

$$\begin{aligned} B_{11} &= B_\varphi \cos^4\varphi + B_x, B_{22} = B_\varphi \sin^4\varphi + B_y, B_{12} = B_{21} = B_{33} \\ &= B_\varphi \sin^2\varphi \cos^2\varphi \end{aligned}$$

and

$$\begin{aligned} &B_\varphi = 2E_\varphi h\bar{\delta}_\varphi, B_x = E_x h\bar{\delta}_x, B_y = E_y h\bar{\delta}_y \\ &\bar{\delta}_\varphi = \tfrac{\delta_\varphi}{a_\varphi}, \bar{\delta}_x = \tfrac{\delta_x}{a_x}, \bar{\delta}_y = \tfrac{\delta_y}{a_y} \end{aligned}$$

Appendix D

Anisogrid sizing

D.1 Composite design anisogrid sizing calculation iterations

The anisogrid analytical model sizing is shown here. The table shows the different number of ribs and how the geometric spacing and the width varies with respect to it.

Diameter	1.666
phi	26.565
cos phi	0.89442759
tan phi	0.499998883
d bar phi	0.07648
d bar y	0.03824

		Geometric spacing of ribs (in m)			Width of the ribs (in m)	
Number of ribs	angle subtended at axial center	a	a_h	a_c	d_h	d_c
10	36	5.234E-01	4.681E-01	5.234E-01	3.580E-02	2.001E-02
20	18	2.617E-01	2.341E-01	2.617E-01	1.790E-02	1.001E-02
30	12	1.745E-01	1.560E-01	1.745E-01	1.193E-02	6.671E-03
40	9	1.308E-01	1.170E-01	1.308E-01	8.951E-03	5.004E-03
45	8	1.163E-01	1.040E-01	1.163E-01	7.956E-03	4.448E-03
50	7.2	1.047E-01	9.363E-02	1.047E-01	7.161E-03	4.003E-03
60	6	8.723E-02	7.802E-02	8.723E-02	5.967E-03	3.336E-03
70	5.142857143	7.477E-02	6.688E-02	7.477E-02	5.115E-03	2.859E-03
80	4.5	6.542E-02	5.852E-02	6.542E-02	4.475E-03	2.502E-03
90	4	5.815E-02	5.201E-02	5.815E-02	3.978E-03	2.224E-03
100	3.6	5.234E-02	4.681E-02	5.234E-02	3.580E-03	2.001E-03
110	3.272727273	4.758E-02	4.256E-02	4.758E-02	3.255E-03	1.819E-03
120	3	4.362E-02	3.901E-02	4.362E-02	2.984E-03	1.668E-03
130	2.769230769	4.026E-02	3.601E-02	4.026E-02	2.754E-03	1.540E-03
140	2.571428571	3.738E-02	3.344E-02	3.739E-02	2.557E-03	1.430E-03
150	2.4	3.489E-02	3.121E-02	3.489E-02	2.387E-03	1.334E-03
160	2.25	3.271E-02	2.926E-02	3.271E-02	2.238E-03	1.251E-03
170	2.117647059	3.079E-02	2.754E-02	3.079E-02	2.106E-03	1.177E-03
180	2	2.908E-02	2.601E-02	2.908E-02	1.989E-03	1.112E-03
190	1.894736842	2.755E-02	2.464E-02	2.755E-02	1.884E-03	1.053E-03
200	1.8	2.617E-02	2.341E-02	2.617E-02	1.790E-03	1.001E-03

Table D.1: Geometric spacing and width of ribs as varying with the number of ribs [6]

The graphs below show the plot of this variation of the geometric spacing Figure D.1 and the width of the ribs Figure D.2 with respect to the number of ribs.

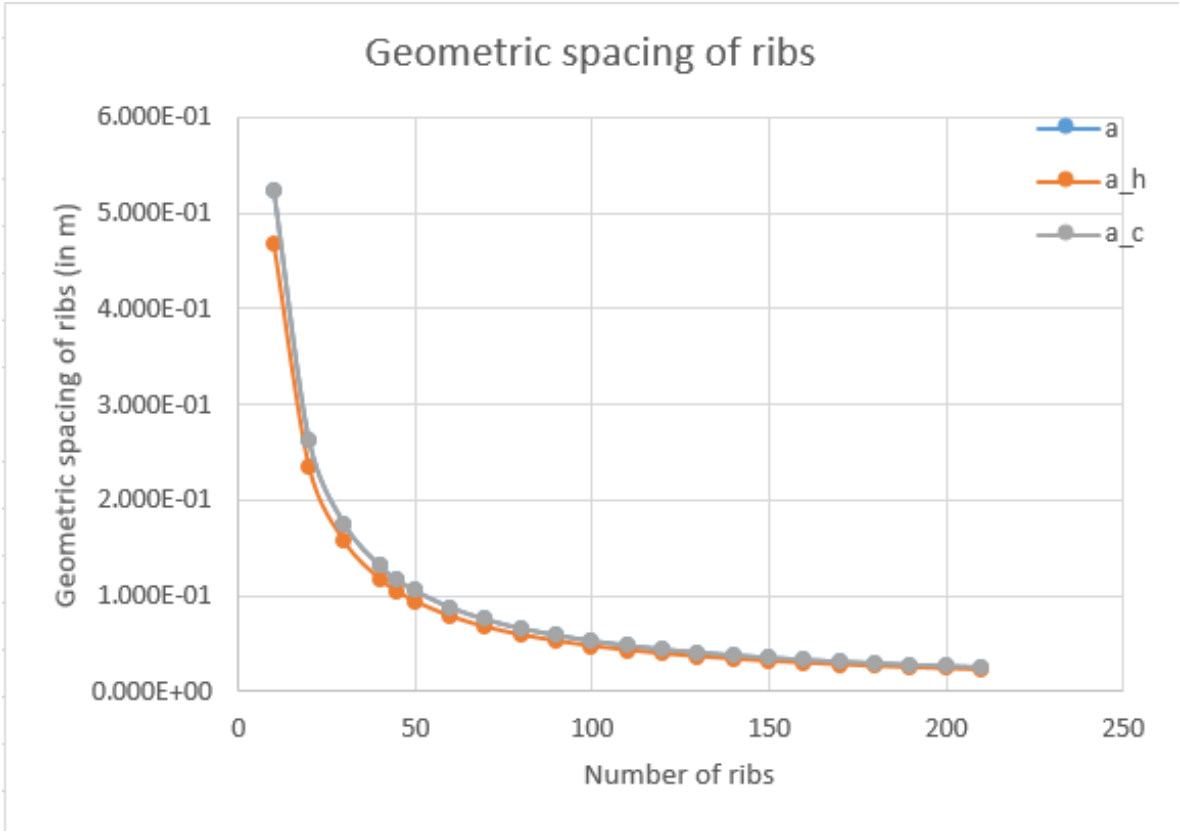

Figure D.1: Analytical composite design – geometric spacing

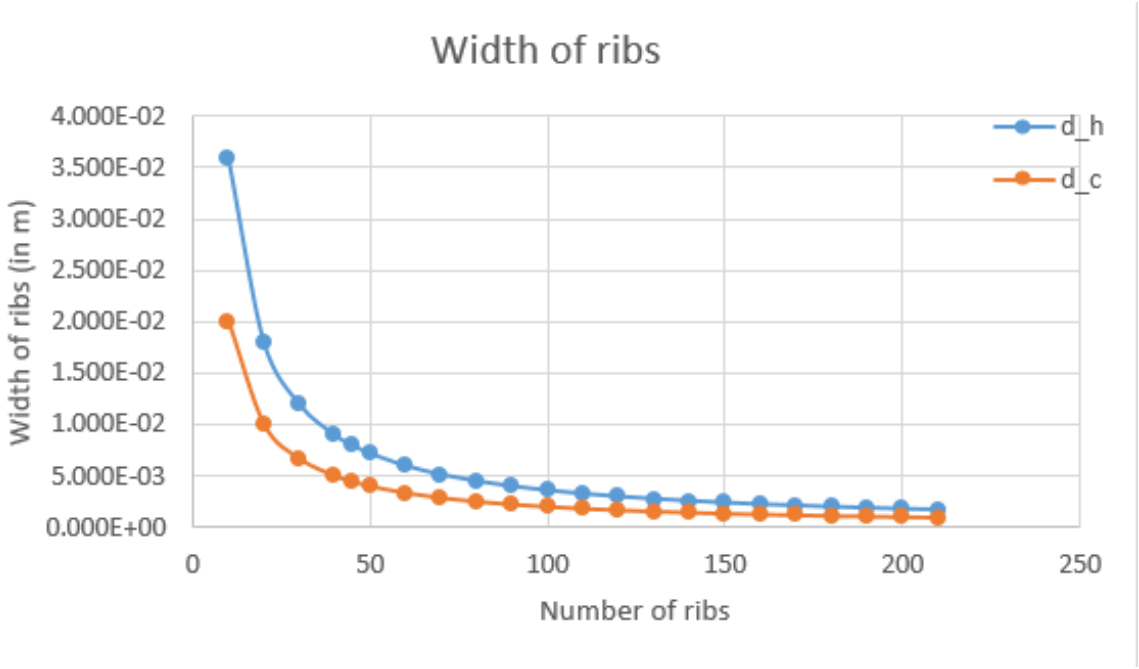

Figure D.2: Analytical composite design – width sizing

References

[1] Altair Engineering Inc. Practical Aspects of Structural Optimization with Altair OptiStruct. Technical report, 2021.

[2] ArianeGroup. ArianeGroup to develop PHOEBUS for ESA as demonstrator for Ariane 6 future carbon upper stage, 11 2022. URL https://press.ariane.group/arianegroup-developpe-phoebus-pour-lesa-un-demonstrateur-du-futur-etage-superieur-dariane-6-en-materiaux-composites-6071/.

[3] ArianeGroup GmbH. Ariane 6, rocketing to the moon with a new ultralight upper stage, 2019. URL https://www.ariane.group/en/news/new-video-ariane-6-rocketing-to-the-moon-with-a-new-ultralight-upper-stage/.

[4] ArianeGroup GmbH. The ArianeGroup kick stage: taking Ariane 6's versatility to new heights, 2020. URL https://www.ariane.group/en/news/the-arianegroup-kick-stage-taking-ariane-6s-versatility-to-new-heights/.

[5] ArianeGroup GmbH. Astris system development and qualification project. 2020.

[6] ArianeSpace. Ariane 6 user's manual. Technical report, 2021.

[7] V. G. Belardi, P. Fanelli, and F. Vivio. Structural analysis and optimization of anisogrid composite lattice cylindrical shells. *Composites Part B: Engineering*, 139:203–215, 4 2018. ISSN 13598368. doi: 10.1016/j.compositesb.2017.11.058.

[8] M P Bendsøe. Optimal shape design as a material distribution problem. *Structural optimization*, 1(4):193–202, 1989. ISSN 1615-1488. doi: 10.1007/BF01650949. URL https://doi.org/10.1007/BF01650949.

[9] Philippe Berthe, Ann P Over, Michelle Picardo, and Anthony W Byers. Orion European Service Module (ESM) development, integration and qualification status. In *2018 AIAA SPACE and Astronautics Forum and Exposition*, Orlando, 9 2017. doi: 10.2514/6.2017-5144.

[10] Chiara Bisagni. Stability and Analysis of Structures I Buckling of Cylindrical Shells and Buckling of a Wing Box. Technical report, Delft University of Technology, 2021.

[11] Boyang Chen. Non-Linear Modeling Lecture 3 AS4ASM505 2018. Technical report, Delft University of Techonology, 2018.

[12] Wook-Han Choi, Cheng-Guo Huang, Jong-Moon Kim, and Gyung-Jin Park. Comparison of some commercial software systems for structural optimization. In *11th World Congress on Structural and Multidisciplinary Optimisation*, Sydney, 6 2015. URL https://www.aeromech.usyd.edu.au/WCSMO2015/papers/1037_paper.pdf.

[13] Gandolfo Di Vita, Sofia Caeiro, Tiziana Cardone, Gonçalo Rodrigues, Andrea Amaldi, Antoine Alouani, Guillaume Dussardier, Cyprien Le-Plenier, Stefano Scalisi, Paolo Palmieri, Moreno Faraud, Louis J Ghosn, and Ryan W Proud. Design optimisation and mass saving of the structure of the Orion-MPCV European Service Module. In *69th International Astronautical Congress (IAC)*, Bremen, 10 2018.

[14] ESA. Contracts signed for prototype of a highly-optimised black upper stage, 2019. URL https://www.esa.int/Enabling_Support/Space_Transportation/Future_space_transportation/Contracts_signed_for_prototype_of_a_highly-optimised_black_upper_stage.

[15] ESA. Ariane 6 targets new missions with Astris kick stage, 2021. URL https://www.esa.int/Enabling_Support/Space_Transportation/Ariane/Ariane_6_targets_new_missions_with_Astris_kick_stage.

[16] Jie Gao, Mi Xiao, Yan Zhang, and Liang Gao. A Comprehensive Review of Isogeometric Topology Optimization: Methods, Applications and Prospects. *Chinese Journal of Mechanical Engineering (English Edition)*, 33(1), 12 2020. ISSN 21928258. doi: 10.1186/s10033-020-00503-w. URL https://cjme.springeropen.com/articles/10.1186/s10033-020-00503-w#.

[17] Steven M Huybrechts, Steven E Hahn, and Troy E Meink. Grid stiffened structures: A survey of fabrication, analysis and design methods. In *International Conference on Composite Materials*, Paris, 7 1999. URL https://www.iccm-central.org/Proceedings/ICCM12proceedings/site/papers/pap357.pdf.

[18] ISRO. Disassembled view of I3K satellite bus, 2016. URL https://www.isro.gov.in/sites/default/files/tenders/eoi_4.pdf/.

[19] Christos Kassapoglou, Peter Belobaba, Jonathan Cooper, Roy Langton, and Allan Seabridge. *Design and Analysis of Composite Structures Second Edition Aerospace Series With Applications to Aerospace Structures*. 2013.

[20] Abdul Khaleelullah, Sk J Basha, and H K Rangavittal. Design and Analysis of Propellant Tanks Support Structure for an Advanced Spacecraft. *International Journal of Applied Research In Mechanical Engineering (IJARME)*, 1(3):194–200, 1 2012. doi: 10.47893/IJARME.2012.1035.

[21] Akshay Kulkarni. Kick Stage Main Structure Design Methodology (Literature Study). Technical report, Delft University of Technology, 2022.

[22] Akshay Kulkarni. Design Methodology Development and Optimization of Kick Stage Main Structures (Project Plan). Technical report, Delft University of Technology, 2022.

[23] Prashant Kumar Srivastava and Sanjay Shukla. Structural Optimization Methods: A General Review. Technical Report 9, 2007. URL www.ijirset.com.

[24] McDonnell Douglas Astronautics Company. Isogrid design handbook. Technical report, 1973. URL https://femci.gsfc.nasa.gov/isogrid/NASA-CR-124075_Isogrid_Design.pdf.

[25] MSC. MSC Nastran 2018 Linear Static Analysis User's Guide. Technical report, 2018. URL http://msc-documentation.questionpro.com.

[26] MSC. MSC Nastran 2020 Design Sensitivity and Optimization User's Guide. Technical report, MSC Software Corporation, 2020. URL http://msc-documentation.questionpro.com.

[27] MSC. MSC Nastran 2021 Dynamic Analysis User's Guide. Technical report, MSC Software Corporation, 2021. URL http://msc-documentation.questionpro.com.

[28] NASA. Rocket staging . URL https://www.grc.nasa.gov/www/k-12/rocket/rktstage.html#:~:text=The%20first%20stage%20is%20ignited,the%20second%20stage%20into%20orbit.

[29] NASA. *Buckling of Thin-Walled Circular Cylinders*. 2 edition, 2020. URL http://www.sti.nasa.gov.

[30] Leonid Pavlov, Ivar Te Kloeze, Bart J R Smeets, and Sahak Menzo (Samo) Simonian. Development of mass and cost efficient grid-stiffened and lattice structures for space applications. Toulouse, 9 2016.

[31] Thomas Roberts. Space Launch to Low Earth Orbit: How Much Does It Cost?, 6 2022.

[32] Catherine Spivey. Design Optimization of an Isogrid or Orthogrid Tank for Small, Low-Cost Launch Vehicles. Technical report, 2021. URL https://www.researchgate.net/publication/355410230.

[33] V. V. Vasiliev and A. F. Razin. Anisogrid composite lattice structures for spacecraft and aircraft applications. *Composite Structures*, 76(1-2):182–189, 10 2006. ISSN 02638223. doi: 10.1016/j.compstruct.2006.06.025.

[34] V. V. Vasiliev, V. A. Barynin, and A. F. Razin. Anisogrid composite lattice structures - Development and aerospace applications. *Composite Structures*, 94(3):1117–1127, 2 2012. ISSN 02638223. doi: 10.1016/j.compstruct.2011.10.023.

[35] Theodore Von Karman and Hsue-Shen Tsein. The Buckling of Thin Cylindrical Shells under Axial Compression. *Journal of Aeronautical Sciences*, 8(8):898–907, 6 1941. ISSN 0022-4650. doi: 10.2514/2.7056.